Into the unknown: Exploring the surface chemistry of black phosphorus

Kendahl L. Walz Mitra

A dissertation

submitted in partial fulfillment of the

requirements for the degree of

Doctor of Philosophy

University of Washington

2023

Reading Committee:

Alexandra Velian, Chair

Brandi M. Cossairt

Dianne J. Xiao

Program Authorized to Offer Degree:

Chemistry

University of Washington

Abstract

Into the unknown: Exploring the surface chemistry of black phosphorus

Kendahl L. Walz Mitra

Chair of the Supervisory Committee:
Alexandra Velian
Department of Chemistry

Black phosphorus (bP), a layered 2D allotrope of elemental phosphorus, is a promising material for electronic and catalytic applications, among others, due to its direct, tunable bandgap, high carrier mobility, and relatively reactive basal plane. Although reactivity, likely originating from the surface lone pairs, occurs adventitiously, our understanding of bP chemistry remains limited. Facile methods to functionalize the surface and probe the resulting modified nanosheets are scarce: previous reports of bP functionalization suffer from oxidative degradation of exfoliated nanosheets, low signal-to-noise ratios, and minimal changes in characteristic bP features post-functionalization. When functionalization is reported, further investigation into the stoichiometric chemistry of the modified nanosheets is rare, limiting rational application of bP materials. This work dives into the intersection of molecular phosphine chemistry and materials design to investigate the fundamental chemistry of bP through covalent functionalization and to

apply these principles to fabricate a bP-supported hydroformylation catalyst. In Chapter 2, clear covalent bonds between nitrene functional groups and the bP surface are demonstrated via infrared spectroscopy and ^{15}N isotopic labeling. In Chapter 3, the ligand character of bP (Tolman electronic parameter, buried volume) in an organometallic complex is investigated using discrete metal carbonyl functional groups. Finally, strategies developed herein are applied in Chapter 4 to synthesize and study the reactivity of a novel bP-supported hydroformylation catalyst. The body of work presented herein establishes a detailed understanding of bP surface chemistry and demonstrates its applications as a novel and chemically interesting support.

TABLE OF CONTENTS

LIST OF FIGURES

LIST OF TABLES

ACKNOWLEDGEMENTS

A dissertation is rarely the result of one person working in a vacuum and that is not the case here. There are many people who have made invaluable contributions and without whom, this work would not exist. Firstly, I thank my advisor, Prof. Alexandra Velian who's dedication to sitting down and discussing each piece of data and experiment pushed this research forward. This experience has undoubtedly made me a better scientist and I hope the work reflects that.

Secondly, I thank the other Velian group members for all their support throughout this process. In particular, Michael Riehs and Andrei Draguicevic, the other members of the 2D team, who both contributed to this work and will carry it forward – I can't wait to see what you do in the future. Ben Mitchell and Jon Kephart who have been there since the beginning – all I can say is thank you for everything.

Thirdly, my committee – Prof. Brandi Cossairt, Prof. Dianne Xiao, Prof. Xiaodong Xu, and Prof. Daniel Gamelin – thank you for your support over the years and for your insightful questions and comments that always kept me thinking.

Finally, thank you to my family and friends. In particular, my parents, Kristin, Kevin, Marguerite, Randy, and my sisters, Marin and Keira – thank you for your unconditional support on the long journey to get here, patiently listening even when what I was saying didn't make sense, and for enduring the long flights out to Seattle. And to my husband, Kinshuk – this one's for you.

DEDICATION

This work is dedicated to my husband, Kinshuk. I couldn’t have done it without you.

1 INTRODUCTION

1.1 OVERVIEW OF BLACK PHOSPHORUS

Black phosphorus (bP), a 2D van der Waals nanosheet, represents an exciting frontier as a next-generation nanomaterial. Its unique electronic, structural, and chemical properties make it attractive for applications from field effect transistors[1] and photovoltaics[2] to chemical sensing[3] and catalysis.[4,5] bP is distinct from other common van der Waals materials with a unique corrugated, anisotropic structure derived from the sp^3-hybridization of the tricoordinate phosphorus atoms. This ridged surface gives bP a higher surface area-to-volume ratio than other 2D materials.[6] Like all van der Waals materials, the nanosheets are held together by weak van der Waals forces while the intralayer P–P bonds are covalent. As a result, bP can be exfoliated to monolayers and few-layer stacks.

The most thermodynamically stable allotrope of elemental phosphorus, bP was discovered in 1914 by Bridgman.[7] Its basic structure and properties were revealed soon after: Hultgren and coworkers reported the bP crystal structure in 1935[8] and its electronic properties were detailed by Keyes and coworkers in 1953.[9] However, interest in this new material remained limited until the discovery of graphene in 2004 ignited interest in van der Waals materials more generally. The “black phosphorus renaissance” then emerged in 2008 with a report by Nilges and coworkers for a low-pressure synthesis of high-quality bP crystals.[10]

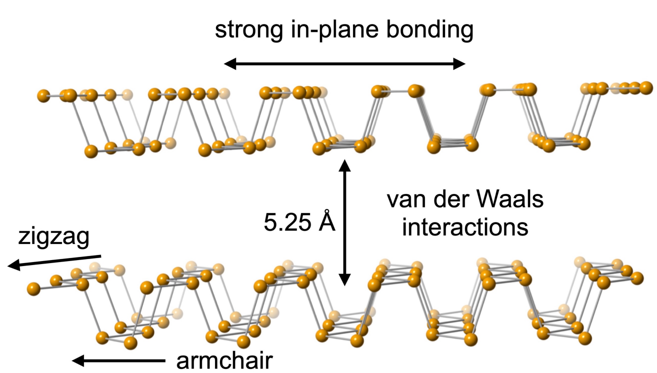

Figure 1.1. Structure of black phosphorus.

Much of the interest in bP centers around its compelling electronic properties. bP is a semiconductor with a direct tunable bandgap ranging from 0.3 eV in the bulk to 2.1 eV in the monolayer.[11,12] This energy range spans the mid-IR to visible region, bridging the gap between graphene (metallic) and transition metal dichalcogenides (TMDCs; bandgap primarily in the visible region).[13] Although most 2D semiconductors are n-type, bP is intrinsically p-type due to vacancies and self-interstitial atoms;[14] however, n-type character can be induced by surface doping.[15] The tunable bandgap combined with high carrier (hole) mobility (*ca.* 1000 $cm^2V^{-1}s^{-1}$)[16] and high on/off ratio (10^5)[17] makes bP an ideal material for electronic and optical applications. In contrast, MoS_2 has a hole mobility of less than 270 $cm^2V^{-1}s^{-1}$.[18]

The unique in-plane anisotropy also impacts bP's transport properties and causes an enhanced thermoelectric effect:[19] hole mobility is *ca.* 2x larger along the armchair direction compared to the zigzag direction.[16] In contrast, thermal conductivity is greater along the zigzag direction (20–40 $Wm^{-1}K^{-1}$) compared to the armchair direction (10–20 $Wm^{-1}K^{-1}$).[20]

1.2 Surface Functionalization of bP

Since the first report of bP covalent functionalization by Ryder and coworkers in 2016,[21] the chemical properties of the bP surface have also been a topic of interest. Surface chemistry on bP happens adventitiously: when exposed to ambient conditions, bP will oxidize rapidly.[22] The likely loci of this reactivity is the lone pairs on the surface which produce a relatively reactive basal plane in contrast to other van der Waals materials like graphene, MoS_2, and h-BN.[23]

Covalent functionalization in particular offers a facile method to further tune bP's unique electronic and chemical properties by forming bonds between the surface and a new chemical species. Since 2016, bP functionalization has been reported with a variety of organic groups including aryl,[24–27] alkyl,[28–31] and amine groups,[32,33] and C_{60}[34] as well as inorganic nanoparticles,[4,35–40] quantum dots,[41] and metal atoms.[42–45] Much of these functionalization methods are adapted from other 2D materials with saturated surfaces (e.g. graphene, TMDCs) and do not leverage the unique reactivity of the bP basal plane or systematically explore its chemistry. Additionally, as with all surfaces, characterizing the exact nature of the functional group–surface interaction is also challenging. For bP, this characterization is further complicated by adventitious oxidation that may occur during exfoliation and functionalization. As a result, many basic questions concerning bP surface chemistry remain unanswered including how to predict competent functionalization partners, the electronic and steric nature of bP as a ligand, particularly compared to its well-understood molecular analogs, phosphines, and how to consistently probe what happens once the surface has been modified. While some of these questions have been considered by theory,[23] experimental evidence remains scarce. Ultimately, this lack of understanding hinders applications of functionalized bP.

The following work begins to address some of these gaps in our understanding of bP chemistry. Chapter 2 shows how bP's intrinsic reactivity can be leveraged to functionalize the surface with nitrene groups using mild conditions. Molecular (IR, Raman, and NMR spectroscopies) and materials characterization techniques (XPS, AFM, SEM) are developed to probe the modified surface with precision. Chapter 3 investigates the nature of bP as a ligand through functionalization with Lewis acidic organometallic fragments. IR characterization suggests that bP acts as a relatively strong σ-donor with a moderate steric profile. Subsequent reactions with the functionalized nanosheets show stoichiometric reactivity comparable to molecular phosphine analogs. Finally, in Chapter 4, a proposed single site Rh/bP heterogeneous catalyst is employed for hydroformylation for the first time. Preliminary results suggest that the metal remains bound to the bP surface during catalysis, and that electronic metal-support interactions play a key role in the observed activity.

1.3 References

[1] H. Liu, Y. Du, Y. Deng, P. D. Ye, *Chem. Soc. Rev.* **2015**, *44*, 2732–2743.

[2] M. Batmunkh, M. Bat-Erdene, J. G. Shapter, *Adv. Mater.* **2016**, *28*, 8586–8617.

[3] D. An, X. Zhang, Z. Bi, W. Shan, H. Zhang, S. Xia, M. Qiu, *Adv Funct Materials* **2021**, *31*, 2106484.

[4] M. Vanni, M. Caporali, M. Serrano-Ruiz, M. Peruzzini, *Surfaces* **2020**, *3*, 132–167.

[5] T. Yin, L. Long, X. Tang, M. Qiu, W. Liang, R. Cao, Q. Zhang, D. Wang, H. Zhang, *Advanced Science* **2020**, *7*, 2001431.

[6] S.-Y. Cho, Y. Lee, H.-J. Koh, H. Jung, J.-S. Kim, H.-W. Yoo, J. Kim, H.-T. Jung, *Adv. Mater.* **2016**, *28*, 7020–7028.

[7] P. W. Bridgman, *J. Am. Chem. Soc.* **1914**, *36*, 1344–1363.

[8] R. Hultgren, N. S. Gingrich, B. E. Warren, *The Journal of Chemical Physics* **1935**, *3*, 351–355.

[9] R. W. Keyes, *Phys. Rev.* **1953**, *92*, 580–584.

[10] T. Nilges, M. Kersting, T. Pfeifer, *Journal of Solid State Chemistry* **2008**, *181*, 1707–1711.

[11] A. H. Woomer, T. W. Farnsworth, J. Hu, R. A. Wells, C. L. Donley, S. C. Warren, *ACS Nano* **2015**, *9*, 8869–8884.

[12] A. Castellanos-Gomez, L. Vicarelli, E. Prada, J. O. Island, K. L. Narasimha-Acharya, S. I. Blanter, D. J. Groenendijk, M. Buscema, G. A. Steele, J. V. Alvarez, H. W. Zandbergen, J. J. Palacios, H. S. J. van der Zant, *2D Mater.* **2014**, *1*, 025001.

[13] A. Castellanos-Gomez, *J. Phys. Chem. Lett.* **2015**, *6*, 4280–4291.

[14] V. Wang, Y. Kawazoe, W. T. Geng, *Phys. Rev. B* **2015**, *91*, 045433.

[15] D. Yue, D. Lee, Y. D. Jang, M. S. Choi, H. J. Nam, D.-Y. Jung, W. J. Yoo, *Nanoscale* **2016**, *8*, 12773–12779.

[16] F. Xia, H. Wang, Y. Jia, *Nat Commun* **2014**, *5*, 4458.

[17] M. Huang, M. Wang, C. Chen, Z. Ma, X. Li, J. Han, Y. Wu, *Adv. Mater.* **2016**, *28*, 3481–3485.

[18] Z. Jin, X. Li, J. T. Mullen, K. W. Kim, *Phys. Rev. B* **2014**, *90*, 045422.

[19] A. Carvalho, M. Wang, X. Zhu, A. S. Rodin, H. Su, A. H. Castro Neto, *Nat Rev Mater* **2016**, *1*, 16061.

[20] Z. Luo, J. Maassen, Y. Deng, Y. Du, R. P. Garrelts, M. S. Lundstrom, P. D. Ye, X. Xu, *Nat Commun* **2015**, *6*, 8572.

[21] C. R. Ryder, J. D. Wood, S. A. Wells, Y. Yang, D. Jariwala, T. J. Marks, G. C. Schatz, M. C. Hersam, *Nature Chemistry* **2016**, *8*, 597–602.

[22] M. van Druenen, F. Davitt, T. Collins, C. Glynn, C. O'Dwyer, J. D. Holmes, G. Collins, *Langmuir* **2019**, *35*, 2172–2178.

[23] A. Ienco, G. Manca, M. Peruzzini, C. Mealli, C. Organometallici, C. Nazionale, *Dalton Transactions* **2018**, *47*, 17243–17256.

[24] M. van Druenen, F. Davitt, T. Collins, C. Glynn, C. O'Dwyer, J. D. Holmes, G. Collins, *Chem. Mater.* **2018**, *30*, 4667–4674.

[25] Y. Cao, X. Tian, J. Gu, B. Liu, B. Zhang, S. Song, F. Fan, Y. Chen, *Angew. Chem. Int. Ed.* **2018**, *57*, 4543–4548.

[26] W. Chen, S. Gao, Z. Xie, Y. Lu, G. Gong, G. Liu, J. Shang, C. Yao, R.-W. Li, *J. Mater. Chem. C* **2020**, *8*, 7309–7313.

[27] S. Thurakkal, X. Zhang, *Mater. Chem. Front.* **2021**, *5*, 2824–2831.

[28] Z. Sofer, J. Luxa, D. Bouša, D. Sedmidubský, P. Lazar, T. Hartman, H. Hardtdegen, M. Pumera, *Angew. Chem. Int. Ed.* **2017**, *56*, 9891–9896.

[29] H. Hu, H. Gao, L. Gao, F. Li, N. Xu, X. Long, Y. Hu, J. Jin, J. Ma, *Nanoscale* **2018**, *10*, 5834–5839.

[30] S. Wild, X. T. Dinh, H. Maid, F. Hauke, G. Abellán, A. Hirsch, *Angew. Chem. Int. Ed.* **2020**, *59*, 20230–20234.

[31] S. Wild, M. Fickert, A. Mitrovic, V. Lloret, C. Neiss, J. A. Vidal-Moya, M. Á. Rivero-Crespo, A. Leyva-Pérez, K. Werbach, H. Peterlik, M. Grabau, H. Wittkämper, C. Papp, H. Steinrück, T. Pichler, A. Görling, F. Hauke, G. Abellán, A. Hirsch, *Angew. Chem. Int. Ed.* **2019**, *58*, 5763–5768.

[32] Y. Liu, P. Gao, T. Zhang, X. Zhu, M. Zhang, M. Chen, P. Du, G. Wang, H. Ji, J. Yang, S. Yang, *Angew. Chem. Int. Ed.* **2019**, *58*, 1479–1483.

[33] K. L. Walz Mitra, C. H. Chang, M. P. Hanrahan, J. Yang, D. Tofan, W. M. Holden, N. Govind, G. T. Seidler, A. J. Rossini, A. Velian, *Angew. Chem. Int. Ed.* **2021**, *60*, 9127–9134.

[34] X. Zhu, T. Zhang, D. Jiang, H. Duan, Z. Sun, M. Zhang, H. Jin, R. Guan, Y. Liu, M. Chen, H. Ji, P. Du, W. Yan, S. Wei, Y. Lu, S. Yang, *Nat Commun* **2018**, *9*, 4177.

[35] D. Zhang, X. Lin, S. Lan, H. Sun, X. Wang, X. Liu, Y. Zhang, Y. Zeng, *Particle and Particle Systems Characterization* **2018**, *35*, 1–11.

[36] M. Caporali, M. Serrano-Ruiz, F. Telesio, S. Heun, G. Nicotra, C. Spinella, M. Peruzzini, *Chemical Communications* **2017**, *53*, 10946–10949.

[37] G. Lee, S. Jung, S. Jang, J. Kim, *Applied Physics Letters* **2017**, *110*, DOI 10.1063/1.4985708.

[38] W. Lei, T. Zhang, P. Liu, J. A. Rodriguez, G. Liu, M. Liu, *ACS Catalysis* **2016**, *6*, 8009–8020.

[39] S. Y. Cho, H. J. Koh, H. W. Yoo, H. T. Jung, *Chemistry of Materials* **2017**, *29*, 7197–7205.

[40] Y. Peng, B. Lu, N. Wang, J. E. Lu, C. Li, Y. Ping, S. Chen, *ACS Applied Materials & Interfaces* **2019**, *11*, 24707–24714.

[41] X. Jiang, H. Jin, R. Gui, *Dalton Trans.* **2020**, *49*, 11911–11920.

[42] X. Liu, L. Xiao, J. Weng, Q. Xu, W. Li, C. Zhao, J. Xu, Y. Zhao, *Sci. Adv.* **2020**, *6*, eabb4359.

[43] Y. Zhao, H. Wang, H. Huang, Q. Xiao, Y. Xu, Z. Guo, H. Xie, J. Shao, Z. Sun, W. Han, X. F. Yu, P. Li, P. K. Chu, *Angewandte Chemie - International Edition* **2016**, *55*, 5003–5007.

[44] J. Zhang, Y. Ma, K. Hu, Y. Feng, S. Chen, X. Yang, J. Fong-Chuen Loo, H. Zhang, F. Yin, Z. Li, *Bioconjugate Chem.* **2019**, *30*, 1658–1664.

[45] L. Wu, J. Wang, J. Lu, D. Liu, N. Yang, H. Huang, P. K. Chu, X.-F. Yu, *Small* **2018**, *14*, 1801405.

2 SURFACE FUNCTIONALIZATION OF BLACK PHOSPHORUS WITH NITRENES: IDENTIFICATION OF P=N BONDS BY USING ISOTOPIC LABELING

2.1 ABSTRACT

Surface functionalization of two-dimensional crystals is a key path to tuning their intrinsic physical and chemical properties. However, synthetic protocols and experimental strategies to directly probe chemical bonding in modified surfaces are scarce. Introduced here is a mild, surface-specific protocol for the surface functionalization of few-layer black phosphorus nanosheets using a family of photolytically generated nitrenes (RN) from the corresponding azides. By embedding spectroscopic tags in the organic backbone, a multitude of characterization techniques are employed to investigate in detail the chemical structure of the modified nanosheets, including vibrational, X-ray photoelectron, solid state ^{31}P NMR, and UV-vis spectroscopy. To directly probe the functional groups introduced on the surface, R fragments were selected such that in conjunction with vibrational spectroscopy, ^{15}N-labeling experiments, and DFT methods, diagnostic P=N vibrational modes indicative of iminophosphorane units on the nanosheet surface could be conclusively identified.

2.2 INTRODUCTION

Surface functionalization could provide an avenue to rationally tune the physico-chemical properties of two dimensional (2D) inorganic crystals and unlock their potential as next-generation electronic, catalytic, or quantum materials. Black phosphorus (bP), a 2D van der Waals material composed entirely of tricoordinate phosphorus, is a promising candidate for a range of applications, including field-effect transistors,[1,2] photodetectors,[3,4] and thermoelectric devices[5] due to its unique properties including a layer-dependent bandgap, high carrier mobility, and high current switching ratio.[6] Methods to chemically functionalize the bP basal plane that minimize lattice degradation (e.g. P–P bond cleaving) are rare, yet if available they could address key challenges limiting bP implementation, such as air stability, rational doping, or band gap tuning. Probing the integrity and structural changes of the bP nanosheets after functionalization is necessary to assess the effectiveness of any synthetic protocol tested, but experimental limitations in surface analysis hinder the conclusiveness of the information collected.

From a chemical standpoint, bP offers a unique synthetic avenue for its surface functionalization. In contrast to less reactive surfaces such as graphene or hexagonal boron nitride (h-BN), the availability of lone pairs in the basal plane makes exfoliated bP nanosheets amenable to mild and highly specific surface modification strategies, for example those employed in the chemistry of molecular phosphines. To date, efforts to covalently functionalize bP rely primarily on harsh conditions traditionally used to chemically modify h-BN or graphene, such as treatment with iodonium[7,8] and aryl diazonium salts.[9–11] This 'one-size fits all' approach to surface functionalization ignores the inherent chemical orthogonality of 2D nanomaterials. More recently, the Staudinger reaction[12] between black phosphorus and 4-benzoic acid azide was reported to produce functionalized nanosheets bearing iminophosphorane groups on the bP surface.[13] However, carried out at high temperatures for a prolonged period of time (140 °C, 40 h), this transformation led to significant chemical degradation of the nanosheets, making the assignment of iminophosphorane P=N bonding motifs circumstantial and challenging to distinguish from concurrent oxidation processes.

Herein we introduce a mild protocol, tailored to functionalize black phosphorus nanosheets, that relies on photolytically generated nitrenes (RN). To experimentally investigate the nature of the

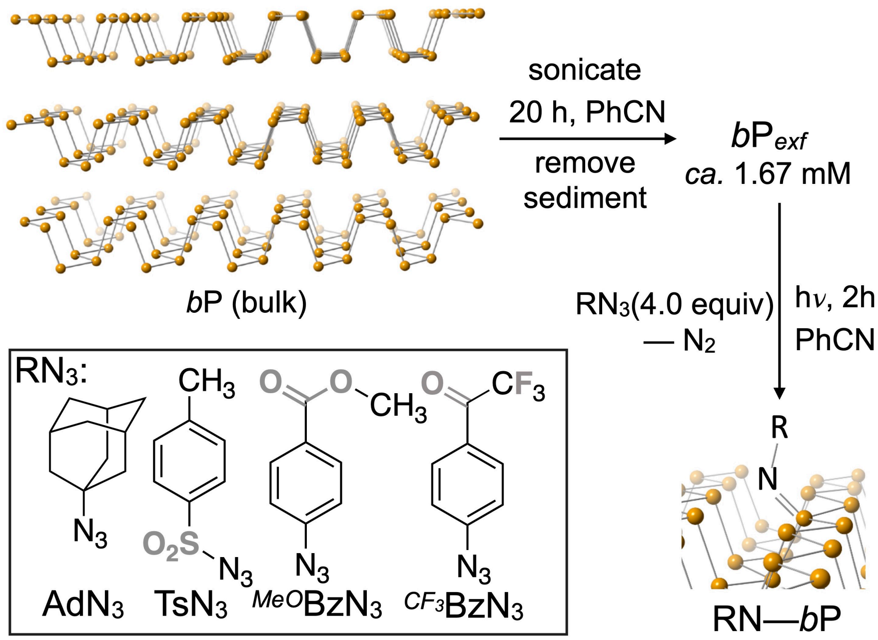

Figure 2.1. Functionalization of bP_{exf} with organic azides.

chemical bonding introduced on the bP surface, a family of parent organic azides was selected to include diagnostic spectroscopic signals associated with the organic (R) backbone. Specifically, tosyl (Ts), *p*-methoxycarbonylphenyl (^{MeO}Bz), 4-trifluoroacetylphenyl (^{CF_3}Bz), and adamantyl (Ad) azides were employed as nitrene sources under photolytic conditions (Figure 2.1). Post-functionalization, the nanosheets were characterized extensively using vibrational, X-ray (emission, photoelectron), NMR, and UV-vis spectroscopy. In contrast to prior claims,[13,14] we found most of these methods alone could not conclusively distinguish between adventitious oxidation and deliberate surface functionalization of bP. To directly probe chemical bonding in the modified surfaces, the organic substituents RN were judiciously chosen, such that in conjunction with vibrational spectroscopy, ^{15}N-labeling experiments, and DFT calculations, diagnostic P=N vibrational modes indicative of iminophosphorane units (P=NR) on the nanosheet surface could be directly and conclusively identified.

2.3 Results and Discussion

2.3.1 *Synthesis*

Finely crushed bP crystals were sonicated and centrifuged to remove large particles, producing dispersions of exfoliated black phosphorus nanosheets (bP_{exf}, *ca.* 1.67 mM, 50 mg/L at 2000 *g*). Extensive characterization reveals this process yields high-quality, minimally oxidized black phosphorus nanosheets that average 7–11 layers in thickness (Figures S2–3). Fresh dispersions of bP_{exf} were irradiated in the presence of an organic azide using a broadband UV lamp under rigorous air- and water-free conditions (Figure 2.1). During photolysis, the initial light brown dispersion takes a deep brown-red hue, typical of byproducts in reactions involving nitrenes.[15] Post-reaction, the functionalized nanosheets were isolated via filtration. Soluble byproducts were then removed by extraction with copious amounts of solvent.

2.3.2 *Binding Modes*

Multiple binding modes might occur between photolytically generated nitrenes[16] and accessible P sites on bP. The relative stability of three different binding modes of tosyl nitrene [TsN] to the basal phosphorus sites of a bP sheet were considered *in silico* using density functional theory

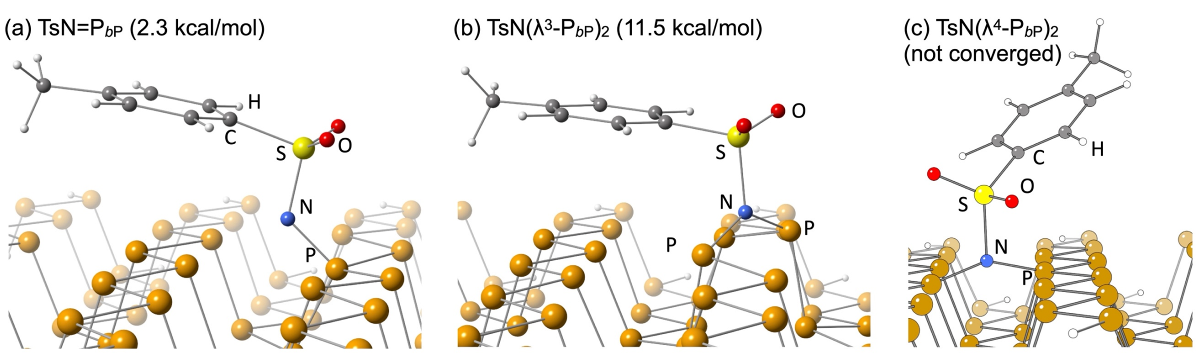

Figure 2.2. Three binding modes for tosyl nitrene binding to bP were evaluated in silico: (a) iminophosphorane TsN=P$_{bP}$, (b) bisphosphinoamine TsN(λ^3-P$_{bP}$)$_2$ and (c) TsN(λ^4-P$_{bP}$)$_2$.

(DFT): (a) the iminophosphorane $TsN{=}P_{bP}$, (b) the bisphosphinoamine $TsN(\lambda^3\text{-}P_{bP})_2$ (λ^3-P, trivalent P), and (c) the NP_4 heterocyclic structure $TsN(\lambda^4\text{-}P_{bP})_2$ (Figure 2.2 and **Error! Reference source not found.**). The direct reaction between a molecular phosphine and an azide typically results in the formation of a phosphazide, RN_3PR_3. Most often, phosphazides spontaneously extrude dinitrogen to form iminophosphoranes ($RN{=}PR_3$), which are also produced from the direct reaction between photolytically generated nitrenes and phosphines. The absence of N_3 vibrational modes in the experimental spectra of RN–bP (Figure 2.5a) indicates that if a phosphazide formed, it quickly lost N_2 and converted to other species such as an iminophosphorane $TsN{=}P_{bP}$ (Figure 2.2a). Molecular iminophosphoranes undergo facile 1,2-migrations;[17] on the bP nanosheet this transformation would result in nitrene group insertion into a P–P bond, giving rise to a PNP bisphosphinoamine bridge, (*i.e.* $TsN(\lambda^3\text{-}P_{bP})_2$; Figure 2.2b). *In silico*, we found the bisphosphinoamine to be energetically disfavored compared to the iminophosphorane. A third binding motif, in which the nitrene fragment bridges two phosphorus atoms located on neighboring ridges of the nanosheet forming an NP_4 heterocycle without cleaving any P–P bonds, was also evaluated (Figure 2.2c). Upon optimization, this $TsN(\lambda^4\text{-}P_{bP})_2$ structure was found to be unstable, converging instead to $TsN{=}P_{bP}$.

2.3.3 *Morphology and X-Ray Photoelectron Spectroscopy (XPS)*

Post-functionalization, the black phosphorus nanosheets maintain their structural integrity and laminar morphology, as evinced by solid state NMR and Raman spectroscopy (Figure A.2, Figure A.7) and visualized with scanning electron and atomic force microscopies, respectively (Figure 2.3a). The elemental composition of functionalized RN–bP was probed by XPS, revealing the presence of N, O, and C in addition to P (Figure A.3). In ^{CF_3}BzN–bP, fluorine was also detected, indicating the presence of [^{CF_3}BzN] surface groups. Although sulfur has a high photoemission

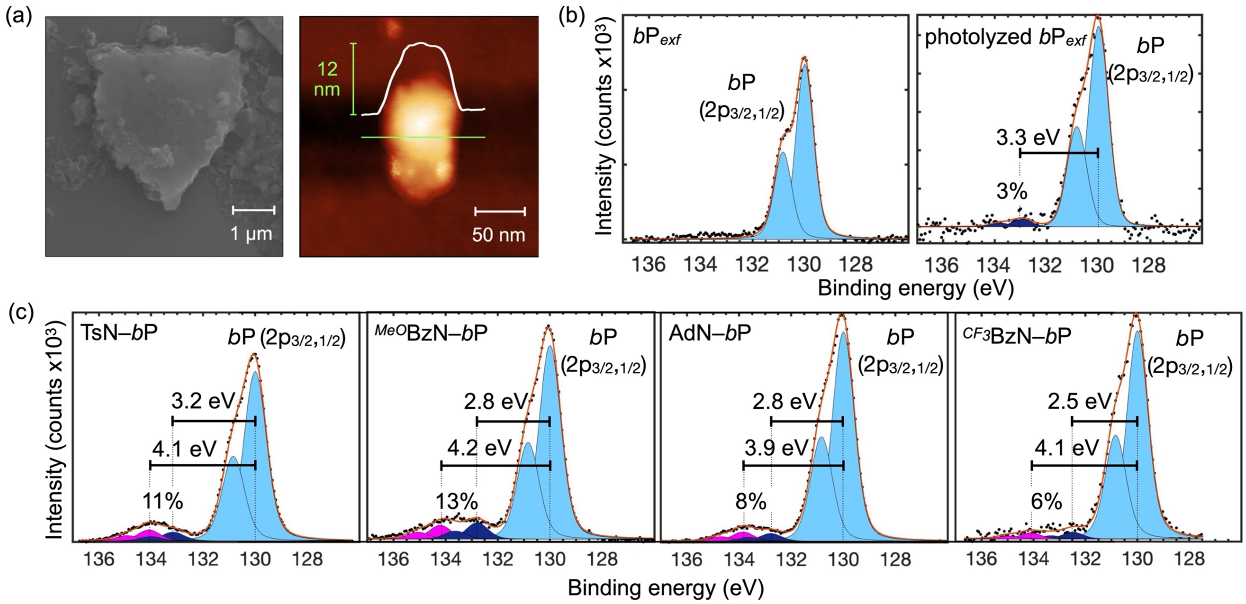

Figure 2.3. (a) Morphological characterization of TsN–bP by scanning electron and atomic force microscopy. P2p XPS spectra of (b) control samples and (c) azide functionalized nanosheets.

probability, strong bP plasmon satellites[19] obscure its detection in TsN–bP. High-resolution N1s XPS was obtained for all samples, but it cannot differentiate between the CN group of residual benzonitrile, with energies at 398.7 and 400.2 eV for its chemi- and physiosorbed states,[20] respectively, and PN binding environments, which occur between 398–401 eV (Figure A.5).[21] Successful functionalization is however corroborated by high-resolution C1s XPS. A binding environment corresponding to C=O is observed at *ca.* 288.5 eV in both ^{MeO}BzN–bP and ^{CF_3}BzN–bP at energies distinct from those associated with adventitious carbon or benzonitrile. Notably, the same feature is absent in TsN–bP or bP$_{exf}$, which do not contain a carbonyl group. Most notably, in ^{CF_3}BzN–bP, a C–F environment associated with the CF_3 unit is observed at 290.5 eV (Figure A.4).

Characterization of the functionalized nanosheets using high resolution P2p XPS reveals that in addition to the characteristic black phosphorus P(0) doublet at 130.0 eV, each derivative contains two new P chemical environments at higher energies, indicative of a higher oxidation state (Figure

2.3c). While the 132.8–134.2 eV energy range of the oxidized P is comparable to a previous assignment for a P=N bond at 134 eV,[13] an extensive literature survey[21] reveals that PN and PO environments cannot be distinguished using P2p XPS alone, as they occur over the same binding energy range of 130.9–136 eV (Figure A.5).[22,23] Consequently, we assign the two new P environments in RN–bP to P sites with an oxidation state greater than zero, which could include both PO and PN moieties. After accounting for the adventitious formation of phosphorus oxides observed in the control samples (*ca*. 3%), the remaining amount of oxidized phosphorus in RN–bP is attributed to PN bonds.

2.3.4 *X-ray Emission Spectroscopy (XES)*

Phosphorus Kα XES, a technique that probes the functionalization of the bulk material, corroborates the findings from the surface XPS measurements. XES analysis reveals that TsN–bP, ^{MeO}BzN–bP, and AdN–bP contain oxidized P sites with features at slightly higher energies (0.66–0.69 eV, Figure A.6) than for pristine bP, but like XPS, it cannot distinguish between PN and PO bonds.[24] XES analysis is highly dependent on the degree of exfoliation of the nanosheets, as thick flakes contain significantly more elemental, unoxidized phosphorus and fewer exposed surface sites accessible for functionalization. Thus, the percent bulk functionalization of the RN–bP samples was found to range from *ca.* 5 to 0.3%, a range comparable to other reports of bP functionalization.[13,14,25]

2.3.5 *Solid State NMR Spectroscopy*

The chemical bonding in the functionalized RN–bP (R = Ts, ^{MeO}Bz) nanosheets was probed extensively using a range of magic angle spinning (MAS) NMR spectroscopy techniques.

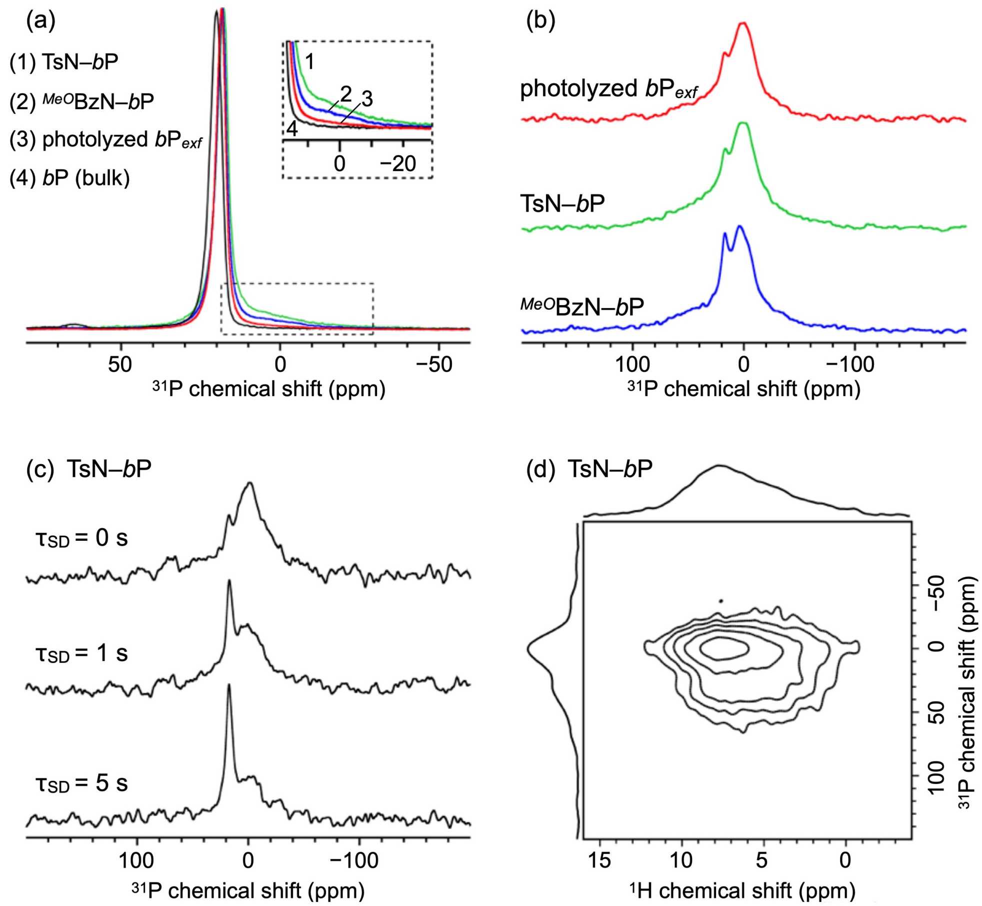

Figure 2.4. Characterization of control samples and functionalized nanosheets using (a) direct excitation ^{31}P solid state NMR, (b) $^{1}H \rightarrow ^{31}P$ CPMAS NMR, (c) $^{1}H \rightarrow ^{31}P$ CPMAS spin diffusion, and (d) $^{1}H\{^{31}P\}$ CP-HETCOR.

Direct excitation ^{31}P NMR spectroscopy analysis of bulk bP, bP$_{exf}$, photolyzed bP$_{exf}$, and RN–bP reveals a single, intense peak associated with the bP lattice (Figure 2.4a). For the bulk sample, this singlet is centered at 20 ppm, within the previously reported range of 19–22 ppm.[13,14,26,27] After exfoliation and functionalization with TsN_3 or $^{MeO}BzN_3$, the maximum of this peak shifts to 18 ppm. A decrease in chemical shift upon reduction of particle size has been reported for many other semiconductors, and usually occurs as a result of an increase in the band gap, which in turn leads to reduced paramagnetic deshielding, increased nuclear shielding, and a more negative chemical shift.[28,29] The spectra collected for the bP_{exf} and photolyzed bP_{exf} control samples are very similar, though in the latter case, we detect a slight broadening and a shift to a higher frequency (Figure A.2).

Most notably, functionalization of the nanosheets is associated with the emergence of a broad shoulder extending from *ca.* 20 ppm to –20 ppm (Figure 2.4a, inset). A similar feature, assigned to P=N bonds, was reported after the thermolysis of bP with benzoic acid azide.[13] In this study, we found that a small shoulder is also present in the photolyzed bP_{exf} control sample, though of reduced intensity compared to the azide-functionalized nanosheets. Hence, we propose this feature arises not only from P atoms bonded or nearby to [RN] groups, but also from adventitious oxidation of bP during photolysis (e.g. PO or PC bonds). Considering the quantitative nature of the direct excitation ^{31}P NMR spectra, the intensity of the shoulder feature can be correlated to the concentration of PO and PN moieties within each sample, which mirrors that observed by P2p XPS (Figure 2.3b, c).

^{1}H→^{31}P cross-polarization magic angle spinning (CPMAS) NMR spectroscopy was employed to selectively probe ^{31}P NMR signals arising from P atoms bound to, or within *ca.* 5 Å of any functional groups on the nanosheets. Although significantly different when analyzed using P2p XPS (Figure 2.3) and IR spectroscopy (Figure 2.5), the photolyzed bP_{exf} control and functionalized RN–bP samples give rise to very similar ^{31}P CPMAS NMR spectra (Figure 2.4b). Both samples feature two peaks, one stemming from pristine lattice phosphorus sites, and another, more intense and broader peak, centered at 0 ppm. The enhanced intensity of the latter signal implies that it originates from ^{31}P spins located within a few Å of ^{1}H spins. However, its presence in both RN–bP and the photolyzed control sample reveals it also stems from adventitious oxidation, and not exclusively from deliberate functionalization. Importantly, bP_{exf} nanosheets that were not photolyzed show no observable signal using this technique, indicating that the concentration of the oxidized sites in bP_{exf} is at least an order of magnitude smaller before photolysis than in the photolyzed bP_{exf} or RN–bP (Figure A.2). Due to the breadth of the ^{31}P NMR signals observed in the CPMAS spectra, it is possible that the ^{1}H spins providing the observed magnetization arise from terminations other than the RN group, such as P–OH or P–CH that might form during photolysis. This interpretation is corroborated by the presence of O–H and C–H stretches in the IR spectra of TsN–bP, ^{MeO}BzN–bP, and the photolyzed bP_{exf} control (Figure 2.5a).

^{31}P CP spin diffusion experiments were conducted to confirm the oxidized P sites giving rise to the feature at 0 ppm are located on the nanosheets, rather than belonging to a phase-segregated oxidized impurity. The initial ^{31}P magnetization was generated in the $^{1}H{\rightarrow}^{31}P$ CP step, then it was stored for a variable spin diffusion time period (τ_{SD}) ranging from 0 to 5 s. During τ_{SD}, ^{31}P–^{31}P dipolar couplings cause transfer of magnetization between spatially proximate ^{31}P spins. After τ_{SD}, the ^{31}P longitudinal magnetization is converted to transverse magnetization by a $\pi/2$ pulse and observed. The ^{31}P spin diffusion spectra reveal that as τ_{SD} is increased, the NMR signal intensity is transferred from oxidized ^{31}P NMR signals to the bulk, zerovalent bP ^{31}P NMR signals (Figure 2.4c). This observation confirms that the ^{31}P NMR signals at 0 ppm arise from oxidized P sites located on the bP sheets, and not from a phase-segregated, oxidized impurity (e.g. molecular phosphorus oxides).

Finally, to probe the chemical identity of the functional groups attached to the nanosheets, the chemical shifts of H atoms proximate to the oxidized P sites were determined using $^{1}H\{^{31}P\}$ CP heteronuclear correlation (HETCOR) experiments, which correlate ^{1}H to ^{31}P chemical shifts in a two-dimensional map, as depicted in Figure 2.4d. The HETCOR spectrum of TsN–bP shows that the ^{1}H spins involved in the CP magnetization transfer have distinct ^{1}H chemical shifts, with broad

^{1}H signals centered at *ca.* 8 and 6 ppm. We note that the $^{1}H\{^{31}P\}$ HETCOR spectrum of an intentionally oxidized sample of bP_{exf} appears very similar to that of TsN–bP (Figure A.1). This finding reaffirms that adventitious oxidation precludes the unambiguous detection of TsN-functionalized phosphorus in these experiments. The observation of distinct sets of ^{1}H chemical shifts (at 8 and 6 ppm, respectively) for each type of ^{31}P NMR signal is somewhat surprising because the ^{31}P spin diffusion experiments described above suggest that all the ^{31}P spins in those experiments are spatially proximate. Since ^{31}P spin diffusion experiments probe larger length scales (10's of Å) than CP experiments (*ca.* 5 Å), the HETCOR spectrum indicates that the bulk ^{31}P spins (with a chemical shift of 20 ppm) and the oxidized ones (with a chemical shift of 0 ppm) derive their ^{1}H magnetization in the CP experiment from different sets of ^{1}H spins. For example, the bulk, basal P atoms might be proximate to an RN group or to adsorbed solvent, while the oxidized P sites could be localized on the edges of the nanosheets and bound to OH groups. Furthermore, a dipolar ^{1}H double-quantum single-quantum (DQ–SQ) NMR spectrum of TsN–bP shows that the ^{1}H spins are only strongly dipole coupled (within *ca.* 3 Å) to ^{1}H spins with the same chemical shifts (Figure A.1). All of these observations are consistent with the hypothesis that there are distinct clusters of ^{1}H spins where the chemical shift within a group is very similar, and strongly suggests that the oxidized P atoms detected are localized on the edges of the nanosheets.

In summary, ^{1}H and ^{31}P solid state NMR spectroscopy confirm that the structure of bP is largely unaltered during exfoliation and functionalization. Comparison of direct excitation ^{31}P solid state NMR spectra suggests that the ^{31}P NMR signals centered at 0 ppm can be partly, but not exclusively, attributed to P atoms bound to or in the vicinity of [NR] organic functional groups. Indeed, ^{31}P CPMAS and CP spin diffusion experiments suggest the bP sheets are partially oxidized during photolysis and contribute to the ^{31}P NMR signals at 0 ppm. Ultimately, the relative intensity of the NMR signals corresponding to adventitious oxidation in the ^{31}P CPMAS spectra makes selective observation of P atoms that are bonded or in close proximity to the organic functional groups challenging.

2.3.6 *Infrared Spectroscopy (IR) and ^{15}N Labeling*

To investigate the nature of the bonding between the nitrene and the nanosheet surface, we turned to IR spectroscopy — a technique uniquely poised to distinguish between P(NR) and PO environments. IR has been previously used to probe the surface functionalization of 2D-nanosheets,[11,30] but to the best of our knowledge it has never been used to identify the formation of more complex, higher order bonding on these surfaces. Here, the chemical association of the

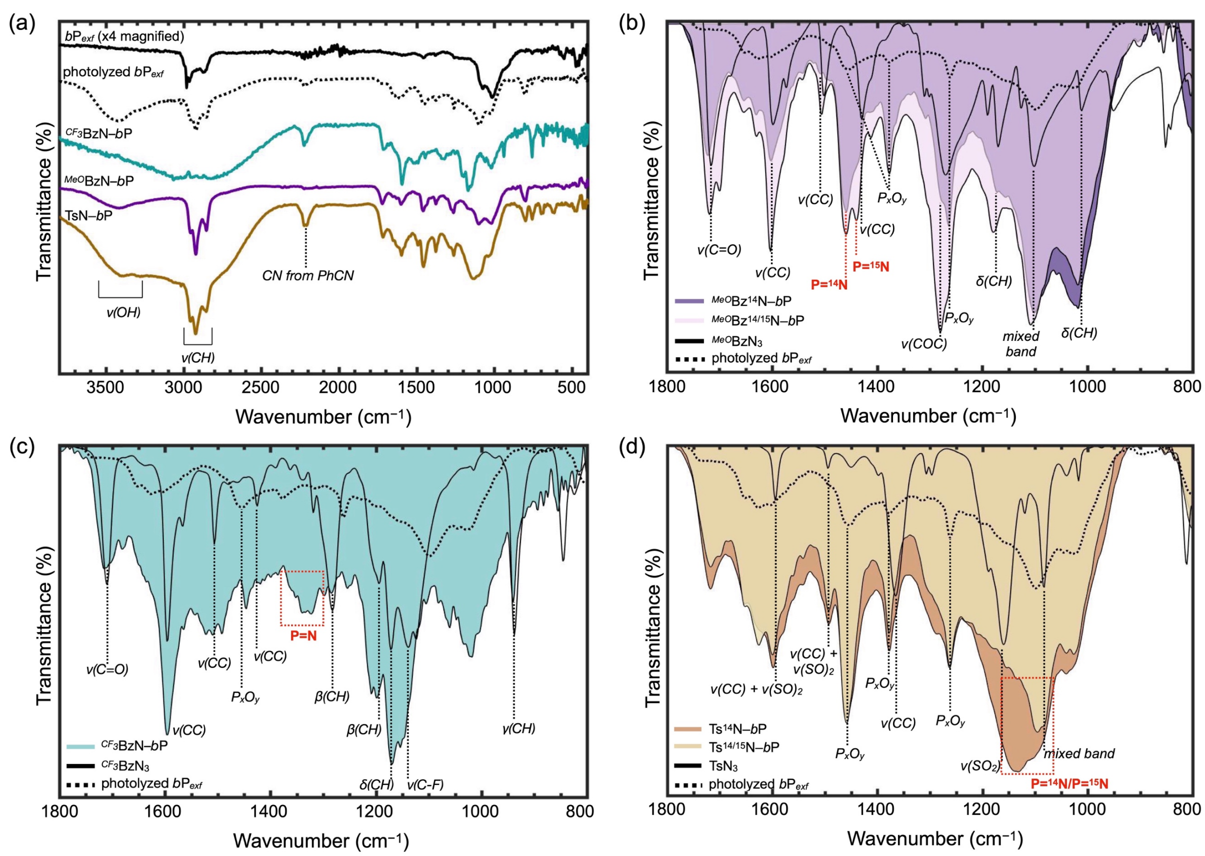

Figure 2.5. IR characterization of (a) RN–bP functionalized nanosheets and control samples, (b) ^{MeO}BzN–bP and ^{MeO}Bz$^{14/15}$N–bP, (c) ^{CF_3}BzN–bP, and (d) TsN–bP and Ts$^{14/15}$N–bP.

[NR] group with bP to form iminophosphorane RN=P_{bP} linkages was investigated for the three R groups with distinctive IR signatures, Ts, ^{MeO}Bz, and ^{CF3}Bz. Together with DFT calculations, ^{15}N isotopic labeling experiments were employed to identify the presence of P=N vibrational modes on the functionalized nanosheets.

Post-functionalization, the nanosheets exhibit distinct new vibrational signals between 1700–1000 cm^{-1} that are associated with the backbone of the [NR] nitrene group (Figure 2.5a). These vibrations are distinct from those associated with adventitious bP oxidation, which were assessed by IR characterization of the photolyzed bP_{exf} control (Figure 2.5a). Notably, all three RN–bP derivatives exhibit a systematic 2–7 cm^{-1} blue-shift in the vibrational modes of the organic moiety compared to the parent azide, implying a change in the chemical environment of the [NR] unit post-functionalization. The functionalized nanosheets contain no unreacted organic azide, or tetrazoles that might have resulted from reaction with benzonitrile.[31,32] In addition, N–H stretches that might stem from physio- or chemisorbed RNH_2 amine were also not detected in the functionalized samples (Figure A.8).[33] ^{MeO}BzN–bP shows strong features corresponding to the C=O (1723 cm^{-1}), C=C (1603 cm^{-1}), and C–O–C (1280 cm^{-1}) vibrational modes of the [^{MeO}BzN] backbone (Figure 2.5b).[34] Similar C=O (1715 cm^{-1}) and C=C (1597, 1509 cm^{-1}) vibrational modes are also observed in ^{CF3}BzN–bP along with a strong C–F stretching mode at 1146 cm^{-1} (Figure 2.5c). TsN–bP, features new signals associated with mixed $\nu(CC) + \nu(SO_2)$ and $\nu(SO_2)_{sym}$ vibrational modes observed at 1599, 1492, and 1155 cm^{-1}, respectively (Figure 2.5d).

Although relatively intense, P=N stretches can be challenging to locate as they span a surprisingly wide range of frequencies, from *ca.* 1500 to 1055 cm^{-1}.[35] Because the substituent on the nitrogen is the strongest determinant of the P=N vibrational energy,[36] molecular iminophosphoranes can be used to estimate the position of the PN vibration for RN=P_{bP}. Thus, a family of triphenylphosphine-based molecular iminophosphoranes $RN{=}PPh_3$ (R = Ts, ^{MeO}Bz, ^{CF_3}Bz) was selected as a model system, and their vibrational profiles calculated (Figure A.10). The P=N stretch for $TsN{=}PPh_3$ is located at 1147 cm^{-1} (experimental)[36] and 1135 cm^{-1} (predicted). For $^{MeO}BzN{=}PPh_3$ and $^{CF_3}BzN{=}PPh_3$, the PN stretch is comparatively more intense and blue-shifted to 1387 and 1399 cm^{-1}, respectively, ostensibly due to coupling with an N–Ph stretch and a phenyl ring deformation mode (Figure A.10). Inspecting the experimental spectra obtained for RN–bP against the predicted ranges for P=N stretches, we can indeed identify intense features in these regions. For example, ^{MeO}BzN–bP and TsN–bP each contain an intense vibration at 1459 and 1120 cm^{-1}, respectively, not associated with the organic backbone or bP oxidation). Calculations predicted that formation of a bisphosphinoamine in the reaction between tosyl nitrene and the bP surface is energetically disfavored compared to the iminophosphorane $TsN{=}P_{bP}$. Experimentally, no vibrational modes corresponding to P–N single bonds of bisphosphinoamines could be identified in the IR spectra collected for ^{MeO}BzN–bP and TsN–bP (Figure A.8).

To unequivocally assign the P=N vibrations in the complex IR spectra of the functionalized nanosheets, the organic nitrene [RN] unit was isotopically enriched with ^{15}N, and the effect of the isotopic shift on the spectra analyzed. ^{15}N-labeling experiments were performed using enriched $^{MeO}Bz^{14/15}N_3$ and $Ts^{14/15}N_3$ azides obtained from terminally labeled $Na^{15}N^{14}N_2$. The [RN] groups incorporated in the nanosheets will contain therefore an equal ratio of ^{14}N and ^{15}N. If formed, the iminophosphorane moieties $RN{=}P_{bP}$ are expected to give rise to a set of both $^{14}N{=}P$ and $^{15}N{=}P$ vibrational modes. Inspecting the changes incurred in the IR spectrum of labeled ^{MeO}BzN–bP, we note that in addition to a prominent feature at 1459 cm^{-1}, a new signal emerges at 1439 cm^{-1}. We attribute this set of features to the $P{=}^{14}N$ and $P{=}^{15}N$ stretches, respectively. In close agreement with the experiment, a simple harmonic oscillator approximation estimates the energy of the $P{=}^{15}N$

stretch at 1425 cm^{-1}. Although occurring at a higher frequency than the PN bond predicted for the molecular iminophosphorane ^{MeO}BzN=PPh_3 of 1387 cm^{-1}, the vibration is within the expected energy range for an N-phenyl substituted PN unit.[37]

Similarly, ^{15}N isotopic labeling of TsN–bP led to the appearance of an intense and broad feature centered at 1094 cm^{-1}, red-shifted from that assigned to the P=^{14}N bond at 1120 cm^{-1}. The isotopic shift of 26 cm^{-1} is in perfect agreement with that predicted using a harmonic oscillator approximation, and the frequency of the observed stretch lies very close to that measured for the molecular iminophosphorane TsN=PPh_3 of 1147 cm^{-1}.[36] Isotopic labeling was not performed for the ^{CF_3}BzN–bP derivative, but the P=N stretch is expected to occur at a similar energy to that observed for ^{MeO}BzN–bP. Inspection of the vibrational spectrum of this derivative reveals the presence of a broad signal at 1332 cm^{-1}, a likely candidate for the P=^{14}N stretch (Figure 2.5c). The broadness of the P=N vibrational mode in both the TsN–bP and ^{CF_3}BzN–bP derivatives can be attributed in part to the cluster of closely spaced vibrational modes involving the PN bond proximate to the primary P=N stretch (Figure A.10).

In conclusion, combining vibrational spectroscopy, isotopic labeling, and DFT modeling enabled the direct and conclusive identification of iminophosphorane P=N linkages on the surface of the azide-functionalized bP nanosheets.

2.3.7 *Ambient Stability*

Surface[38] or edge[26] functionalization has been previously explored as a strategy to increase the ambient stability of bP dispersions. Notably, functionalization of bP using *p*-benzoic acid azide, with the proposed formation of P=N linkages on the bP surface was also reported to increase its

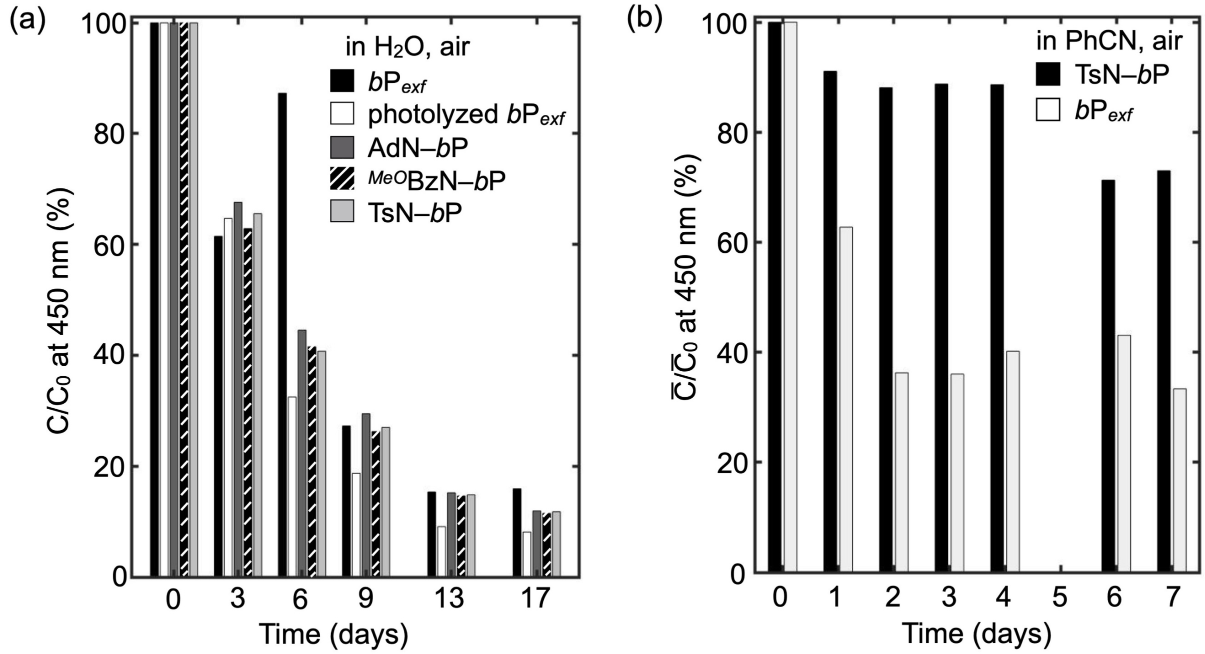

Figure 2.6. UV-vis spectroscopy in water and benzonitrile. (a) Bar graph depicting the similar evolution of the normalized concentrations (C/C_0, C_0 = concentration at t=0) of RN–bP and control samples in H_2O, under ambient conditions. (b) Bar graph of the concentrations measured for ambiently exposed samples plotted in (c), divided by the corresponding concentrations for samples stored under N_2 ($\overline{C}/\overline{C}_0$, $\overline{C} = C(air)/C(N_2)$).

ambient stability in water,[13] a surprising result considering RN=P bonds are prone to hydrolyze to phosphine oxides and amines.[39]

Herein, we developed a protocol to test the ambient stability of the functionalized nanosheets that accounts for aggregation and sedimentation of the nanosheets during the study, as well as for hydrolysis. The electronic absorption profile of RN–bP dispersions in water or benzonitrile was monitored in the presence and absence of oxygen. Furthermore, after exposure to ambient conditions, the functionalized nanosheets were isolated and analyzed by P2p XPS to probe the chemical evolution of the samples. In brief, when the nanosheets were suspended in deionized water under ambient conditions, no increase in the stability of functionalized RN–bP (R = Ad, ^{MeO}Bz, Ts) nanosheets compared to the control bP samples was observed using UV-vis spectroscopy (Figure 2.6a, b). This result is consistent with reports of facile P=N bond hydrolysis in molecular analogs of nitrene-functionalized bP, but in contrast to the reported stability of bP nanosheets functionalized thermally with *p*-benzoic acid azide.[13]

To determine if nitrene functionalization of bP increases its ambient stability we sought to minimize hydrolysis of the P=N linkages by using an aprotic organic solvent (PhCN). The concentration of the dispersed functionalized and pristine nanosheets was monitored by UV-vis spectroscopy while either kept under rigorous air- and water-free conditions in a nitrogen glovebox, or, in parallel, exposed to ambient conditions (Figure 2.6c, d). Firstly, aggregation and sedimentation of the nanosheets is responsible for a significant drop in the overall concentrations of the functionalized TsN–bP and control bP_{exf} dispersions, and this decrease is more pronounced for the unfunctionalized bP_{exf} sample (Figure 2.6c). Secondly, the concentration of the TsN–bP dispersion is less affected by ambient exposure than the control bP_{exf} sample (Figure 2.6d).

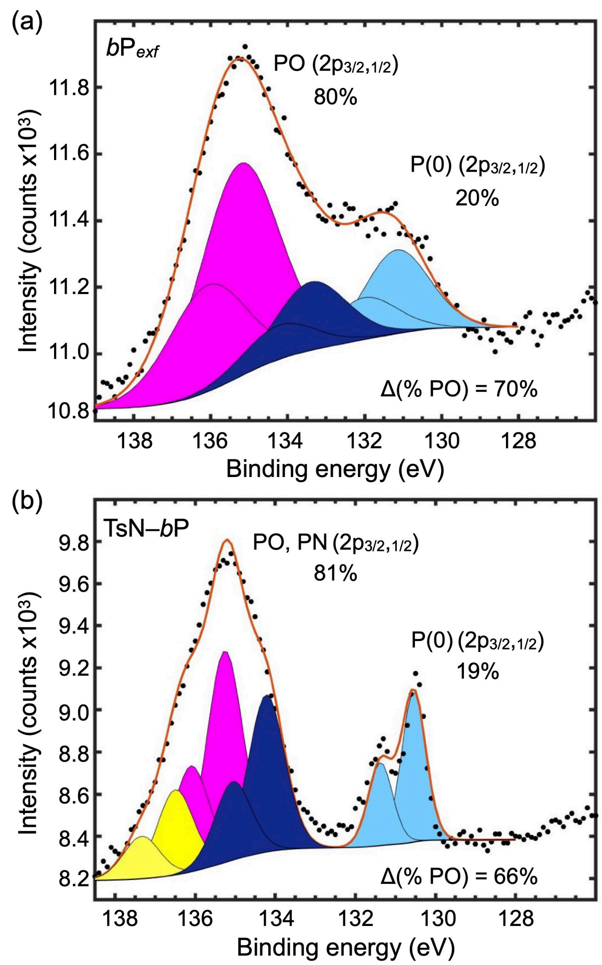

Figure 2.7. P2p XPS analysis of (a) bP_{exf} and (b) TsN–bP nanosheets isolated from PhCN dispersions after seven days of ambient exposure. Δ(% PO) indicates the increase in the amount of oxidized P with ambient exposure.

To probe if the changes in absorbance are actually indicative of a smaller degree of ambient degradation of TsN–bP, after completion of the UV-vis measurement studies, the functionalized TsN–bP and control bP_{exf} nanosheets were analyzed by P2p XPS (Figure 2.7, Figure A.9). The data revealed a significant and comparable increase in oxidation in both the TsN–bP and control samples during 7 days of ambient exposure. This result is at odds with the UV-vis data which suggests a significantly smaller degree of oxidation occurs in the functionalized sample. Though qualitative, this experiment suggests that the effect of RN functionalization on the ambient stability is minor, even if analysis of the UV-vis data alone would suggest differently.

2.4 Conclusion

In conclusion, we report a mild functionalization protocol for bP that leverages the unique network of lone pairs in the basal plane of this 2D inorganic material. A family of organic azides was selected to include a range of spectroscopic handles (*i.e.* vibrational, XPS, NMR) that facilitated probing in detail the chemical bonding of the modified nanosheets using a wide range of experimental techniques. Our studies revealed that most spectroscopic techniques employed could not conclusively distinguish between adventitious oxidation and deliberate functionalization. To circumvent this limitation, we demonstrate that P=N bonds can be directly identified on the modified bP surface using vibrational spectroscopy in conjunction with ^{15}N labeling and DFT studies. In contrast to prior claims, we also found that UV-vis spectroscopy is not a reliable method to assess enhanced ambient stability of the functionalized black phosphorus nanosheets. In aggregate, this study illustrates how molecular synthetic and characterization strategies can be translated to provide an unprecedented level of chemical control and structural detail in the modification and characterization of 2D inorganic materials.

2.5 EXPERIMENTAL

2.5.1 *Materials*

Unless stated otherwise, all work was performed under an inert atmosphere of N_2 using a Schlenk line or an LC Technology Solutions, Inc. glovebox containing <5 ppm H_2O and O_2. Benzonitrile (99%, Alfa Aesar) was degassed for several hours under vacuum and stored over 3 Å molecular sieves for a minimum of 2 days prior to use. Additional anhydrous solvents were obtained from a SciMatCo solvent system and stored over 3 Å molecular sieves (Thermo-Fisher) for at least 12 h before use. Molecular sieves were previously activated by heating at 250 °C under vacuum for a minimum of 3 days. All water used for ambient stability experiments was deionized, and Ultra-Pure Milli-Q water with a resistivity of >18 MΩ·cm was used as specified. Black phosphorus (*b*P) crystals (99.998%, Smart Elements) were purchased and used as received, or synthesized using a literature protocol.[40] All glassware was dried overnight at 150 °C prior to use.

All azides were stored in the dark in the glovebox freezer (−35 °C) and thawed at room temperature prior to use. NaN_3 (>99.5%, Sigma-Aldrich), $Na^{15}N^{14}N_2$ (>98%, Cambridge Isotope Laboratories), 1-azidoadamantane (AdN_3, 97%, Sigma-Aldrich), and methyl 4-aminobenzoate (98%, Aldrich) were used as received. *p*-Toluenesulfonyl azide (TsN_3), methyl 4-azidobenzoate ($^{MeO}BzN_3$), and 1-(4-azidophenyl)-2,2,2-trifluoroethanone ($^{CF_3}BzN_3$) were synthesized using literature protocols.[41–43]

Ultrasonication was performed using a 110W bath sonicator at 40 kHz that was maintained at 22−28 °C using circulation cooling. Centrifugation was performed using Nalgene™ Oak Ridge High-Speed Centrifuge Tubes sealed with O-ring caps. Filtrations were performed using EMD Millipore Omnipore hydrophobic membrane filters with a pore size of 0.2 µm. Photolytic treatments were performed with a 450 W medium-pressure mercury vapor lamp (Hanovia Specialty Lighting, PC 451.050) emitting 200–400 nm broadband radiation. The lamp was hosted inside a quartz jacket that was continuously cooled using an automated water circulator.

2.5.2 *Instrumentation*

Attenuated total reflectance infrared (ATR-IR) spectra were recorded on a Bruker Alpha IR instrument equipped with a Platinum ATR accessory. Diffuse reflectance infrared Fourier transform spectroscopy (DRIFTS) was used in some analyses with the corresponding Bruker DRIFTS accessory and FTIR-grade potassium bromide (KBr, >99%; Alfa Aesar). Raman spectra were acquired on a Renishaw InVia microscope using a 532 nm diode-pumped solid-state laser and a 50x microscope objective. UV–vis–NIR spectra were acquired using a Varian Cary 5000 UV–vis–NIR double-beam spectrophotometer. XRD spectra were acquired on a Bruker D8 Discover powder X-ray diffractometer with a large-area Pilatus 100K large-area 2D detector under ambient conditions. Scanning electron microscope images were obtained on a FEI Sirion XL30 Scanning Electron Microscope (SEM). Images were acquired at 11,227x magnification with an accelerating voltage of 15 kV and a working distance of 5 mm. XPS/ESCA analysis was performed on a Surface Science Instruments (SSI) S-Probe system under ultrahigh vacuum with a monochromatized Al Kα X-ray source and a low energy electron flood gun for charge neutralization (Figure 2.3, Figure 2.7, Figure A.3, Figure A.4). XPS of materials for ambient stability (Figure 2.7, Figure A.9) was collected on a Kratos Axis-Ultra DLD spectrometer with a monochromatized Al Kα X-ray and a low energy electron flood gun for charge neutralization under ultrahigh vacuum. AFM images were measured in non-contact mode on an Asylum Research Cypher atomic force microscope under a flow of N_2. All images were acquired using electrically conductive Cr/Pt AFM probes. For spectroscopic analysis (XPS, XES, Powder-XRD, and Raman), test-grade Si wafers (University Wafer) and Au-coated Si wafers (100 nm Au, Platypus Technologies) were cut, rigorously washed by sequential ultrasonication with detergent (Si only), water (Si only), acetone, and isopropanol, and then oven-dried overnight at 150 °C prior to use. Suspensions of various *b*P products in dichloromethane (DCM) or tetrahydrofuran (THF) were drop-cast onto clean silicon wafers and annealed for 2–5 min at 80 °C before analysis. XPS analyses were conducted using identical preparations with clean silicon or Au-coated Si wafers.

Phosphorus Kα XES measurements were performed using a recently developed laboratory spectrometer described in detail by Holden *et al*.[44] Phosphorus speciation by Kα XES using the spectrometer was demonstrated in Stein et al.[45] The spectrometer uses a low-power, 50 Watt Pd-anode X-ray tube (Varex) to stimulate fluorescence in the sample. The fluorescence is analyzed in the Dispersive Refocusing Rowland (DRR) geometry using a cylindrically bent, Si (111) Johann crystal analyzer with a 10 cm-radius of curvature (XRSTech). The analyzed rays are detected using an energy-resolving CMOS-based color X-ray camera.[46] The spectrometer is contained in a vacuum chamber which is evacuated to a pressure of <100 mTorr during measurements. The bP samples were prepared for XES measurement by drop-casting a dispersion of nanosheets in DCM or THF onto silicon wafers with an approximate sample spot area of ~3−4 mm in diameter. The prepared samples were stored under inert atmosphere and briefly exposed to air (<5 minutes) during loading into the spectrometer. The uncertainty in the energy scale is *ca.* ±0.02–0.03 eV.

Analysis of the XPS spectra acquired with the SSI S-probe system was performed using Esca Hawk7 software followed by analysis of the high-resolution P2p spectra using linear combination fitting with the nonlinear least-squares fitting Python package LMFIT (Figure 2.3, Figure 2.7, Figure A.3, Figure A.4).[47] XPS of materials for ambient stability acquired with the Kratos Axis-Ultra DLD system (Figure 2.7, Figure A.9) were analyzed using CasaXPS software. All binding energies were referenced to adventitious carbon (B.E.[C 1s] = 285.0 eV). Shirley baselines were subtracted from spectra prior to analysis. Paired pseudo-Voigt profiles representing the (P $2p_{3/2}$, P $2p_{1/2}$) doublet were fit to baseline-subtracted data with a fixed peak separation of 0.84 eV and relative ratio of 2:1, consistent with reported values for phosphorus.[48] To fit multiple P peak shapes, widths of subsequent signals were constrained to the width of the (P $2p_{3/2}$, P $2p_{1/2}$) pair. Relative contributions of each unique peak shape were measured according to the relative intensity of the signal. The center of the P $2p_{3/2}$ signal was fixed to 130.0 eV for comparative analysis. The percent composition of oxidized phosphorus was found to vary between RN–bP samples prepared through the same method, but on separate days. For example, four independent P2p measurements of TsN–bP samples produced through the same method, but on separate days gives an average of 8±2% oxidized phosphorus. As a result, these percentages are considered to be estimates.

Solid state NMR experiments were performed on a Bruker wide-bore 9.4 T ($\nu_0(^1H)$ = 400 MHz) NMR spectrometer with a Bruker Avance III HD console equipped with a Bruker 2.5 mm HXY MAS probe. The ^1H solid state NMR spectra were referenced to neat tetramethylsilane using adamantane ($\delta_{iso}(^1H)$ = 1.82 ppm) as a secondary chemical shift reference. ^{31}P NMR spectra were indirectly referenced using previously published relative NMR frequencies.[49] All solid-state NMR spectra were obtained with a magic angle spinning (MAS) frequency of 25 kHz. For all ^1H NMR spectra the radiofrequency (rf) fields for the $\pi/2$ pulses was 100 kHz. The recycle delay of the ^1H solid state NMR spin echo spectra was between 1.5 s to 2 s, and 32 scans were collected. The ^1H–^1H dipolar double quantum single quantum homonuclear correlations were obtained with back to back (BABA) recoupling.[50–52] The ^1H–^1H DQ-SQ NMR spectra were obtained with recycle delays of 1.1–1.7 s, 16 scans, and 80-96 indirect dimension points. All ^{31}P NMR spectra were obtained with SPINAL-64[53] ^1H decoupling applied during the acquisition and the rf field for the ^{1}H decoupling was 100 kHz. The ^{31}P direct excitation 1D NMR spectra were obtained with rf fields for the ^{31}P $\pi/2$ and π pulses of 93–125 kHz with 16–128 scans and recycle delays between 120 s to 287 s. For the cross-polarization (CP) NMR experiments,[54] the ^{1}H and ^{31}P rf fields for CP spin lock pulse were 73 kHz and 37.5 kHz, respectively, and recycle delays were between 1.1–1.7 s. ^{1}H saturation recovery experiments were used to measure ^{1}H T1 for each sample and select the appropriate recycle delay for the CPMAS experiments. The ^{31}P CP spin echo experiments were obtained with a CP contact time of 2–8 ms, recycle delay between 1.3 s to 1.9 s, and 2048–8192 scans. For the ^{31}P CP spin diffusion experiments,[55] the ^{31}P spin diffusion time was varied between 0–5 s and 128–1028 scans were acquired for each time point. The $^{1}H\{^{31}P\}$ CP-HETCOR spectra[56] were obtained with a forwards CP contact time of 3–8 ms, backwards CP contact time of 2–8 ms, 128–256 scans, and 40–64 indirect dimension points.

2.5.3 *Synthesis of ^{15}N-labeled organic azides*

Caution: Sodium azide forms hydrozoic acid (HN_3), a volatile, highly toxic, and explosive compound, when combined with acids or water. Proper safety precautions should be taken during workup and waste disposal to avoid HN_3 formation.

Synthesis of ^{15}N-labeled *p*-toluenesulfonyl azide ($TsN_2{}^{15}N/Ts^{15}NN_2$)

Synthesis adapted from literature.[41] To a 50-mL pear-shaped flask containing a solution of $Na^{15}NN_2$ (135 mg, 2.05 mmol, 1.02 equiv) in water (1 mL), TsCl (381 mg, 2.0 mmol, 1 equiv) was added as a solution in anhydrous acetone (5 mL). The flask was covered with aluminum foil and the solution was stirred for 16 h at room temperature. Acetone was removed *in vacuo*, and the resulting residue was washed with DCM (3 mL) and water (1 mL). The aqueous extracts were washed again with DCM (2 mL), and the organic extracts were combined and dried over anhydrous

Na_2SO_4. The volatiles in the filtrate were removed under vacuum to afford the product as a white powder (360 mg, 1.82 mmol, 90% yield). IR (ATR): $\nu_{asym}(N_2{}^{15}N)$ = 2102, 2122 cm^{-1}.

Synthesis of ^{15}N-labeled methyl 4-azidobenzoate ($^{MeO}Bz^{15}NN_2$ / $^{MeO}BzN_2{}^{15}N$)

In a protocol adapted from literature,[57] methyl 4-aminobenzoate (171 mg, 1.13 mmol, 1 equiv) was loaded into a 25-mL pear-shaped flask and dissolved in diluted HCl (0.2 M, 5 mL). Additional water (2 mL) was added to aid dissolution, and the flask was sealed with a rubber septum. After cooling to 0 °C, $NaNO_2$ (79 mg, 1.14 mmol, 1.01 equiv) was dissolved in deionized water (2 mL) and added dropwise *via* syringe to the benzoate solution. $Na^{15}NN_2$ (75 mg, 1.14 mmol, 1.01 equiv) in water (1 mL) was then added dropwise *via* syringe, and the mixture was diluted with 9 mL water. After 30 minutes of stirring, the mixture was removed from the bath and allowed to warm to room temperature. The crude reaction mixture was washed with Et_2O (2 x 10 mL) and water (1 x 10 mL), and then dried over anhydrous Na_2SO_4, filtered, and placed under vacuum. The resulting light beige powder was dissolved in Et_2O (10 mL), filtered through a plug of anhydrous silica gel, and dried under vacuum to yield spectroscopically pure product (156 mg, 0.88 mmol, 78%). IR (ATR): $\nu_{asym}(N_2{}^{15}N)$ = 2070, 2118 cm^{-1}, ν(C=O) = 1718 cm^{-1}.

2.5.4 *Synthesis and characterization of exfoliated black phosphorus nanosheets*

Crystals of black phosphorus (bulk bP; 60 mg) were finely crushed with an agate mortar and pestle. The resulting fine, silver-black powder was subsequently sonicated in the dark for 20 h in anhydrous benzonitrile (120 mL). Air-free 250-mL Schlenk flasks sealed with Teflon stoppers were used to prevent air exposure. The resulting suspensions were brown and opaque. Larger, unexfoliated sediments were removed by centrifugation for 1 h at 2000 *g*. The yellow-brown supernatants containing bP_{exf} were collected. An average calculated concentration of 1.67±0.75

mM was obtained from 15 different batches of bP_{exf} dispersions centrifuged at 2000 *g*. The concentration was estimated using previously reported extinction coefficients.[40]

For characterization by XPS and XES specifically, materials treated with $^{MeO}BzN_3$, AdN_3, and $^{CF3}BzN_3$ were centrifuged at 500 *g* to isolate a larger amount of product for characterization. This process yielded thicker exfoliated nanosheets.

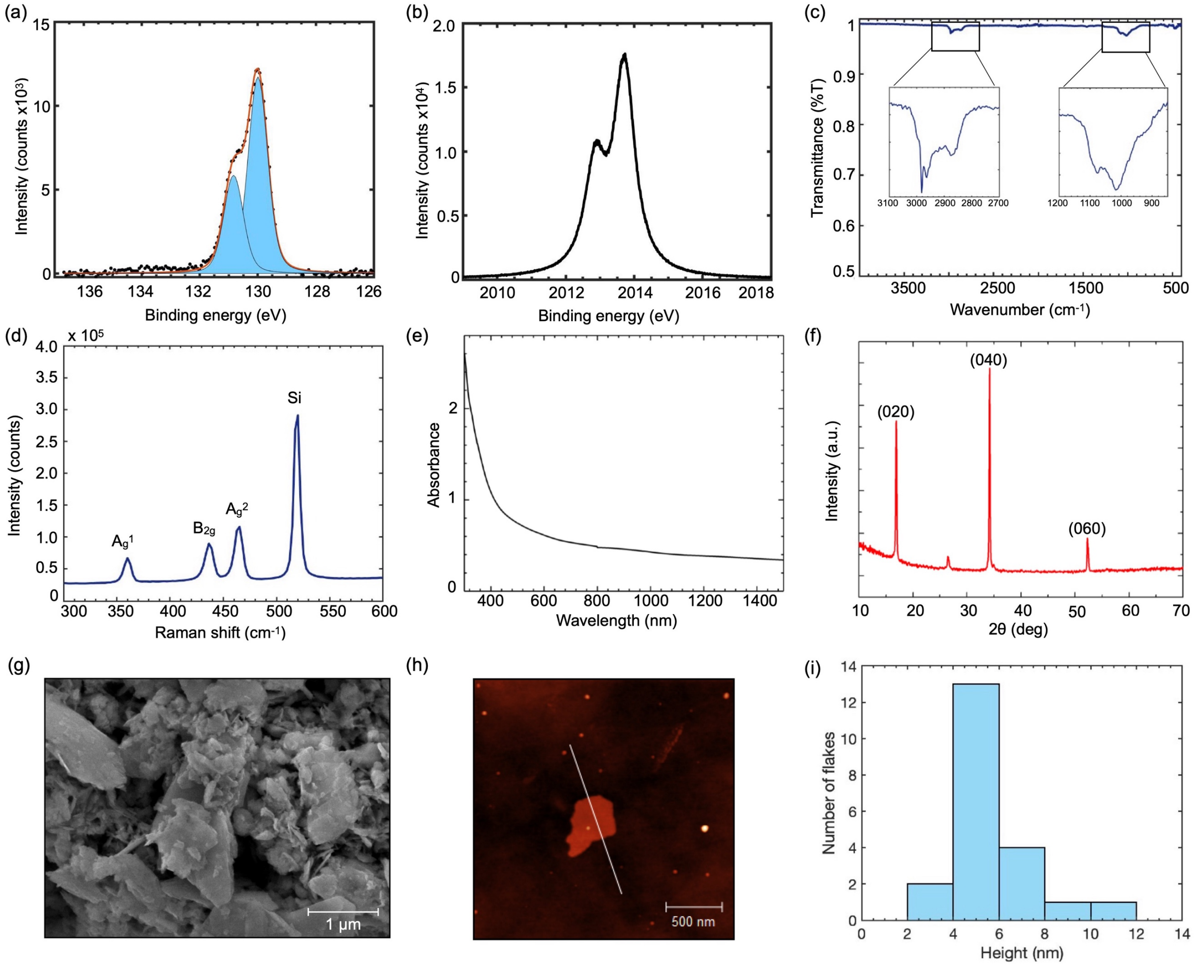

Figure 2.8. Characterization of bP_{exf}. (a) High-resolution P2p XPS of bP_{exf}. No phosphorus oxide formation is observed. (b) Phosphorus Kα XES spectrum for bP_{exf} showing no detectable oxidation. (c) ATR-IR spectrum of bP_{exf} showing minimal adsorbates. (d) Raman spectrum of bP_{exf}. (e) UV-visible-NIR absorption profile of a bP_{exf} dispersion in PhCN. The absorption shoulder at 450 nm was used to determine concentration in accordance with literature reports. (f) Powder-XRD of bP_{exf}. (g) SEM image of bP_{exf}. (h) AFM image of a drop-cast liquid-exfoliated bP_{exf} flake. (i) Histogram of the heights of solution-phase exfoliated flakes collected by centrifugation at 2000 g indicating an average thickness of 7–11 layers. Heights were determined by AFM.

2.5.5 *Functionalization of bP$_{exf}$ with organic azides under photolytic conditions*

All reactant stoichiometries were based on an approximative concentration of bP$_{exf}$ nanosheets in benzonitrile of 1.67 mM. Molar equivalencies were calculated relative to all dispersed phosphorus atoms (*i.e.* an excess of azide was used relative to the surface phosphorus atoms available for reactivity). During photolysis, reaction mixtures were stirred vigorously in Pyrex flasks, which were clamped at a distance of *ca.* 6 inches from the light source.

A bP$_{exf}$ dispersion in PhCN (30 mL, 1.67 mM at 2000 *g*, 1 equiv) and an organic azide (AdN$_3$, ^{CF_3}BzN$_3$, TsN$_3$, ^{MeO}BzN$_3$, Ts$^{14/15}$N$_3$ or ^{MeO}Bz$^{14/15}$N$_3$, respectively; 0.20 mmol, 4.0 equiv) were loaded into a 50-mL Schlenk tube equipped with a Teflon stir bar. Prior to photolysis, the headspace of the flask was evacuated to accommodate the N$_2$ evolved during the reaction. The reaction mixture was irradiated for 2 h under vigorous stirring and then filtered to isolate the solid products. The collected solids were washed on the filter membrane with PhCN (1 x 30 mL) and THF (1 x 30 mL) before being resuspended in THF (*ca*. 5 mL) for storage. This workup was effective at removing reaction byproducts and was used for all samples. A workup consisting of washing the collected solids with DCM (5 x 2 mL) was found to be ineffective at removing reaction byproducts from the nanosheets (Figure A.8).

Control sample: photolysis of bP$_{exf}$

A 50-mL Schlenk tube equipped with a Teflon stir bar was loaded with bP$_{exf}$ (30 mL, 1.67 mM at 2000 *g*, 1 equiv) in PhCN. The headspace of the tube was evacuated, and the reaction mixture was irradiated for 2 h under vigorous stirring. No color change was observed in the photo-treated solution. The collected solids were washed on the filter membrane with PhCN (1 x 30 mL) and THF (1 x 30 mL) before being resuspended in THF (*ca*. 5 mL) for storage.

Photolytic treatment of bP*exf* with organic azides for NMR analysis

Three 100-mL Schlenk tubes equipped with Teflon stir bars were loaded with bP*exf* in PhCN (50 mL, 1.67 mM at 2000 *g*, 1 equiv) and the organic azide (TsN_3, $Ts^{14/15}N_3$, $^{MeO}BzN_3$, or $^{MeO}Bz^{14/15}N_3$; 0.33 mmol, 4.0 equiv). Simultaneously, two 50-mL Schlenk tubes equipped with Teflon stir bars were loaded with bP*exf* in PhCN (30 mL, 1.67 mM at 2000 *g*, 1 equiv) and the organic azide (0.20 mmol, 4.0 equiv). All headspaces were evacuated. All tubes were irradiated for 2 h, after which the reaction mixtures were a wine-red color. To obtain the solid product, the reaction suspension was centrifuged at 15,000 *g* for 1 h at 4 °C. The pellet was resuspended in a minimal amount of PhCN (*ca.* 15 mL), filtered, and washed sequentially with PhCN (1 x 15 mL) and THF (1 x 15 mL). The resulting dark-brown filter cake was resuspended *via* ultrasonication in THF (*ca.* 7 mL) and centrifuged at 5,000 *g*. The solid product was placed under vacuum for 4 h prior to analysis.

Control sample: thermolysis of bP*exf*

A Schlenk flask equipped with a Teflon stir bar was loaded with a dispersion of bP*exf* in PhCN (30 mL, 1.67 mM at 2000 *g*, 1 equiv). The dispersion was vigorously stirred at 150 °C for 12 h. No color change or other visual indicators differentiated the resulting mixture from the original bP*exf* solution. The reaction mixture was filtered to isolate the solid product. The collected solids were washed on the filter membrane with PhCN (1 x 30 mL) and THF (1 x 30 mL) before the solids were resuspended in THF (*ca*. 5 mL) for storage.

2.6 ACKNOWLEDGEMENTS

Adapted with permission from Walz Mitra, K.L.; Chang, C.H.; Hanrahan, M.P.; Yang, J.; Tofan, D.; Holden, W.M.; Govind, N.; Seidler, G.T.; Rossini, A.J.; Velian, A. Surface Functionalization

of Black Phosphorus with Nitrenes: Identification of P=N Bonds by Using Isotopic Labeling. *Angew. Chem. Int. Ed.* **2021**, *60*, 9127. Copyright 2020 Wiley-VCH GmbH.

2.7 References

[1] L. Li, Y. Yu, G. J. Ye, Q. Ge, X. Ou, H. Wu, D. Feng, X. H. Chen, Y. Zhang, *Nature Nanotechnology* **2014**, *9*, 372–377.

[2] H. S. Ra, A. Y. Lee, D. H. Kwak, M. H. Jeong, J. S. Lee, *ACS Applied Materials and Interfaces* **2018**, *10*, 925–932.

[3] Q. Guo, A. Pospischil, M. Bhuiyan, H. Jiang, H. Tian, D. Farmer, B. Deng, C. Li, S. J. Han, H. Wang, Q. Xia, T. P. Ma, T. Mueller, F. Xia, *Nano Letters* **2016**, *16*, 4648–4655.

[4] H. Yuan, X. Liu, F. Afshinmanesh, W. Li, G. Xu, J. Sun, B. Lian, A. G. Curto, G. Ye, Y. Hikita, Z. Shen, S. C. Zhang, X. Chen, M. Brongersma, H. Y. Hwang, Y. Cui, *Nature Nanotechnology* **2015**, *10*, 707–713.

[5] Y. Saito, T. Iizuka, T. Koretsune, R. Arita, S. Shimizu, Y. Iwasa, *Nano Letters* **2016**, *16*, 4819–4824.

[6] H. Liu, A. T. Neal, Z. Zhu, Z. Luo, X. Xu, D. Tománek, P. D. Ye, *ACS Nano* **2014**, *8*, 4033–4041.

[7] M. Van Druenen, F. Davitt, T. Collins, C. Glynn, C. O'Dwyer, J. D. Holmes, G. Collins, *Chemistry of Materials* **2018**, *30*, 4667–4674.

[8] F. Hof, R. A. Schäfer, C. Weiss, F. Hauke, A. Hirsch, *Chemistry - A European Journal* **2014**, *20*, 16644–16651.

[9] C. R. Ryder, J. D. Wood, S. A. Wells, Y. Yang, D. Jariwala, T. J. Marks, G. C. Schatz, M. C. Hersam, *Nature Chemistry* **2016**, *8*, 597–602.

[10] J. M. Englert, C. Dotzer, G. Yang, M. Schmid, C. Papp, J. M. Gottfried, H. P. Steinrück, E. Spiecker, F. Hauke, A. Hirsch, *Nature Chemistry* **2011**, *3*, 279–286.

[11] K. C. Knirsch, N. C. Berner, H. C. Nerl, C. S. Cucinotta, Z. Gholamvand, N. McEvoy, Z. Wang, I. Abramovic, P. Vecera, M. Halik, S. Sanvito, G. S. Duesberg, V. Nicolosi, F. Hauke, A. Hirsch, J. N. Coleman, C. Backes, *ACS Nano* **2015**, *9*, 6018–6030.

[12] H. Staudinger, J. Meyer, *HCA* **1919**, *2*, 635–646.

[13] Y. Liu, P. Gao, T. Zhang, X. Zhu, M. Zhang, M. Chen, P. Du, G. W. Wang, H. Ji, J. Yang, S. Yang, *Angewandte Chemie - International Edition* **2019**, *58*, 1479–1483.

[14] H. Hu, H. Gao, L. Gao, F. Li, N. Xu, X. Long, Y. Hu, J. Jin, J. Ma, *Nanoscale* **2018**, *10*, 5834–5839.

[15] A. Reiser, H. M. Wagner, *The Chemistry of the Azido Group*, John Wiley & Sons Ltd., **1971**.

[16] G. L'abbé, *Chemical Reviews* **1969**, *69*, 345–363.

[17] Y. G. Gololobov, L. F. Kasukhin, *Tetrahedron* **1992**, *48*, 1353–1406.

[18] M. Taniguchi, S. Suga, M. Seki, H. Sakamoto, H. Kanzaki, Y. Akahama, S. Terada, S. Endo, S. Narita, *Solid State Communications* **1983**, *45*, 59–61.

[19] J. Brunner, M. Thuler, S. Veprekt, R. Wild, *J. Phys. Chem. Solids* **1979**, *40*, 967–971.

[20] F. Tao, Z. H. Wang, X. F. Chen, G. Q. Xu, *Phys. Rev. B* **2002**, *65*, 115311.

[21] C. Powell, **1989**, *X-ray Photoelectron Spectroscopy Database XPS,Version 4.1, NIST Standard Reference Database 20*, DOI 10.18434/T4T88K.

[22] T. Yang, B. Dong, J. Wang, Z. Zhang, J. Guan, K. Kuntz, S. C. Warren, D. Tománek, *Physical Review B - Condensed Matter and Materials Physics* **2015**, *92*, 1–6.

[23] K. L. Kuntz, R. A. Wells, J. Hu, T. Yang, B. Dong, H. Guo, A. H. Woomer, D. L. Druffel, A. Alabanza, D. Tománek, S. C. Warren, *ACS Applied Materials and Interfaces* **2017**, *9*, 9126–9135.

[24] W. M. Holden, Laboratory-Based Tender X-Ray Emission Spectroscopy: Instrumental, Experimental, and Theoretical Advances and Application to the Study of Phosphorus and Sulfur Electronic Structure, University of Washington, **2019**.

[25] S. Wild, M. Fickert, A. Mitrovic, V. Lloret, C. Neiss, J. A. Vidal-Moya, M. Á. Rivero-Crespo, A. Leyva-Pérez, K. Werbach, H. Peterlik, M. Grabau, H. Wittkämper, C. Papp, H. Steinrück, T. Pichler, A. Görling, F. Hauke, G. Abellán, A. Hirsch, *Angew. Chem. Int. Ed.* **2019**, *58*, 5763–5768.

[26] X. Zhu, T. Zhang, D. Jiang, H. Duan, Z. Sun, M. Zhang, H. Jin, R. Guan, Y. Liu, M. Chen, H. Ji, P. Du, W. Yan, S. Wei, Y. Lu, S. Yang, *Nature Communications* **2018**, *9*, 1–9.

[27] C. Ferrara, E. Vigo, B. Albini, P. Galinetto, C. Milanese, C. Tealdi, E. Quartarone, S. Passerini, P. Mustarelli, *ACS Applied Energy Materials* **2019**, *2*, 2794–2802.

[28] J. P. Yesinowski, in *Solid State NMR*, Springer-Verlag Berlin Heidelberg, Berlin, Heidelberg, **2012**, pp. 229–312.

[29] M. Tomaselli, J. L. Yarger, M. Bruchez, R. H. Havlin, D. deGraw, A. Pines, A. P. Alivisatos, *The Journal of Chemical Physics* **1999**, *110*, 8861–8864.

[30] D. Voiry, A. Goswami, R. Kappera, C. D. C. C. E. Silva, D. Kaplan, T. Fujita, M. Chen, T. Asefa, M. Chhowalla, *Nature Chemistry* **2015**, *7*, 45–49.

[31] F. Himo, Z. P. Demko, L. Noodleman, K. B. Sharpless, *Journal of the American Chemical Society* **2002**, *124*, 12210–12216.

[32] S. C. S. Bugalho, A. C. Serra, L. Lapinski, M. L. S. Cristiano, R. Fausto, *Physical Chemistry Chemical Physics* **2002**, *4*, 1725–1731.

[33] T. Sainsbury, A. Satti, P. May, A. O'Neill, V. Nicolosi, Y. K. Gun'Ko, J. N. Coleman, *Chemistry - A European Journal* **2012**, *18*, 10808–10812.

[34] K. S. Maiti, *Physical Chemistry Chemical Physics* **2015**, *17*, 19735–19744.

[35] L. C. Thomas, *Interpretation of the Infrared Spectra of Organophosphorus Compounds*, Heyden, London, New York, **1974**.

[36] W. Wiegräbe, H. Bock, *Chemische Berichte* **1968**, *101*, 1414–1427.

[37] T. Meguro, S. Yoshida, K. Igawa, K. Tomooka, T. Hosoya, *Organic Letters* **2018**, *20*, 4126–4130.

[38] Y. Zhao, H. Wang, H. Huang, Q. Xiao, Y. Xu, Z. Guo, H. Xie, J. Shao, Z. Sun, W. Han, X. F. Yu, P. Li, P. K. Chu, *Angewandte Chemie - International Edition* **2016**, *55*, 5003–5007.

[39] S. Y. Pyun, Y. H. Lee, T. R. Kim, *Kinetics and Catalysis* **2005**, *46*, 21–28.

[40] A. H. Woomer, T. W. Farnsworth, J. Hu, R. A. Wells, C. L. Donley, S. C. Warren, *ACS Nano* **2015**, *9*, 8869–8884.

[41] H. Lu, V. Subbarayan, J. Tao, X. P. Zhang, *Organometallics* **2010**, *29*, 389–393.

[42] S. C. Hockey, G. J. Barbante, P. S. Francis, J. M. Altimari, P. Yoganantharajah, Y. Gibert, L. C. Henderson, *European Journal of Medicinal Chemistry* **2016**, *109*, 305–313.

[43] B. Zhu, H. Zhang, S. Pan, C. Wang, J. Ge, J.-S. Lee, S. Q. Yao, *Chem. Eur. J.* **2016**, *22*, 7824–7836.

[44] W. M. Holden, O. R. Hoidn, A. S. Ditter, G. T. Seidler, J. Kas, J. L. Stein, B. M. Cossairt, S. A. Kozimor, J. Guo, Y. Ye, M. A. Marcus, S. Fakra, *Review of Scientific Instruments* **2017**, *88*, 073904.

[45] J. L. Stein, W. M. Holden, A. Venkatesh, M. E. Mundy, A. J. Rossini, G. T. Seidler, B. M. Cossairt, *Chem. Mater.* **2018**, *30*, 6377–6388.

[46] W. M. Holden, O. R. Hoidn, G. T. Seidler, A. D. DiChiara, *Review of Scientific Instruments* **2018**, *89*, 093111.

[47] M. Newville, T. Stensitzki, D. B. Allen, A. Ingargiola, **2014**, DOI 10.5281/ZENODO.11813.

[48] J. F. Moulder, W. F. Stickle, P. E. Sobol, K. D. Bomben, J. Chastain, R. C. King Jr., Physical Electronics, Incorporation, Eds. , *Handbook of X-Ray Photoelectron Spectroscopy: A Reference Book of Standard Spectra for Identification and Interpretation of XPS Data*, Physical Electronics, Eden Prairie, Minn., **1995**.

[49] R. K. Harris, E. D. Becker, S. M. Cabral de Menezes, R. Goodfellow, P. Granger, *Pure and Applied Chemistry* **2001**, *73*, 1795–1818.

[50] M. Feike, D. E. Demco, R. Graf, J. Gottwald, S. Hafner, H. W. Spiess, *Journal of Magnetic Resonance, Series A* **1996**, *122*, 214–221.

[51] I. Schnell, A. Lupulescu, S. Hafner, D. E. Demco, H. W. Spiess, *Journal of Magnetic Resonance* **1998**, *133*, 61–69.

[52] I. Schnell, *Progress in Nuclear Magnetic Resonance Spectroscopy* **2004**, *45*, 145–207.

[53] B. M. Fung, A. K. Khitrin, K. Ermolaev, *Journal of Magnetic Resonance* **2000**, *142*, 97–101.

[54] A. Pines, M. G. Gibby, J. S. Waugh, *The Journal of Chemical Physics* **1973**, *59*, 569–590.

[55] N. M. Szeverenyi, M. J. Sullivan, G. E. Maciel, *Journal of Magnetic Resonance (1969)* **1982**, *47*, 462–475.

[56] Yoshitaka Ishii, Robert Tycko, *Journal of Magnetic Resonance* **n.d.**, *142*, 199–204.

[57] T. Slagbrand, A. Volkov, P. Trillo, F. Tinnis, H. Adolfsson, *ACS Catal.* **2017**, *7*, 1771–1775.

3 SURFACE FUNCTIONALIZATION OF BLACK PHOSPHORUS WITH DISCRETE ORGANOMETALLIC FRAGMENTS

3.1 INTRODUCTION

Black phosphorus (bP), a 2D allotrope of elemental phosphorus, is a promising material for electronic,[1,2] optical,[3,4] and thermoelectric[5] applications due to its tunable near IR-to-visible direct bandgap, high on/off ratio, and high carrier mobility.[6] Surface modification has been shown to be a facile and effective method to tune these properties: treatment with group 13 Lewis acids[7] and TCNQ,[8,9] among others, has been shown to p-dope bP while treatment with benzyl viologen[10] results in n-doping, demonstrating strong electronic communication between surface moieties and bP. These interactions can also be harnessed to enhance catalytic performance: nanoparticles adsorbed on bP show enhanced activity for ORR[11] and hydrogenation,[12,13] among other reactions. Interactions with surface groups likely occur through the surface lone pairs which are available for reactivity as exemplified by the rapid oxidation of bP under ambient conditions.[14]

Covalent functionalization of bP has largely been explored with organic groups including aryl,[15–18] alkyl,[19–22] and amine groups.[23,24] In contrast, there is little work with discrete organometallic fragments; the existing literature primarily focuses on studying function (e.g., ambient stability, drug delivery) rather than probing the nature of the M–bP interaction.[25–28] Understanding the role that bP plays in an organometallic complex not only would expand the library of functional groups available for bP modification but could also shed light on how bP behaves as ligand, allowing for more informed design of bP-containing systems.

This type of investigation is precedented for other 2D materials such as transition metal dichalcogenides, graphitic carbon nitride, and gray arsenic where covalent functionalization with metal carbonyls[29–31] and acetate fragments,[32] among others, has been demonstrated. Discrete covalent bonding between these nanosheets and the organometallic fragments is established in large part by taking advantage of the spectroscopic handles on the ancillary ligands via IR spectroscopy.[29–32] While theoretical work by Ienco and coworkers suggests that bP can form dative bonds with Lewis acidic organometallic fragments,[33] to our knowledge, this has yet to be conclusively established experimentally.

Herein, the covalent functionalization of bP with discrete organometallic Re and Mo complexes is demonstrated. Specifically, $Re(CO)_5Cl$ (**1**$(CO)_2(Cl)$), $CpRe(CO)_3$ (**2**(CO)), $Re(bipy)(CO)_3Cl$ (**3**(Cl)), and $CpMo(CO)_3(BF_4)$ (**4**) were used to functionalize bP under mild synthetic conditions inspired by molecular phosphine reactions (Figure 3.1). The structure of the resulting materials was probed in detail using X-ray (XPS, XRD) and spectroscopic techniques (DRIFTS, Raman). The dominant M–bP binding mode of each organometallic functional group was identified using DRIFTS spectroscopy coupled with group theory, revealing that bP is capable of binding discrete

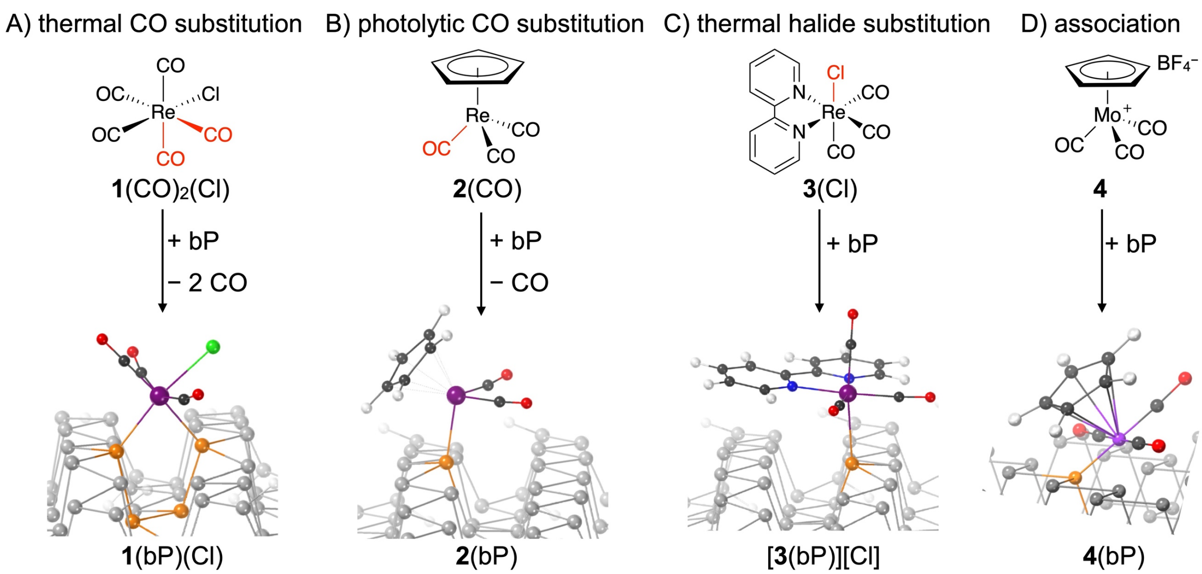

Figure 3.1. Functionalization of bP with parent metal precursors via (A) thermal CO substitution, (B) photolytic CO substitution, (C) thermal halide substitution, and (D) association. (D) is not optimized.

organometallic complexes analogous to molecular phosphines. Reactions of bP with **1**$(CO)_2Cl$ demonstrate the chelating ability of bP as a ligand for the first time experimentally. The stoichiometric chemistry of the functionalized nanosheets was further probed via anion exchange and ligand insertion. New vibrational modes post-reaction demonstrate successful modification of the Re center, indicating that once immobilized, the organometallic fragments are still available for traditional organometallic manipulation.

3.2 Results and Discussion

3.2.1 *Synthesis*

Fresh dispersions of bP_{exf} were treated with four molecular complexes $Re(CO)_5Cl$ (**1**$(CO)_2(Cl)$), $CpRe(CO)_3$ (**2**(CO)), $Re(bipy)(CO)_3Cl$ (**3**(Cl)), or $[CpMo(CO)_3][BF_4]$ (**4**), respectively (Figure 3.1).[34–37] Post-functionalization, no discrete crystalline species except black phosphorus are observed via Raman spectroscopy or PXRD (Figure B.1). Spectroscopic signatures of the organic ligands are observable by IR spectroscopy and XPS, indicating the organometallic fragments remain intact. The resulting bP nanosheets feature spectroscopic signatures indicating M–bP bond formation, ostensibly via three distinct pathways depending on the nature of the parent complex: CO or halide substitution, and ligand association.

3.2.2 *Infrared Spectroscopy*

Previous work in our group has demonstrated the utility of IR spectroscopy in interrogating the nature of functional groups on bP,[24] and as a result, IR was the primary characterization tool in this work. Carbonyl ligands are well-established spectroscopic reporters in molecular systems and their utility in probing the structure of functionalized inorganic surfaces has been previously demonstrated for many materials including for 2D materials,[29,32,38–40] metal oxides,[41–43] nanocrystals,[44],[45] and zeolites.[46,47] Here, DRIFTS spectroscopy in conjunction with symmetry considerations and comparison to molecular analogues indicate a single dominant product is formed in each of the Re-functionalized nanosheets and at least two in the more reactive Mo precursor case.

IR spectroscopy indicates the consumption of the starting materials and the formation of discrete metal complexes anchored on the bP surface (Figure 3.2). The product formed upon treating bP with **1**(CO)$_2$(Cl) has a vibrational spectrum diagnostic of a κ^2–bound Re tricarbonyl species, with three CO stretches red-shifted from the parent complex. The number, energy, and intensity of these CO stretches are remarkably reminiscent of the molecular complex *fac*-**1**(PPh$_3$)$_2$(Cl) (Figure 3.2).[48],[49] The formation of bP–Re(CO)$_3$Cl sites demonstrates the purported chelating ability of the bP surface to function as a bidentate ligand.[33] To our knowledge, this is the first experimental evidence of a κ^2–bP structure.

Functionalization of bP with **2**(CO) gives rise to a single product with two red-shifted CO stretches that closely resembles those of the molecular complex **2**(PPh$_3$), signaling the formation of κ^1 bP–CpRe(CO)$_2$ sites (Figure 3.2). In contrast to the two CO substitution reactions, the reaction between **3**(Cl) and bP results in an overall blue-shift of the CO vibrations, reminiscent of the cationic *facial* tricarbonyl complex [**3**(PPh$_3$)][Cl] (Figure 3.2).[50] Although this reaction occurs under identical conditions to that of bP and **1**(CO)$_2$(Cl), Cl^- substitution is observed instead of CO likely due to the increased stabilization of Re^+ afforded by bipy. In addition to the similarity with [**3**(PPh$_3$)][Cl], vibrational modes observed at 1611 and 1560 cm^{-1} indicate preservation of the bipy

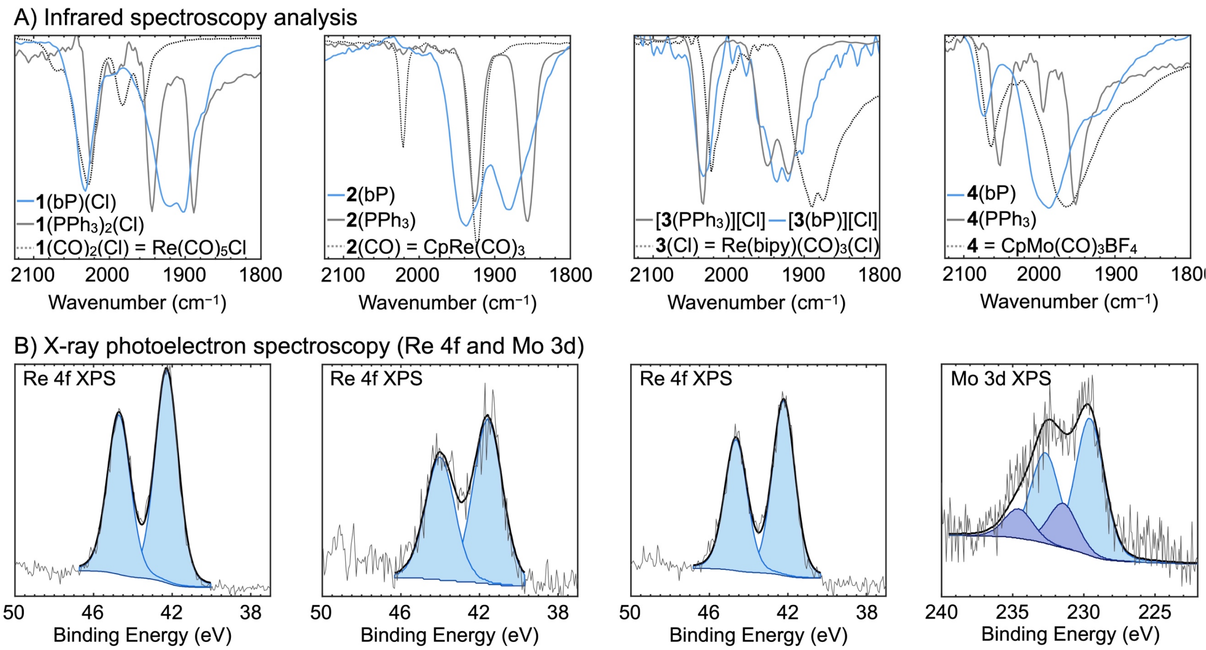

Figure 3.2. Spectroscopic characterization of functionalized materials. (A) DRIFTS of **1**$(CO)_2$Cl, **2**(CO), [**3**(bP)]Cl, and **4**(bP) overlaid with the respective parent complexes and the PPh_3 molecular analogs. (B) High-resolution XPS of **1**$(CO)_2$Cl, **2**(CO), [**3**(bP)]Cl, and **4**(bP).

ligand (Figure B.5). Efforts to substitute carbonyl ligands from [**3**(PPh_3)][Cl] through thermolytic or photolytic methods were unsuccessful.

The nucleophilic 16 e^- complex **4** salt,[51,52] is significantly more reactive towards bP with the reaction proceeding at room temperature. The vibrational spectrum of the functionalized nanosheets **4**(bP) features strong CO stretches slightly blue-shifted from the parent complex (by 4 and 9 cm^{-1}; Figure 3.2). Unlike the other tricarbonyl materials, the two asymmetric stretches in **4**(bP) were unable to be resolved. The prominent shoulder at 1926 cm^{-1} is likely indicative of a secondary binding mode, possibly decarbonylated $CpMo(CO)_2(bP)(BF_4)$ sites with bP again acting as a bidentate, κ^2 chelating ligand.[53–55]

3.2.3 *X-ray Photoelectron Spectroscopy*

To corroborate the IR data, a host of other characterization techniques were employed, including XPS, PXRD, and Raman spectroscopy. Of these, XPS was most informative, confirming the incorporation of the metal complexes in the functionalized nanosheets (Figure 3.2). The presence of Re, C (carbonyl), and Cl was detected in **1**(bP), whereas Mo, C (carbonyl), and F were found in **4**(bP). No distinct P 2p binding environment associated with P–M bonding is detected in any of the functionalized samples by XPS. However, this is expected considering the lack of oxidation state changes at P upon coordination.[56] Notably, XPS also reveals that no adventitious oxidation of the bP lattice occurred during the functionalization protocols.[14,57,58] High-resolution Re 4f peak fitting reveals only one Re environment per material at energies consistent with those reported for other immobilized rhenium(I) carbonyl complexes[59–61] and molecular rhenium(I) carbonyl phosphine complexes.[62–64] Notably, no Re^0 nanoparticles[65] or Re oxides[56] were detected by XPS or PXRD. High-resolution Mo 3d and F 1s XPS reveal two Mo and F environments, each in approximately a 1:3 ratio, consistent with the formation of two products upon treatment of bP with **4** (Figure B.4). Considering the relative binding energies of the two species and the associated IR data, we propose the major product is the five-coordinate Mo(II) complex **4**(bP), whereas the minor components, shifted to higher energies, could be associated with the less-electron rich Mo(II) center in bP–$CpMo(CO)_2(BF_4)$.[66]

3.2.4 *Degree of bP Functionalization*

Characterization of the nanosheets by bulk ICP-MS measurements as well as surface techniques (XPS) allowed for an estimate of the metal loading on bP. ICP of **1**(bP)(Cl) indicates a bulk 0.17 ±0.02 mol% Re loading (1 Re / 97 P atoms). This is significantly smaller than other reports of bP functionalization for both organic groups (from *ca.* 1.3% for isobutyronitrile[20] to 7% for CH_3[22])

and other metal species like Al^{3+} (9%)[67] and Pd–Pd (3.3–6.1%)[68] using bulk techniques. This lower loading could be due to the relative thickness of the nanosheets or to the larger steric bulk of the $Re(CO)_3Cl$ groups.

All observable Re is localized to the bP surface. PXRD and Raman spectroscopy showed no evidence of intercalation (Figure B.1); however, a recent report of bP intercalated with dimeric Pd–Pd units reveals that these techniques alone are not sufficient to rule out intercalation.[68] However, in contrast with this report, the ligands around Re are preserved, ostensibly ruling out intercalation without noticible lattice disruption due to the large van der Waals radius of the organometallic fragments. Additionally, XPS spectra of the Re-functionalized materials clearly reveal only Re(I) species and show no Re(0) formation that could signal intercalation (Figure 3.2).

Interestingly, the available surface binding sites appear to be saturated after the first functionalization, even if the apparent degree of functionalization is low. Attempts to further functionalize **1**(bP)(Cl) and **2**(bP) using the electrophilic **4** were unsuccessful, even though these materials show the lowest degrees of functionalization (Figure B.6).

To estimate the Re surface loading, XPS was performed. XPS of **1**(bP)(Cl) over 7 measurements gives an average of *ca.* 2% Re surface loading (1 Re / 59 P). However, these measurements sampled only a small number of nanosheets; additional techniques that survey multiple flakes are needed. While the other functionalized materials were not examined by ICP, XPS suggests that the identity of the functional group affects the degree of functionalization. **2**(bP) is the least functionalized (1 Re/101 P) followed by **1**(bP)(Cl) (1/59), [**3**(bP)][Cl] (1/34), and **4**(bP) (1/25). While all values except for **1**(bP)(Cl) represent only two measurements, this trend may be related to the electrophilicity of the unsaturated 16 e^- organometallic intermediates (see Appendix I.B.3 for more discussion).[33]

3.2.5 *Black phosphorus as a Ligand: Estimating Tolman Parameters*

As a ligand, bP appears to behave similarly to a molecular phosphine: reaction conditions for molecular phosphine complexes can be adapted for successful bP functionalization and subsequent modification at the metal center. While some studies have touched on bP as a potential ligand for single metal atoms,[13,69] to our knowledge there has been no direct comparison of its electronic and steric character with other molecular phosphines. However, this is an important step in understanding and predicting the chemistry it can engage in. Using Tolman's electronic parameter (TEP) and buried volume calculations, the electronic and steric character of bP was directly compared to other phosphines.

TEP[70], based on carbonyl stretching frequencies, is a widely used method for understanding the reactivity of phosphines. Originally applied to $Ni(CO)_3L$, L = PR_3, $P(OR)_3$ complexes, it has since been extended to study a host of metal carbonyl complexes, including $[Re(bipy)(CO)_3(PR_3)]^+$,[71] as well as other non-phosphine L-type ligands.[72,73] While this method has limitations,[72] for

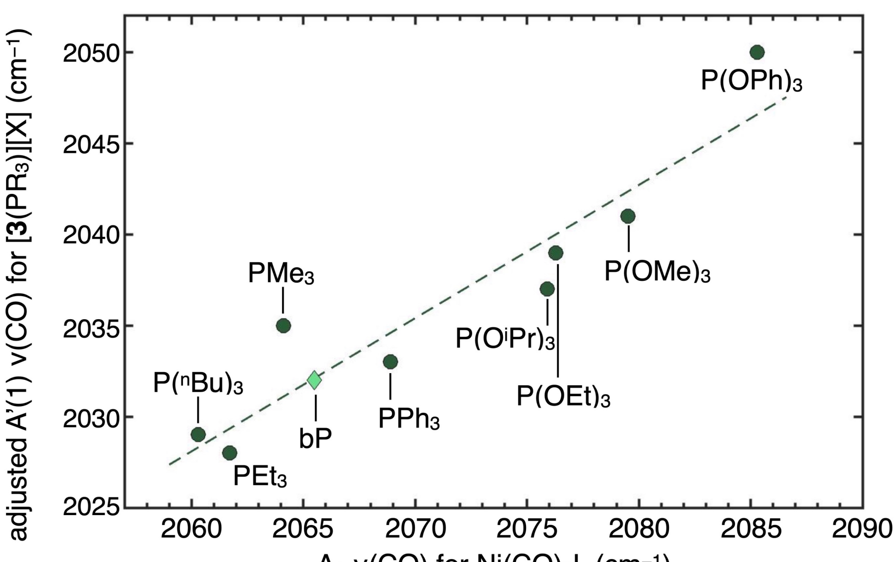

Figure 3.3. Plot of symmetric ν(CO) for [**3**(PR_3)][X] versus Tolman's Ni complex showing linear correlation (R^2 = 0.881). bP is plotted based on [**3**(bP)][Cl] A'(1) ν(CO).

example a dependence on measurement parameters and packing effects, we found $[Re(bipy)(CO)_3(PR_3)]^+$ to be an effective qualitative probe for bP electronic character as the reference data set agreed most closely with our $[Re(bipy)(CO)_3(PPh_3)]Cl$ reference compound (see Appendix I.B.2 for more details). Comparison of bP with both phosphines and phosphites suggests that it is a strong σ-donor with minimal π-accepting character akin to PEt_3 (Figure 3.3). While both theoretical[33,74,75] and experimental studies[7,13,76,77] suggest bP can act chemically as a Lewis base, our results are in contrast to *in silico* studies which predict bP to be a worse Lewis base than molecular phosphines due to a degree of electron delocalization.[33,75]

The steric bulk of bP in these materials was also assessed for κ^1 and κ^2 binding modes for [**3**(bP)][Cl] and **1**(bP)(Cl), respectively, using the percent buried volume ($\%V_{bur}$) (Table B.5; see Appendix B.2 for details on calculation).[78,79] While as a surface bP has inherent steric rigidity, this analysis shows that it is not significantly bulkier than common phosphine ligands. In the κ^1 binding mode, $\%V_{bur} = 28\%$, not much larger than the 25% calculated for P(*p*-tol)$_3$ analog (Tolman $\theta = 145°$).[70] In the κ^2 binding mode, $\%V_{bur}$ increases to 43% making bP sterically similar to bidentate phosphines like bis(diphenylphosphino)propane (dppp, $\%V_{bur} = 44\%$, Tolman $\theta = 127°$), but still smaller than PPh_3 ($\%V_{bur} = 45\%$, Tolman $\theta = 145°$).[70] This relative lack of steric strain may come from its unique corrugated structure which could allow metals more space along the channel side.

3.2.6 *Ligand Exchange*

As analysis of ν(CO) indicates that bP is both sterically and electronically similar to alkyl phosphines, a series of ligand exchange reactions was conducted to probe whether the

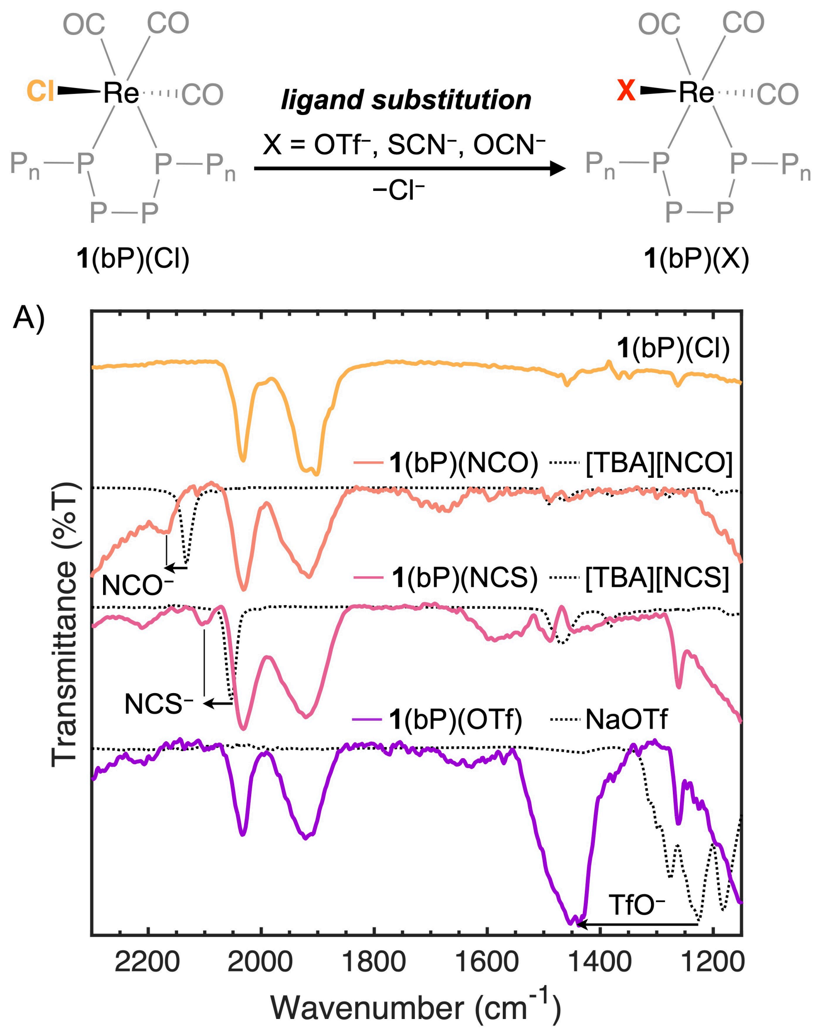

Figure 3.4. Anion exchange reactions of **1**(bP)(Cl). (A) DRIFTS spectra of **1**(bP)(X), X= Cl^-, OTf^-, OCN^-, and SCN^-.

functionalized nanosheet was chemically comparable to molecular analogs. Initial reactions focused on straightforward anion exchanges of **1**(bP)(Cl) demonstrate that the immobilized Re centers are accessible to substrates.

Anion exchanges of **1**(bP)(Cl) using ligands with strong spectroscopic signals (OTf^-, OCN^-, SCN^-) allowed for clear tracking of reaction success (Figure 3.4). Upon treatment of **1**(bP)(Cl) with the parent salts, distinct blue-shifts of the key spectroscopic stretches are observed, indicating coordination to the Re center and formation of **1**(bP)(OTf), **1**(bP)(NCO), and **1**(bP)(NCS), respectively.[80–82] For **1**(bP)(NCS), the observed ν(CO)/ν(CN) intensity ratio is also comparable with those reported for diimine[83] and phosphine[84] molecular analogs.

The observed spectroscopic features do not come from residual parent salts or from adsorption to the bP surface: no spectroscopic signatures of the parent salts are observed via IR while PXRD shows no crystalline salt domains (Figure B.7). Additional control reactions with NaOTf and TBA(NCS) show no new spectroscopic signatures that would indicate adsorption (Figure B.10). Throughout all three reactions, Re–P bonding was preserved: no leaching or dissociation from the nanosheet was detected by IR (Figure B.8) or by ICP-MS (0.17 mol% Re in both **1**(bP)(Cl) and **1**(bP)(OTf)).

3.2.7 *Sequential Anion Exchange and Ligand Insertion*

To further probe the stoichiometric reactivity of **1**(bP)(X), the synthesis of the methyl carbonate species **1**(bP)(CO_3CH_3) was approached via two pathways: sequential anion exchange followed by CO_2 insertion (Path 1,[85] Figure 3.5) or via direct anion exchange using cesium carbonate followed by methylation (Path 2, Figure 3.5).[86,87]

Path 1, an analogue of work performed by Simpson and Bergman with **1**(PMe_3)(X), demonstrates that **1**(bP)(X) behaves similar to molecular phosphine analogues.[85,88] In Path 1, **1**(bP)(OTf) was formed from **1**(bP)(Cl) and then treated with $NaOCH_3$ to give **1**(bP)(OCH_3). Again, IR played a key role in tracking this exchange: upon formation of **1**(bP)(OCH_3), the strong 1470 cm^{-1} feature

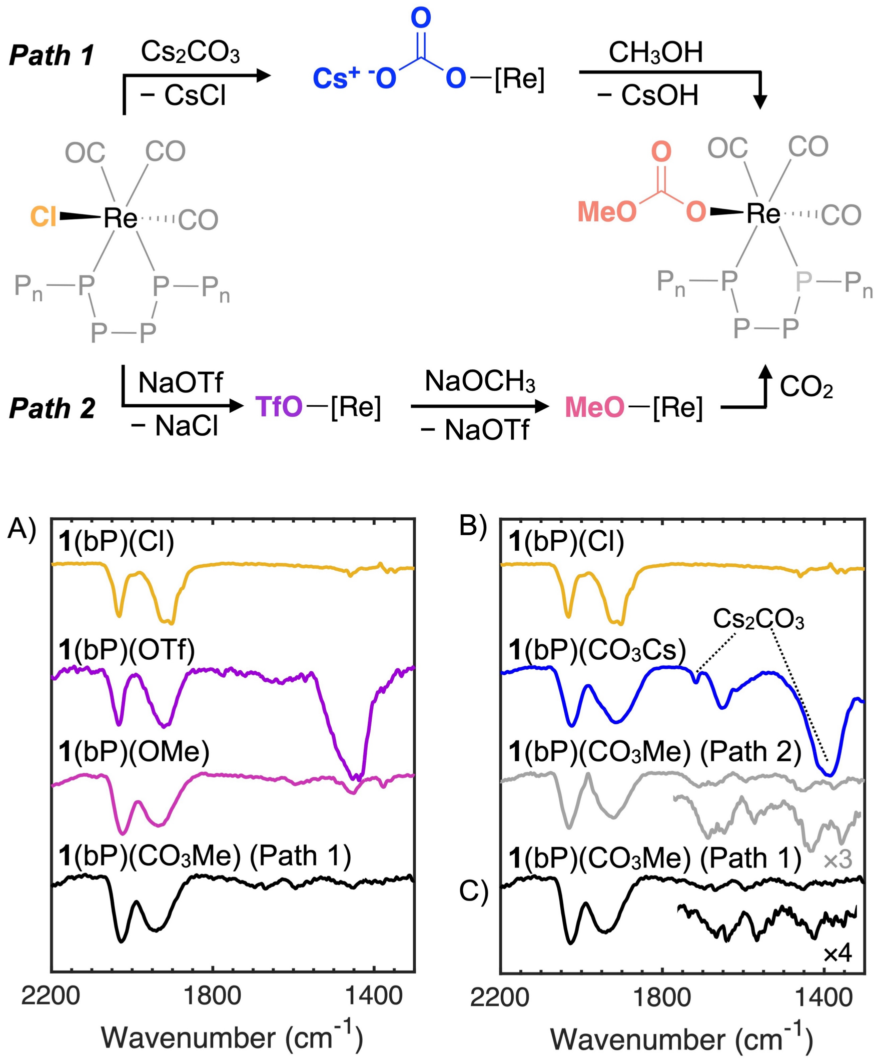

Figure 3.5. Synthesis of **1**(bP)(CO_3CH_3). DRIFTS of (A) Path 1 materials, (B) Path 2 materials, and (C) **1**(bP)(CO_3CH_3) synthesized via Path 1.

characteristic of coordinated OTf^- is replaced by three new features associated with OCH_3^-. While the exact assignment of these features is ambiguous (Figure B.11),[89] they were only observed when OCH_3^- was present. Introduction of CO_2 into a dispersion of **1**(bP)(OCH_3) gave **1**(bP)(CO_3CH_3), as evinced by the appearance of a new IR feature at 1671 cm^{-1}, likely associated with C=O.[85,90,91]

To support successful synthesis of **1**(bP)(CO_3CH_3), the methyl carbonate was independently synthesized through Path 2.[86,87] Combining **1**(bP)(Cl) and Cs_2CO_3 gave **1**(bP)(CO_3Cs) with a new spectroscopic feature at 1650 cm^{-1} corresponding to a terminal carbonate anion.[92] While molecular analogs of this exchange usually result in dimers bridged by CO_3^{2-}, the frequency of the observed stretch is more blue-shifted than expected for a bridging carbonate.[93,94] Unlike the other anion exchanges, residual parent Cs_2CO_3 salt was still observed in **1**(bP)(CO_3Cs); efforts to completely remove it were unsuccessful (see Section 3.4.7 for details). Treating **1**(bP)(CO_3Cs) with methanol gave **1**(bP)(CO_3CH_3) with identical spectroscopic features to the product from Path 1, indicating that the methyl carbonate can be successfully synthesized via two complimentary pathways.

3.3 Conclusion

This study reveals that Lewis acidic organometallic fragments are competent reaction partners for bP functionalization. Infrared spectroscopy coupled with symmetry considerations and molecular analogs reveal one dominant binding mode on each Re-functionalized material including the first experimental evidence of a κ^2 binding mode. Using Tolman's electronic parameter as a model with IR, bP was found to be a good σ-donor with little π-accepting character. Post-functionalization stoichiometric reactivity studies with **1**(bP)(X) show (1) the Re centers are accessible to substrates after functionalizing the bP surface, (2) the Re—P bonds are chemically robust and can withstand sequential transformations at the metal center, and (3) the stoichiometric chemistry of the Re centers on bP is analogous to the chemistry of molecular Re phosphine complexes.

3.4 EXPERIMENTAL

3.4.1 *Materials*

Unless stated otherwise, all work was performed under an inert atmosphere of N_2 using a Schlenk line or inside of an LC Technology Solutions, Inc. glove box containing <5 ppm H_2O and O_2. All glassware was dried at 160˚C for a minimum of 12 h and cooled under vacuum prior to use. All solvents excluding benzonitrile were purchased from Fischer Scientific. Anhydrous solvents were dispensed from a JC Meyer solvent system and stored over 3 Å molecular sieves (Thermo-Fisher) for at least 12 h before use. Molecular sieves were previously activated under vacuum at 300˚C for 48 h. Benzonitrile (99%, Alfa Aesar) was degassed for at least 6 hours under vacuum and stored over activated 3Å molecular sieves in the glovebox for a minimum of 72 h prior to use.

Black phosphorus (bP) crystals were synthesized using the methods in Reference [95]. $Re(CO)_5Cl$ (98%, Strem Chemicals), $CpRe(CO)_3$ (99%, Strem Chemicals), $[CpMo(CO)_3]_2$ (98%, Strem Chemicals), 2,2'-bipyridine (≥99%, Sigma Aldrich), NaOTf (98%, Sigma Aldrich), TBA(NCS) (98%, Sigma Aldrich), NaNCS (≥98%, Sigma Aldrich), TBA(NCO) (technical, Sigma Aldrich), PPh_3 (≥99%, Sigma Aldrich), $AgBF_4$ (98%, Sigma Aldrich), AgOTf (≥99%, Sigma Aldrich), and Cs_2CO_3 (99%, Sigma Aldrich) were used as received. $Re(bipy)(CO)_3Cl$ and (η^5-C_5H_5)$Mo(CO)_3(BF_4)$ were synthesized according to procedures reported in the literature;[96,97] see Section 3.4.5. CO_2 was purchased from Praxair and passed through a column of activated charcoal and Drierite before introduction into any reaction.

Ultrasonication was performed in a 110W bath sonicator at 40 kHz. Circulation cooling was used to maintain a bath temperature of 22-28˚C. Filtrations were performed with EMD Millipore Omnipore hydrophobic membrane filters with a pore size of 0.2 μm. Photolytic treatments were performed with a 450 W medium-pressure mercury vapor lamp (Hanovia Specialty Lighting, PC 451.050) emitting 200–400 nm broadband radiation. The lamp was hosted inside a quartz jacket that was continuously cooled to maintain the reactions at ambient temperature.

3.4.2 *Instrumentation*

Attenuated total reflectance infrared (ATR-IR) spectra were recorded on a Bruker Alpha IR instrument equipped with a Platinum ATR accessory. Diffuse reflectance infrared Fourier transform spectroscopy (DRIFTS) was used in some analyses with the corresponding Bruker DRIFTS accessory and FTIR-grade potassium bromide (KBr, >99%; Alfa Aesar). Raman spectra were acquired on a Renishaw InVia microscope using a 532 nm diode-pumped solid-state laser and a 50x microscope objective. XRD spectra were acquired on a Bruker D8 Discover powder X-ray diffractometer with a large-area Pilatus 100K large-area 2D detector under ambient conditions. XPS/ESCA analysis was performed on a Surface Science Instruments (SSI) S-Probe system under ultrahigh vacuum with a monochromatized Al Kα X-ray source and a low energy electron flood gun for charge neutralization. For spectroscopic analysis (XPS, Powder-XRD, and Raman), test-grade Si wafers (University Wafer) and Au-coated Si wafers (100 nm Au, Platypus Technologies) were cut, rigorously washed by sequential ultrasonication with detergent (Si only), water (Si only), acetone, and isopropanol, and then oven-dried overnight at 150 °C prior to use. Suspensions of various bP products in tetrahydrofuran (THF) were drop-cast onto clean silicon wafers and annealed for 2–5 min at 80 °C before analysis. XPS analyses were conducted using identical preparations with clean Au-coated Si wafers. Wafers for Raman spectroscopy were sealed between two glass slides with a ring of silicone grease. Kapton tape was used to cover wafers for XRD.

Analysis of the XPS spectra was performed using Esca Hawk7 software. Binding energies were referenced to adventitious carbon (B.E.[C 1s] = 285.0 eV) and Shirley baselines were used. Fitting of multiple peak shapes was restricted to the least number of peaks required to adequately fit the spectrum. Paired pseudo-Voigt profiles were used to fit the (P $2p_{3/2}$, P $2p_{1/2}$), (Re $4f_{7/2}$, Re $4f_{5/2}$), and (Mo $3d_{5/2}$, Mo $3d_{3/2}$) doubles. To fit multiple peak shapes, widths of subsequent signals were constrained to the width of the respective doublet pairs. Relative contributions of each unique peak shape were measured according to the relative intensity of the signal. P2p doublets were fit to data using a Shirley baseline with a fixed peak separation of 0.84 eV and relative ratio of 2:1, consistent with reported values for phosphorus.[98] Re 4f doublets were fit to data using a Shirley baseline with a fixed peak separation of 2.43 eV and a relative ratio of 4:3.[99] Mo 3d doublets were fit to data using a Shirley baseline with a fixed peak separation of 3.13 eV and a relative ratio of 3:2.[99]

Raman spectra were referenced to the Si wafer peak at 522.1 cm^{-1}. As the A_g^1 Raman mode represents the out-of-plane Raman mode,[100] comparison of the A_g^1 intensities provides the most information. Because Raman intensity depends on multiple factors, including nanosheet orientation,[101] a minimum of 4 Raman measurements per sample were collected. Assuming a random distribution of orientations, each peak intensity was averaged for comparison between samples. Even with averaging, the multiple factors influencing the Raman intensity resulted in a large error in the A_g^1 intensities, and this parameter cannot be used alone as an indicator of the degree of functionalization.

To increase the signal-to-noise ratio, all black phosphorus-containing products were analyzed with diffuse reflectance infrared Fourier transform spectroscopy (DRIFTS). This technique is less surface sensitive than ATR-FTIR,[102] however, spectra collected with ATR-FTIR showed extremely poor signal-to-noise ratios. Due to the additional bulk modes in DRIFTS, broad $\nu(CO)_{asym}$ are observed in almost all samples rather than the expected sharp $\nu(CO)_{asym}$.

3.4.3 *Liquid exfoliation of bP*

Crystals of black phosphorus (bulk bP; 60 mg) were finely crushed with an agate mortar and pestle. The resulting fine, silver-black powder was subsequently sonicated in the dark for 20 h in anhydrous benzonitrile (120 mL). Air-free 250-mL Schlenk flasks sealed with Teflon stoppers were used to prevent air exposure. The resulting suspensions were brown and opaque. The solids were isolated via filtration and washed extensively with tetrahydrofuran to remove residual benzonitrile. The solids were then resuspended in THF using sonication.

3.4.4 *Functionalization of bP*

The subsequent reactions were adapted from analogous reactions with molecular phosphines.[37,103–105] All reactant stoichiometries were based on an approximated concentration of bP_{exf} nanosheets in the respective solvents. Molar equivalencies were calculated relative to the total dispersed phosphorus atoms; relative to the number of surface atoms available for functionalization, an excess of metal complex was used. During both thermolysis and photolysis, the reaction mixtures were stirred vigorously. During photolysis, reaction mixtures were contained in Pyrex flasks, which were clamped at *ca.* 6 inches from the light source.

Synthesis of 1(bP)(Cl) and [3(bP)][Cl]

To a Schlenk flask equipped with a Teflon stir bar, a dispersion of bP_{exf} (60 mg, 1 equiv.) in 15 mL THF and either $Re(CO)_5Cl$ (180.9 mg, 0.50 mmol, 0.26 equiv.) or $Re(bipy)(CO)_3Cl$ (116.50 mg, 0.25 mmol, 0.26 equiv.) were added. The reaction mixture was refluxed under N_2 for 24 h at 70˚C. The solids were isolated by vacuum filtration using a 0.2 μm hydrophobic PTFE membrane. To remove unreacted metal complex and physisorbed species, the solids were washed with pentane (1x10 mL) and THF (2x20 mL). The solids were resuspended in *ca.* 10 mL of THF via sonication, isolated via centrifugation at 5000*g*, and dried under vacuum. The products are referred to as **1**(bP)(Cl) and [**3**(bP)][Cl] throughout.

Synthesis of 2(bP)

To a Schlenk tube equipped with a Teflon stir bar, a dispersion of bP_{exf} (20 mg, 1 equiv.) in 15 mL THF and $CpRe(CO)_3$ (197.1 mg, 0.59 mmol, 0.91 equiv.) were added. The headspace was evacuated, and the reaction mixture was irradiated for 5 h with vigorous stirring. The solids were isolated by vacuum filtration. To remove unreacted metal complex and physisorbed species, the solids were washed with THF (1x15 mL) and pentane (2x20 mL). The product was resuspended in *ca.* 10 mL of THF via sonication, isolated via centrifugation at 5000*g*, and dried under vacuum. The product is referred to as **2**(bP) throughout.

Synthesis of 4(bP)

A solution of $CpMo(CO)_3(BF_4)$ (55.7 mg, 0.17 mmol, 0.26 equiv.) in 10 mL of DCM was added to a dispersion of bP_{exf} (20 mg, 0.65 mmol, 1 equiv.) in 10 mL of DCM. The reaction mixture was transferred to a Schlenk flask equipped with a Teflon stir bar and stopcock, and stirred overnight at room temperature. The solids were isolated by vacuum filtration and washed with DCM (1x40 mL) and THF (1x15 mL) to remove unreacted metal complex and physisorbed species. The solids were resuspended in *ca.* 10 mL of THF by sonication, centrifuged at 5000*g*, and dried under vacuum. The product is referred to as **4**(bP) throughout.

3.4.5 *Synthesis of PPh_3 analogs*

Synthesis of 1(PPh_3)(Cl)

The synthesis was adapted from Reference [34]. Briefly, $Re(CO)_5Cl$ (100.0 mg, 0.28 mmol) was combined with a solution of PPh_3 (183.6 mg, 0.70 mmol) in 10 mL of toluene and transferred to a

100 mL Schlenk flask equipped with a Teflon stopcock and stir bar. The reaction mixture was refluxed for 2.5 h, after which the solvent was removed under vacuum. The resulting oil was triturated with 5 mL of MeOH and then recrystallized from DCM and MeOH. ν(CO) (solid) = 2025, 1944, 1889 cm^{-1}.

Synthesis of 2(PPh_3)

The procedure was followed from Reference [105]. $CpRe(CO)_3$ (100.0 mg, 0.30 mmol) was combined with a solution of PPh_3 (82.0 mg, 0.31 mmol) in 15 mL of THF and transferred to a 50 mL Schlenk tube equipped with a Teflon stopcock and stir bar. The headspace of the tube was evacuated, and the solution was photolyzed for 4.5 h. After photolysis, the headspace was again evacuated to remove CO that evolved during the reaction. The solution volume was then reduced under vacuum to give a light yellow powder. The solid was dissolved in DCM and passed through a column of alternating Celite and silica layers. The product was eluted with DCM; the volume of the eluted solution was reduced to *ca.* 1 mL. To this solution, 25 mL of pentane was added. The solution was then passed through a silica column, first eluting with pentane followed by a 3:1 pentane:DCM solution. The pentane:DMC fraction was collected and found to contain both the product and $CpRe(CO)_3$. The volume was again reduced to *ca.* 1 mL, 25 mL of pentane was added, and it was passed through a silica column. The column was eluted first with pentane until IR showed no CO stretches present in the fraction. The column was then eluted with a 1:1 pentane:DCM solution. This fraction was collected; by IR, the resulting product was pure $CpRe(CO)_2(PPh_3)$. ν(CO) (DCM/pentane) = 1925, 1856 cm^{-1}.

Synthesis of [3(PPh_3)][OTf]

The procedure was obtained from Reference [106] and [107]. $Re(CO)_5Cl$ (500.0 mg, 1.38 mmol) was dissolved in hot toluene. 2,2'-bipyridine (bipy; 215.5 mg, 1.38 mmol) was added to this solution. The reaction mixture was refluxed for 1 h, allowed to cool to room temperature, and cooled to −35°C overnight. The product was then filtered to isolate yellow crystals. $Re(bipy)(CO)_3Cl$ ν(CO) (MeCN) = 2023, 1917, 1899 cm^{-1}.

$Re(bipy)(CO)_3Cl$ (75.0 mg, 0.16 mmol) was then combined with a solution of AgOTf (41.1 mg, 0.16 mmol) in 15 mL of THF in a 100 mL Schlenk flask equipped with a Teflon stopcock and stir bar. The solution was refluxed for 2 h. The byproduct, AgCl, was removed via filtration through a Celite plug to give a solution of $Re(bipy)(CO)_3(OTf)$ in THF. PPh_3 (335.7 mg, 1.28 mmol) was added to this solution. The reaction mixture was then refluxed overnight and the solvent removed under vacuum to give $[Re(bipy)(CO)_3(PPh_3)][OTf]$. ν(CO) (solid) = 2033, 1948, 1921 cm^{-1}.

Synthesis of 4(PPh_3)

The procedure was adapted from Reference [97] and [54]. $AgBF_4$ (1.6 g, 8.2 mmol) was added to a solution of $[CpMo(CO)_3]_2$ (2.0 g, 4.1 mmol) in 100 mL of dry DCM in a 200 mL pear-shaped flask. The reaction mixture was stirred for 5 h at room temperature. After 5 h, the volume of the mixture was reduced and the mixture was filtered to remove precipitated Ag. 100 mL of pentane was added and the solution was cooled to −35°C overnight. The mixture was then filtered. Post-filtration, purple crystals began to crash out of the filtrate. An additional 100 mL of pentane was layered over the filtrate and the solution cooled to −35°C overnight. The mixture was then filtered to isolate $CpMo(CO)_3(BF_4)$. ν(CO) (DCM) = 2068, 1960 cm^{-1}.

PPh_3 (78.7 mg, 0.30 mmol) was added to a solution of $CpMo(CO)_3(BF_4)$ (100 mg, 0.30 mmol) in 5 mL of DCM. The mixture was stirred at room temperature for 30 minutes. The solution was added to a 100-10 mL mixture of ether-pentane and cooled to −35°C overnight. A yellow powder was isolated by filtration and washed with ether. ν(CO) (solid) = 2052, 1995, 1951 cm^{-1}.

3.4.6 *Anion exchange of **1**(bP)(Cl)*

Treatment of 1(bP)(Cl) with NaOTf

A solution of NaOTf (16.7 mg, 0.10 mmol, 0.3 equiv.) in 5 mL of THF was added to a dispersion of **1**(bP)(Cl) (10 mg, 0.32 mmol, 1 equiv.) in 10 mL of THF in a 40 mL amber vial equipped with a Teflon-lined cap and stir bar. The reaction mixture was stirred for 18 h. The solids were isolated by vacuum filtration and washed with THF (1x40 mL) to remove NaCl and unreacted NaOTf. The solids were resuspended in *ca.* 10 mL of THF by sonication, centrifuged at 5000*g*, and dried under vacuum. The product is referred to as **1**(bP)(OTf) throughout.

Treatment of 1(bP)(Cl) with Na(NCS) and TBA(NCS)

The product **1**(bP)(NCS) was obtained through three different sets of reaction conditions detailed below. All three methods gave a material with the same characteristic spectroscopic features.

Method 1: A solution of tetrabutylammonium thiocyanate (TBA(NCS); 18.0 mg, 0.06 mmol) in 5 mL of THF was added to a dispersion of **1**(bP)(Cl) (10 mg, 0.32 mmol) in 15 mL of THF in a 40 mL amber vial equipped with a Teflon-lined cap and a stir bar. The reaction mixture was stirred for 18 h in the dark. The nanosheets were isolated by vacuum filtration and washed with THF (1x40 mL). The solids were resuspended in *ca.* 10 mL of THF via sonication, centrifuged at 5000*g*, and dried under vacuum.

Method 2: A solution of sodium thiocyanate (Na(NCS); 23.6 mg, 0.29 mmol) in 5 mL of THF was added to a dispersion of **1**(bP)(Cl) (30 mg, 0.97 mmol) in 15 mL of THF in a 40 mL amber vial equipped with a Teflon-lined cap and a stir bar. The reaction mixture was stirred for 18 h in the dark. The nanosheets were isolated by vacuum filtration and washed with THF (1x40 mL). The solids were resuspended in *ca.* 10 mL of THF via sonication, centrifuged at 5000*g*, and dried under vacuum.

Method 3: A solution of sodium thiocyanate (Na(NCS); 8.1 mg, 0.10 mmol) in 5 mL of THF was added to a dispersion of **1**(bP)(Cl) (10 mg, 0.32 mmol) in 15 mL of THF in a 100 mL Schlenk flask equipped with a stir bar. The reaction mixture was heated to 40 °C and stirred for 18 h in the dark. The nanosheets were isolated by vacuum filtration and washed with THF (1x40 mL). The solids were resuspended in *ca.* 10 mL of THF via sonication, centrifuged at 5000*g*, and dried under vacuum.

Treatment of 1(bP)(Cl) with TBA(NCO)

A solution of tetrabutylammonium cyanate (TBA(NCO); 17.1 mg, 0.06 mmol) in 5 mL of THF was added to a dispersion of **1**(bP)(Cl) (10 mg, 0.32 mmol) in 10 mL of THF in a 40 mL amber vial equipped with a Teflon-lined cap and a stir bar. The reaction mixture was stirred for 18 h in the dark. The nanosheets were isolated by vacuum filtration and washed with THF (1x40 mL). The solids were resuspended in *ca.* 10 mL of THF via sonication, centrifuged at 5000*g*, and dried under vacuum. The product is referred to as **1**(bP)(NCO) throughout.

3.4.7 *Stoichiometric reactivity of **1**(bP)X*

Treatment of 1(bP)(OTf) with $NaOCH_3$ and $NaOCD_3$

A solution of sodium methoxide ($NaOCH_3$; 0.74 mmol, 0.66 eq.) in 10 mL of methanol was added to a dispersion of **1**(bP)(OTf) (1.13 mmol, 1 eq.) in 15 mL of THF in a 40 mL amber vial equipped with a Teflon-lined cap and a stir bar. The reaction mixture was stirred for 18 h in the dark. The nanosheets were isolated by vacuum filtration and washed with MeOH (1x20 mL) and THF (1x20 mL). The solids were resuspended in *ca.* 10 mL of THF via sonication, centrifuged at 5000*g*, and dried under vacuum. The product is referred to as **1**(bP)(OCH_3) throughout.

Isotopically labeled **1**(bP)(OCD_3) was prepared in the same manner except: (1) $NaOCD_3$ was prepared directly from sodium metal and CD_3OD and (2) 0.3 eq. of $NaOCD_3$ was used.

CO_2 insertion into 1(bP)(OCH_3)

CO_2 was sparged into a dispersion of **1**(bP)(OCH_3) in THF for 3 h in a 100 mL Schlenk flask while stirring. The nanosheets were isolated by vacuum filtration and washed with THF (1x30 mL). The solids were resuspended in *ca.* 10 mL of THF via sonication, centrifuged at 5000*g*, and dried under vacuum. The product is referred to as **1**(bP)(CO_3CH_3) throughout.

Treatment of 1(bP)(Cl) with Cs_2CO_3

A solution of cesium carbonate (Cs_2CO_3; 15 mg, 0.05 mmol) in 10 mL of THF was added to a dispersion of **1**(bP)(Cl) (20 mg, 0.65 mmol) in 10 mL of THF in a 40 mL amber vial equipped with a Teflon-lined cap and a stir bar. The reaction mixture was stirred for 18 h in the dark. The nanosheets were isolated by vacuum filtration and washed with THF (1x40 mL). The solids were then stirred in THF/NMP while heating before isolating via vacuum filtration. This workup method gave the best, although not complete, removal of Cs_2CO_3. Other solvents including MeCN and DMF did not remove Cs_2CO_3. The solids were resuspended in *ca.* 10 mL of THF via sonication, centrifuged at 5000*g*, and dried under vacuum. The product is referred to as **1**(bP)(CO_3Cs) throughout.

Treatment of 1(bP)(CO_3Cs) with MeOH

10 mL of MeOH was added to a dispersion of **1**(bP)(CO_3Cs) in 15 mL of THF and stirred for 3 h. The nanosheets were isolated by vacuum filtration and washed with MeOH (1x30 mL) and THF

(1x20 mL). The solids were then resuspended in *ca.* 10 mL of THF via sonication, centrifuged at 5000*g*, and dried under vacuum. The product is referred to as **1**(bP)(CO_3CH_3) throughout.

3.5 References

[1] H. Liu, Y. Du, Y. Deng, P. D. Ye, *Chem. Soc. Rev.* **2015**, *44*, 2732–2743.

[2] L. Li, Y. Yu, G. J. Ye, Q. Ge, X. Ou, H. Wu, D. Feng, X. H. Chen, Y. Zhang, *Nature Nanotech* **2014**, *9*, 372–377.

[3] J. Miao, L. Zhang, C. Wang, *2D Mater.* **2019**, *6*, 032003.

[4] X. Chen, J. S. Ponraj, D. Fan, H. Zhang, *Nanoscale* **2020**, *12*, 3513–3534.

[5] Y. Zhang, Y. Zheng, K. Rui, H. H. Hng, K. Hippalgaonkar, J. Xu, W. Sun, J. Zhu, Q. Yan, W. Huang, *Small* **2017**, *13*, 1700661.

[6] H. Liu, A. T. Neal, Z. Zhu, Z. Luo, X. Xu, D. Tománek, P. D. Ye, *ACS Nano* **2014**, *8*, 4033–4041.

[7] D. Tofan, Y. Sakazaki, K. L. Walz Mitra, R. Peng, S. Lee, M. Li, A. Velian, *Angew. Chem. Int. Ed.* **2021**, anie.202100308.

[8] G. Abellán, V. Lloret, U. Mundloch, M. Marcia, C. Neiss, A. Görling, M. Varela, F. Hauke, A. Hirsch, *Angew. Chem. Int. Ed.* **2016**, *55*, 14557–14562.

[9] Y. Du, L. Yang, H. Zhou, P. D. Ye, *IEEE Electron Device Lett.* **2016**, *37*, 429–432.

[10] D. Yue, D. Lee, Y. D. Jang, M. S. Choi, H. J. Nam, D.-Y. Jung, W. J. Yoo, *Nanoscale* **2016**, *8*, 12773–12779.

[11] Y. Peng, B. Lu, N. Wang, J. E. Lu, C. Li, Y. Ping, S. Chen, *ACS Appl. Mater. Interfaces* **2019**, *11*, 24707–24714.

[12] M. Caporali, M. Serrano-Ruiz, F. Telesio, S. Heun, G. Nicotra, C. Spinella, M. Peruzzini, *Chemical Communications* **2017**, *53*, 10946–10949.

[13] M. Vanni, M. Serrano-Ruiz, F. Telesio, S. Heun, M. Banchelli, P. Matteini, A. M. Mio, G. Nicotra, C. Spinella, S. Caporali, A. Giaccherini, F. D’Acapito, M. Caporali, M. Peruzzini, *Chem. Mater.* **2019**, *31*, 5075–5080.

[14] K. L. Kuntz, R. A. Wells, J. Hu, T. Yang, B. Dong, H. Guo, A. H. Woomer, D. L. Druffel, A. Alabanza, D. Tománek, S. C. Warren, *ACS Applied Materials and Interfaces* **2017**, *9*, 9126–9135.

[15] M. van Druenen, F. Davitt, T. Collins, C. Glynn, C. O'Dwyer, J. D. Holmes, G. Collins, *Chem. Mater.* **2018**, *30*, 4667–4674.

[16] Y. Cao, X. Tian, J. Gu, B. Liu, B. Zhang, S. Song, F. Fan, Y. Chen, *Angew. Chem. Int. Ed.* **2018**, *57*, 4543–4548.

[17] W. Chen, S. Gao, Z. Xie, Y. Lu, G. Gong, G. Liu, J. Shang, C. Yao, R.-W. Li, *J. Mater. Chem. C* **2020**, *8*, 7309–7313.

[18] S. Thurakkal, X. Zhang, *Mater. Chem. Front.* **2021**, *5*, 2824–2831.

[19] Z. Sofer, J. Luxa, D. Bouša, D. Sedmidubský, P. Lazar, T. Hartman, H. Hardtdegen, M. Pumera, *Angew. Chem. Int. Ed.* **2017**, *56*, 9891–9896.

[20] H. Hu, H. Gao, L. Gao, F. Li, N. Xu, X. Long, Y. Hu, J. Jin, J. Ma, *Nanoscale* **2018**, *10*, 5834–5839.

[21] S. Wild, X. T. Dinh, H. Maid, F. Hauke, G. Abellán, A. Hirsch, *Angew. Chem. Int. Ed.* **2020**, *59*, 20230–20234.

[22] S. Wild, M. Fickert, A. Mitrovic, V. Lloret, C. Neiss, J. A. Vidal-Moya, M. Á. Rivero-Crespo, A. Leyva-Pérez, K. Werbach, H. Peterlik, M. Grabau, H. Wittkämper, C. Papp, H. Steinrück, T. Pichler, A. Görling, F. Hauke, G. Abellán, A. Hirsch, *Angew. Chem. Int. Ed.* **2019**, *58*, 5763–5768.

[23] Y. Liu, P. Gao, T. Zhang, X. Zhu, M. Zhang, M. Chen, P. Du, G. Wang, H. Ji, J. Yang, S. Yang, *Angew. Chem. Int. Ed.* **2019**, *58*, 1479–1483.

[24] K. L. Walz Mitra, C. H. Chang, M. P. Hanrahan, J. Yang, D. Tofan, W. M. Holden, N. Govind, G. T. Seidler, A. J. Rossini, A. Velian, *Angew. Chem. Int. Ed.* **2021**, *60*, 9127–9134.

[25] L. Wu, J. Wang, J. Lu, D. Liu, N. Yang, H. Huang, P. K. Chu, X.-F. Yu, *Small* **2018**, *14*, 1801405.

[26] Y. Zhao, H. Wang, H. Huang, Q. Xiao, Y. Xu, Z. Guo, H. Xie, J. Shao, Z. Sun, W. Han, X.-F. Yu, P. Li, P. K. Chu, *Angew. Chem. Int. Ed.* **2016**, *55*, 5003–5007.

[27] J. Zhang, Y. Ma, K. Hu, Y. Feng, S. Chen, X. Yang, J. Fong-Chuen Loo, H. Zhang, F. Yin, Z. Li, *Bioconjugate Chem.* **2019**, *30*, 1658–1664.

[28] X. Jiang, H. Jin, R. Gui, *Dalton Trans.* **2020**, *49*, 11911–11920.

[29] B. Coulson, M. Isaacs, L. Lari, R. E. Douthwaite, A.-K. Duhme-Klair, *Chem. Commun.* **2019**, *55*, 7450–7453.

[30] J. D. Dillenburger, M. A. T. Nguyen, P. Xu, J. R. Shallenberger, T. E. Mallouk, *Inorg. Chem.* **2022**, *61*, 14824–14832.

[31] J. Sturala, Z. Sofer, M. Pumera, *NPG Asia Mater* **2019**, *11*, 42.

[32] C. Backes, N. C. Berner, X. Chen, P. Lafargue, P. LaPlace, M. Freeley, G. S. Duesberg, J. N. Coleman, A. R. McDonald, *Angew. Chem. Int. Ed.* **2015**, *54*, 2638–2642.

[33] A. Ienco, G. Manca, M. Peruzzini, C. Mealli, C. Organometallici, C. Nazionale, *Dalton Transactions* **2018**, *47*, 17243–17256.

[34] G. Albertin, S. Antoniutti, J. Castro, S. García-Fontán, G. Zanardo, *Organometallics* **2007**, *26*, 2918–2930.

[35] K. Koike, J. Tanabe, S. Toyama, H. Tsubaki, K. Sakamoto, J. R. Westwell, F. P. A. Johnson, H. Hori, H. Saitoh, O. Ishitani, *Inorganic Chemistry* **2000**, *39*, 2777–2783.

[36] R. J. Angelici, G. Facchin, M. M. Singh, *Synthesis and Reactivity in Inorganic and Metal-Organic Chemistry* **1990**, *20*, 275–282.

[37] A. Velian, M. Nava, M. Temprado, Y. Zhou, R. W. Field, C. C. Cummins, *J. Am. Chem. Soc.* **2014**, *136*, 13586–13589.

[38] R. Kuriki, K. Sekizawa, O. Ishitani, K. Maeda, *Angew. Chem. Int. Ed.* **2015**, *54*, 2406–2409.

[39] B. Coulson, L. Lari, M. Isaacs, D. J. Raines, R. E. Douthwaite, A. Duhme-Klair, *Chem. Eur. J.* **2020**, *26*, 6862–6868.

[40] S. Lei, X. Wang, B. Li, J. Kang, Y. He, A. George, L. Ge, Y. Gong, P. Dong, Z. Jin, G. Brunetto, W. Chen, Z.-T. Lin, R. Baines, D. S. Galvão, J. Lou, E. Barrera, K. Banerjee, R. Vajtai, P. Ajayan, *Nature Nanotech* **2016**, *11*, 465–471.

[41] P. S. Kirlin, F. A. DeThomas, J. W. Bailey, H. S. Gold, C. Dybowski, B. C. Gates, *J. Phys. Chem.* **1986**, *90*, 4882–4887.

[42] C. J. Papile, B. C. Gates, *Langmuir* **1992**, *8*, 74–79.

[43] S. Khabuanchalad, J. Wittayakun, R. J. Lobo-Lapidus, S. Stoll, R. D. Britt, B. C. Gates, *Langmuir* **2013**, *29*, 6279–6286.

[44] K. A. Schival, R. R. Gipson, K. V. Prather, E. Y. Tsui, *Nano Lett.* **2019**, *19*, 7770–7774.

[45] K. V. Prather, S. Lee, E. Y. Tsui, *Inorg. Chem.* **2021**, acs.inorgchem.0c03641.

[46] H. Miessner, I. Burkhardt, D. Gutschick, A. Zecchina, C. Morterra, G. Spoto, *J. Chem. Soc., Faraday Trans. 1* **1989**, *85*, 2113.

[47] A. S. Hoffman, C.-Y. Fang, B. C. Gates, *J. Phys. Chem. Lett.* **2016**, *7*, 3854–3860.

[48] A. M. Bond, R. Colton, M. E. McDonald, *Inorg. Chem.* **1978**, *17*, 2842–2847.

[49] E. D. Olmon, Investigating DNA-Mediated Charge Transport by Time-Resolved Spectroscopy, California Institute of Technology, **2012**.

[50] S. Sato, T. Morimoto, O. Ishitani, *Inorg. Chem.* **2007**, *46*, 9051–9053.

[51] W. Beck, in *Inorganic Syntheses: Reagents for Transition Metal Complex and Organometallic Syntheses*, John Wiley & Sons, Inc, New York, **2007**, pp. 5–15.

[52] W. Beck, K. Suenkel, *Chem. Rev.* **1988**, *88*, 1405–1421.

[53] D. H. Gibson, K. Owens, T. S. Ong, *J. Am. Chem. Soc.* **1984**, *106*, 1125–1127.

[54] J. Markham, K. Menard, A. Cutler, *Inorg. Chem.* **1985**, *24*, 1581–1587.

[55] K. Sünkel, H. Ernst, W. Beck, *Zeitschrift für Naturforschung B* **1981**, *36*, 474–481.

[56] **2012**.

[57] M. T. Edmonds, A. Tadich, A. Carvalho, A. Ziletti, K. M. O'Donnell, S. P. Koenig, D. F. Coker, B. Özyilmaz, A. H. C. Neto, M. S. Fuhrer, *ACS Applied Materials and Interfaces* **2015**, *7*, 14557–14562.

[58] T. Yang, B. Dong, J. Wang, Z. Zhang, J. Guan, K. Kuntz, S. C. Warren, D. Tománek, *Physical Review B - Condensed Matter and Materials Physics* **2015**, *92*, 1–6.

[59] J. Willkomm, E. Bertin, M. Atwa, J.-B. Lin, V. Birss, W. E. Piers, *ACS Appl. Energy Mater.* **2019**, *2*, 2414–2418.

[60] A. Zhanaidarova, S. C. Jones, E. Despagnet-Ayoub, B. R. Pimentel, C. P. Kubiak, *J. Am. Chem. Soc.* **2019**, *141*, 17270–17277.

[61] D. A. Popov, J. M. Luna, N. M. Orchanian, R. Haiges, C. A. Downes, S. C. Marinescu, *Dalton Trans.* **2018**, *47*, 17450–17460.

[62] H. Hori, K. Koike, M. Ishizuka, K. Takeuchi, T. Ibusuki, O. Ishitani, *Journal of Organometallic Chemistry* **1997**, *530*, 169–176.

[63] E. M. Johnson, R. Haiges, S. C. Marinescu, *ACS Appl. Mater. Interfaces* **2018**, *10*, 37919–37927.

[64] V. I. Nefedov, *Soviet Journal of Coordination Chemistry* **1978**, *4*, 965.

[65] C. J. Powell, *Journal of Electron Spectroscopy and Related Phenomena* **2012**, *185*, 1–3.

[66] Samuel O. Grim, L. Matienzo J., *Inorganic Chemistry* **1975**, *14*, 1014–1018.

[67] X. Liu, L. Xiao, J. Weng, Q. Xu, W. Li, C. Zhao, J. Xu, Y. Zhao, *Sci. Adv.* **2020**, *6*, eabb4359.

[68] M. Vanni, M. Bellini, S. Borsacchi, L. Calucci, M. Caporali, S. Caporali, F. d'Acapito, M. Geppi, A. Giaccherini, A. Ienco, G. Manca, A. M. Mio, G. Nicotra, W. Oberhauser, M. Serrano-Ruiz, M. Banchelli, F. Vizza, M. Peruzzini, *J. Am. Chem. Soc.* **2021**, jacs.1c01754.

[69] X. Wang, L. Bai, J. Lu, X. Zhang, D. Liu, H. Yang, J. Wang, P. K. Chu, S. Ramakrishna, X. Yu, *Angewandte Chemie* **2019**, *131*, 19236–19242.

[70] C. A. Tolman, *Chem. Rev.* **1977**, *77*, 313–348.

[71] H. Tsubaki, S. Tohyama, K. Koike, H. Saitoh, O. Ishitani, *Dalton Trans.* **2005**, 385–395.

[72] O. Kuhl, *Coordination Chemistry Reviews* **2005**, *249*, 693–704.

[73] D. R. Anton, R. H. Crabtree, *Organometallics* **1983**, *2*, 621–627.

[74] W. Lei, T. Zhang, P. Liu, J. A. Rodriguez, G. Liu, M. Liu, *ACS Catal.* **2016**, *6*, 8009–8020.

[75] C. Mealli, A. Ienco, M. Peruzzini, G. Manca, *Dalton Trans.* **2018**, *47*, 394–408.

[76] J. Hu, Z. Guo, P. E. Mcwilliams, J. E. Darges, D. L. Druffel, A. M. Moran, S. C. Warren, *Nano Lett.* **2016**, *16*, 74–79.

[77] C. Chen, W. Ou, K. Yam, S. Xi, X. Zhao, S. Chen, J. Li, P. Lyu, L. Ma, Y. Du, W. Yu, H. Fang, C. Yao, X. Hai, H. Xu, M. J. Koh, S. J. Pennycook, J. Lu, M. Lin, C. Su, C. Zhang, J. Lu, *Adv. Mater.* **2021**, *33*, 2008471.

[78] L. Falivene, Z. Cao, A. Petta, L. Serra, A. Poater, R. Oliva, V. Scarano, L. Cavallo, *Nat. Chem.* **2019**, *11*, 872–879.

[79] J. Jover, J. Cirera, *Dalton Trans.* **2019**, *48*, 15036–15048.

[80] R. A. Bailey, S. L. Kozak, T. W. Michelsen, W. N. Mills, *Coordination Chemistry Reviews* **1971**, *6*, 407–445.

[81] L. Dahlenburg, G. Hillmann, M. Ernst, M. Moll, F. Knoch, *Journal of Organometallic Chemistry* **1996**, *525*, 115–123.

[82] G. A. Lawrance, *Chem. Rev.* **1986**, *86*, 17–33.

[83] Q. Liu, Y. Zhang, Q. Zhang, Q. Wei, D. Zhou, G. Wu, K. Cai, K. Yuan, H. Bian, *Phys. Chem. Chem. Phys.* **2019**, *21*, 23026–23035.

[84] N. W. Hoffman, N. Prokopuk, M. J. Robbins, C. M. Jones, N. M. Doherty, *Inorg. Chem.* **1991**, *30*, 4177–4181.

[85] R. D. Simpson, R. G. Bergman, *Organometallics* **1992**, *11*, 4306–4315.

[86] W.-G. Jia, Y.-F. Han, G.-X. Jin, *Organometallics* **2008**, *27*, 6035–6038.

[87] B. Demerseman, M. D. Mbaye, D. Sémeril, L. Toupet, C. Bruneau, P. H. Dixneuf, *Eur. J. Inorg. Chem.* **2006**, *2006*, 1174–1181.

[88] R. D. Simpson, R. G. Bergman, *Organometallics* **1993**, *12*, 781–796.

[89] G. Socrates, *Infrared Characteristic Group Frequencies*, Wiley, Chichester ; New York, **1980**.

[90] S. K. Mandal, D. M. Ho, M. Orchin, *Organometallics* **1993**, *12*, 1714–1719.

[91] K. Johnson, T. Frazier, T. M. Becker, K. Miller, D. M. Ho, J. Krause-Bauer, S. K. Mandal, *Inorganic Chemistry Communications* **2001**, *4*, 602–605.

[92] J. P. Jolivet, Y. Thomas, B. Taravel, V. Lorenzelli, *Journal of Molecular Structure* **1980**, *60*, 93–98.

[93] S. K. Mandal, D. M. Ho, G. Q. Li, M. Orchin, *Polyhedron* **1998**, *17*, 607–611.

[94] G. Q. Li, R. M. Burns, S. K. Mandal, J. K. Bauer, M. Orchin, *Journal of Organometallic Chemistry* **1997**, *549*, 89–94.

[95] A. H. Woomer, T. W. Farnsworth, J. Hu, R. A. Wells, C. L. Donley, S. C. Warren, *ACS Nano* **2015**, *9*, 8869–8884.

[96] J. M. Smieja, C. P. Kubiak, *Inorganic Chemistry* **2010**, *49*, 9283–9289.

[97] S. E. Kegley, D. T. Bergstrom, L. S. Crocker, E. P. Weiss, W. G. Berndt, A. L. Rheingold, *Organometallics* **1991**, *10*, 567–573.

[98] J. F. Moulder, W. F. Stickle, P. E. Sobol, K. D. Bomben, *Handbook of Photoelectron Spectroscopy*, Physical Electronics, Inc., Eden Prairie, **1992**.

[99] J. F. Moulder, W. F. Stickle, P. E. Sobol, K. D. Bomben, J. Chastain, R. C. King Jr., Physical Electronics, Incorporation, Eds. , *Handbook of X-Ray Photoelectron Spectroscopy: A Reference Book of Standard Spectra for Identification and Interpretation of XPS Data*, Physical Electronics, Eden Prairie, Minn., **1995**.

[100] H. B. Ribeiro, M. A. Pimenta, C. J. S. de Matos, *Journal of Raman Spectroscopy* **2018**, *49*, 76–90.

[101] G. Abellán, S. Wild, V. Lloret, N. Scheuschner, R. Gillen, U. Mundloch, J. Maultzsch, M. Varela, F. Hauke, A. Hirsch, *Journal of the American Chemical Society* **2017**, *139*, 10432–10440.

[102] E. Roedel, A. Urakawa, S. Kureti, A. Baiker, *Physical Chemistry Chemical Physics* **2008**, *10*, 6190–6198.

[103] J. García-Álvarez, J. Díez, J. Gimeno, C. M. Seifried, C. Vidal, *Inorganic Chemistry* **2013**, *52*, 5428–5437.

[104] K. Koike, J. Tanabe, S. Toyama, H. Tsubaki, K. Sakamoto, J. R. Westwell, F. P. A. Johnson, H. Hori, H. Saitoh, O. Ishitani, *Inorg. Chem.* **2000**, *39*, 2777–2783.

[105] R. J. Angelici, G. Facchin, M. M. Singh, *Synthesis and Reactivity in Inorganic and Metal-Organic Chemistry* **1990**, *20*, 275–282.

[106] J. M. Smieja, C. P. Kubiak, *Inorg. Chem.* **2010**, *49*, 9283–9289.

[107] Y. Xiao, A. W.-Y. Cheung, S.-W. Lai, S.-C. Cheng, S.-M. Yiu, C.-F. Leung, C.-C. Ko, *Inorg. Chem.* **2019**, *58*, 6696–6705.

4 BP AS A CATALYTIC SUPPORT: HYDROFORMYLATION USING BLACK PHOSPHORUS DECORATED WITH RHODIUM

4.1 INTRODUCTION

Single site heterogeneous catalysts, catalysts composed of isolated, independent active sites immobilized on a support, are a promising route to improve catalytic performance due to their efficient atom economy, increased stability, and multiple handles for tunability.[1] While the active sites can be composed of one or more atoms, they are well-defined which allows traditional organometallic chemistry in addition to materials techniques to be leveraged to probe structure-activity relationships.[2] Electronic interactions between the active site and the support, considered as a ligand with its own electronic and steric properties, provide a handle for tuning the selectivity and activity of the catalyst. Additionally, interactions between the substrate and the support can be utilized to further enhance these metrics.

Black phosphorus (bP), a 2D van der Waals material composed of tricoordinate phosphorus atoms, is a particularly promising support due to its potential for interactions with catalytically active metal centers and substrates. The network of lone pairs has the potential to form dative bonds with Lewis acidic metal centers and donate electron density to the metal, providing a new handle to tune catalytic activity.[3–5] Some evidence of this electron donation can be seen in Section 3.2.2 where functionalization of bP with Re carbonyl complexes resulted in more electron-rich Re centers (Figure 3.2; Figure 3.3). The effect of these electronic metal-support interactions (EMSI) on catalytic activity has been demonstrated for nanoparticles[6,7] and heteromaterials[8,9] with bP; however, to our knowledge, there has yet to be an investigation of bP as a support for a single site catalyst.

Hydroformylation, the catalytic conversion of alkenes to aldehydes, serves as an ideal platform to explore this new type of bP-supported catalyst. It is a critical industrial reaction representing the production of more than 10M metric tons of aldehydes per year.[10] The resulting aldehydes can be used directly, for example in fragrances or pharmaceuticals, or converted into other industrially relevant compounds including alcohols, amines, and carboxylic acids.[10] Typical reaction conditions combine an alkene with a metal carbonyl hydride catalyst and syn gas (1:1 $CO:H_2$) at elevated pressures and temperatures. The most widely used catalysts are either rhodium- or cobalt-based; while cobalt catalysts are still used for long-chain and branched olefins, rhodium catalysts are the industry standard as they can be up to 1000x more active than cobalt, and require lower temperatures and pressures.[10,11]

Importantly, these rhodium catalysts are modified with phosphine ligands to increase their activity and stability.[12] The first phosphine-modified hydroformylation catalysts were introduced in 1965 by Wilkinson;[12] since then, there has been a plethora of research exploring how tuning the phosphine structure and electronic character impacts chemo- and regioselectivity.[10,12] Phosphine precursors typically need to be added in large excesses to stabilize the rhodium species: when too little phosphorus ligand is present, CO will coordinate instead to give the unmodified rhodium species.[10] Black phosphorus as a network of P atoms is well-poised to stabilize the Rh centers while giving a catalyst that can be easily separated from the reaction mixture and an additional handle to tune activity via EMSI. Even more critically, as hydroformylation activity and selectivity are strongly influenced by the electronic and steric character of the phosphine ligand, this reaction can provide insight into how bP behaves in a single site heterogeneous catalyst, creating a scaffold for designing future bP-based catalysts.

Table 4.1. Control reactions for hydroformylation of styrene by Rh@bP.

$Rh(CO)_2(acac)$	bP	% CHO conversion
Y	Y	34 ± 9
N	Y	0
Y	N	0

Herein, hydroformylation activity is reported for a bP-supported Rh catalyst. While this work is on-going, the results obtained thus far begin to shed light on the role of bP as a support for a catalytically active metal.

4.2 Results and Discussion

4.2.1 *Synthesis*

Dispersions of exfoliated black phosphorus were prepared by sonication (18 h, benzonitrile) followed by solvent exchange via filtration. Previous work in our group has shown that this exfoliation process yields high-quality exfoliated bP nanosheets with minimal adventitious oxidation (see Figure 2.8).[13] In a standard reaction, dispersions of bP (0.32 mmol, 0.032 M) in toluene were combined with $Rh(CO)_2(acac)$ (0.03 mmol) and an olefin (0.66 mmol) in a Parr reactor and heated to 90°C under 110 psi of syngas for 2 h. Post-reaction, the nanosheets were separated from soluble species via filtration. Species remaining in the organic phase (filtrate) were analyzed by NMR and GC-MS. Isolated nanosheets were preliminarily characterized via ICP-MS and spectroscopic methods (IR, XPS).

4.2.2 *Identifying the Role of Black Phosphorus in Catalysis*

A variety of substrates were screened for hydroformylation activity including terminal aliphatic, internal aliphatic, functionalized, aryl, and cyclic olefins. In all cases, hydroformylation activity was observed (Figure 4.8); for further studies, three substrates, styrene, 1-hexene, and 3,3-dimethylbutene, were selected as these olefins are among the most common in hydroformylation literature, and because they allow multiple parameters (e.g. steric profile, isomerization activity, regioselectivity) to be investigated in depth.

Control experiments with styrene demonstrate that bP plays a critical role in the observed hydroformylation activity. Reactions performed in the absence of bP or in the absence of $Rh(CO)_2(acac)$ show no hydroformylation; activity is only observed when both $Rh(CO)_2(acac)$ and bP are present (Table 4.1). Further temperature and pressure dependence studies showed no significant change in n/iso isomer ratio, consistent with Rh@bP as the only catalytic species (Figure 4.2).[11,14] As a result, while Rh species without phosphine ligands can be active for hydroformylation,[12,15] there is no evidence of catalytically active unmodified Rh species, such as $HRh(CO)_4$, generated *in situ*, likely because the reaction parameters are too mild (see Section 4.4.3 for details).[11]

While preliminary ICP-MS and XPS of the nanosheets isolated post-catalysis show high Rh:P ratios, the identity of the catalytic species Rh@bP is uncertain at the time of writing. Preliminary characterization suggests that low-valent Rh with some carbonyl ligands remains on the bP surface

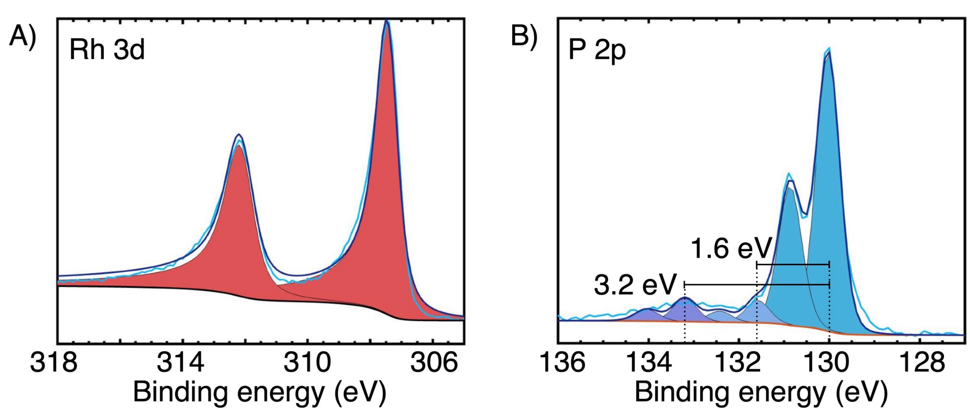

Figure 4.1. High-resolution (A) P 2p, and (B) Rh 3d XPS of Rh@bP. Higher energy P 2p environments are fit as if they correspond to discrete chemical species, however, the exact fitting is uncertain.

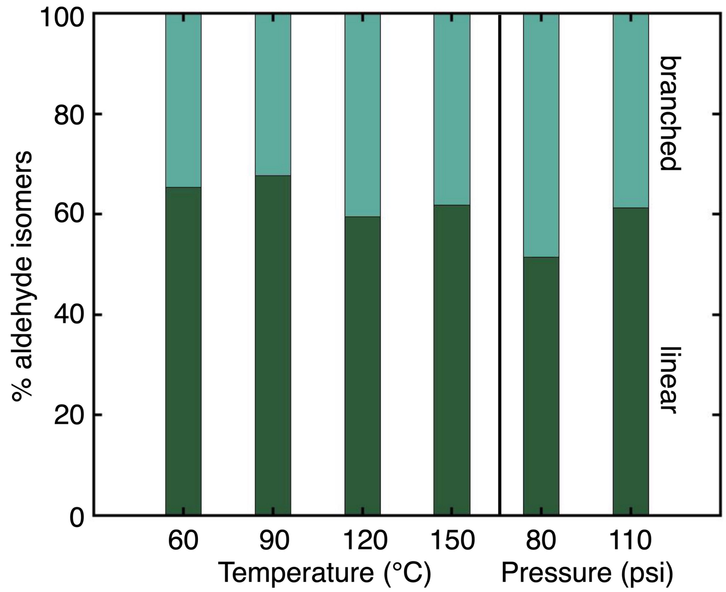

Figure 4.2. Pressure and temperature dependence of n/iso for the hydroformylation of styrene by Rh@bP.

post-catalysis. Notably, this characterization was performed *ex situ* and likely does not represent the pre-catalytic or active catalytic species under hydroformylation conditions.

High-resolution XPS characterization of the nanosheets post-catalysis show one Rh environment at 307.4 eV (Figure 4.1). Comparison of the Rh $3d_{5/2}$ binding energy with literature[16] shows that this binding energy lies between Rh(0) and Rh(I), suggesting that the environment is either an electron-deficient Rh(0) or electron-rich Re(I) species. High-resolution P 2p XPS shows higher energy P environments in addition to the primary P(0) feature observed at 130.0 eV. These environments compose *ca.* 13% of P in the area sampled and are in the binding energy range for phosphorus oxides. However, the broadness of the feature prevents precise fitting; further investigation is required to assign them more conclusively.

A DRIFTS spectrum of Rh@bP isolated post-catalysis shows a broad feature at centered at 2017 cm^{-1} corresponding to CO (Figure 4.3). This feature is significantly broader than the CO stretches observed for the precursor $Rh(CO)_2(acac)$, potentially suggesting that multiple binding modes in Rh@bP. Comparison with control DRIFTS spectra reveal a similar CO feature observed when bP and $Rh(CO)_2(acac)$ are stirred together at room temperature. Based on molecular phosphine analogs of this reaction, the expected product is Rh(CO)(acac)(bP);[17,18] however, literature analogs of this structure show CO stretches at lower energies (e.g. 1984 cm^{-1} for $Rh(CO)(acac)(PPh_3)$[17]) than observed for Rh@bP or the room temperature control. In contrast, molecular $[Rh(CO)(PR_3)_3][X]$ complexes show CO stretches at very similar energies to those observed (e.g. 2026 cm^{-1} for $[Rh(CO)(triphos)][PF_6]$[19]), possibly indicating a multidentate bP binding mode.[19,20]

4.2.3 *Effect of Substrate Identity on Activity and Selectivity*

Of the three substrates examined in detail, hydroformylation of 1-hexene showed the greatest activity for hydroformylation (TOF = 1.6 h^{-1}). However, a high degree of olefin isomerization was observed in addition to hydroformylation (Table 4.2) with TOFs *ca.* 2x greater than those observed for hydroformylation. While phosphine-modified Rh species are typically poor catalysts for alkene isomerization, there are instances where appreciable amounts of isomerization are observed: for example, Rh with bulky bidentate BIPHEPHOS derivatives[21] and Rh(III) catalysts[12] are known to catalyze significant amounts of isomerization. This result potentially hints at multidentate bP coordination or oxidation occurring during the reaction.

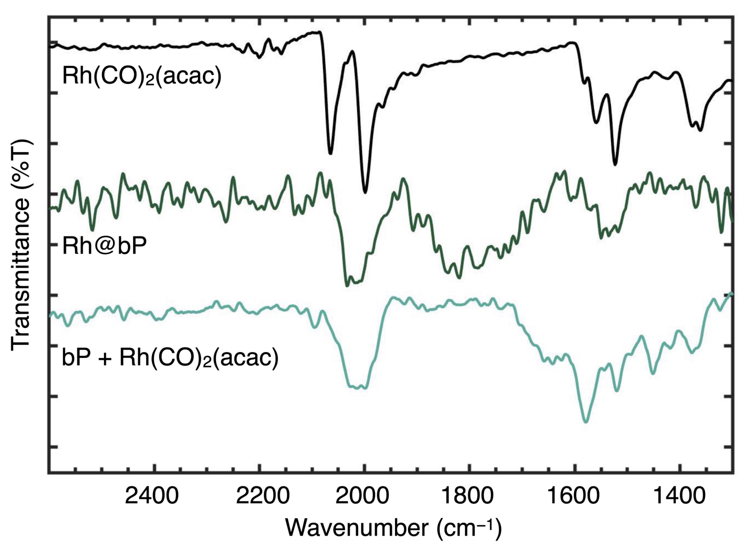

Figure 4.3. DRIFTS spectrum of Rh@bP isolated post-catalysis overlaid with $Rh(CO)_2(acac)$ and bP + $Rh(CO)_2(acac)$.

Little selectivity between isomers is observed: n/iso = 1.1. This is distinct from both unmodified and molecular phosphine-modified Rh, which favor the linear isomer, heptanal.[10,11] Although 2-hexene is present in the reaction due to isomerization, at 2 h, none of the

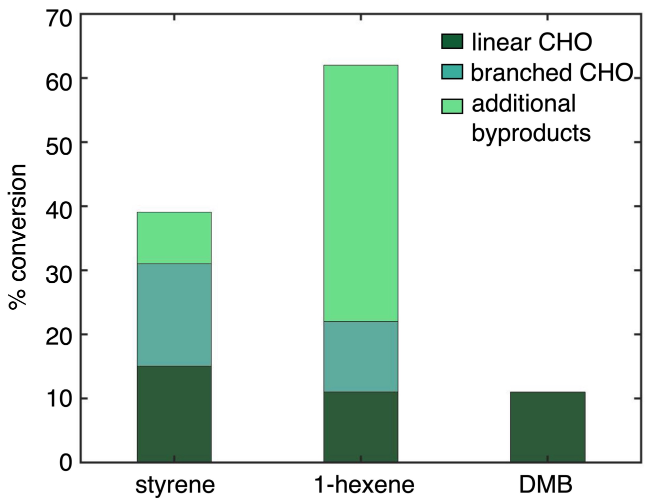

Figure 4.4 Product distribution for Rh@bP-catalyzed hydroformylation of styrene, 1-hexene, and 3,3-dimethylbutene (DMB).

internal olefin is hydroformylated: all aldehydes observed come from direct hydroformylation of 1-hexene (Figure 4.9). However, if the reaction time is extended to 20 h, small amounts of 2-hexene hydroformylation are observed (Table 4.2; Figure 4.9).

As 1-hexene isomerization competes with hydroformylation, 3,3-dimethylbutene (DMB) was chosen as a substrate to inhibit the isomerization pathway. With DMB, *ca.* 11% of the olefin is converted to the linear aldehyde, 4,4-dimethylpentanal; no other products are observed (Table 4.2). The lower activity compared to 1-hexene is likely due to the increased steric hindrance of DMB.[22] However, it is important to note that the DMB conversion is preliminary (see Table 4.2 caption for details). As this reaction proceeded smoothly with no competing catalytic processes, DMB was selected as the substrate for kinetic studies in accordance with literature precedent (Section 4.2.4).[12]

In contrast to 1-hexene, the hydroformylation of styrene does show some regioselectivity: n/iso = 1.5. This is also in contrast to unmodified rhodium and mono- and bis-phosphine rhodium carbonyl hydrido complexes, which show strong preference for the branched isomer.[11,14] For styrene, this is particularly interesting as the preference for the branched isomer is characteristic of styrene rather than the identity of the catalyst and derives from the stability of the intermediate η^3-benzylic rhodium complex.[23] However, with bulky chelating phosphite ligands, selectivity for the linear isomer has been observed primarily due to steric constraints but also due to the strong π-accepting character of the ligands.[24–29] This could indicate a higher coordination mode of Rh on bP (e.g. κ^2 or κ^3); however, buried volume calculations (Section 3.2.5) suggest that even in a κ^2 binding mode, bP is about as bulky as PPh_3, making it less hindered than the bulky phosphite ligands studied. It could also indicate a new lower-energy transition state in the hydroformylation mechanism, making the linear pathway more favorable than the branched. Energetically favorable cyclic transition states are known for specific phosphinite ligand-substrate pairs due to weak interactions between the P atoms and the functional group on the olefin.[30,31] Recent work suggests that small organic molecules do interact with the bP surface: molecules including toluene, hexane, isopropanol, and acetone have been shown to dope the bP surface via physisorption.[32] More investigation is required to determine which possibility is more likely.

4.2.4 *Kinetic Studies with 3,3-dimethylbutene*

Kinetic studies were performed with respect to DMB concentration ([DMB]) to determine the reaction order of Rh@bP with respect to this parameter. These studies appear to reveal a pseudo-zero-order dependence on [DMB]. Given the relatively low substrate loading relative to the

Table 4.2. Activity and selectivity of Rh@bP for various olefins. Reaction conditions: 90°C, 2 h, S/Rh = 22, bP/Rh = 11. [a]TOF = mmol compound / mmol Rh added / time. TOF_{other} for styrene is TOF of hydrogenation; for 1- and 2-hexene, it is TOF of isomerization. [b]Data obtained after 20 h; reactions collected at 2 h showed no conversion. [c]Amount of linear aldehyde produced was estimated by mmol DMB added – mmol DMB remaining.

Substrate	**Conversion %**	**CHO Conversion %**	**n/iso**	**TOF_{ald} (h^{-1})[a]**	**TOF_{other} (h^{-1})[a]**
styrene[b]	39	31	1.5	0.3	0.2
1-hexene	62	22	1.1	1.6	4.1
3,3-dimethylbutene[c]	11	11	–	1.2	–
2-hexene[b]	17	8	0.6	0.1	0.03

amount of Rh precursor added to the reaction (S/Rh = 11–163), this result is quite surprising. It is in contrast to the vast majority of molecular hydroformylation catalysts which show first order dependence on [olefin], referred to as "type-I" catalysts.[33] A minority of catalysts, referred to as "type-II," show zero-order dependence on [olefin]. These include unmodified Rh species as well as some phosphine-, monophosphite-, and bisphosphite-modified Rh species.[33–35] The two types of [olefin] dependencies are associated with important mechanistic considerations including the rate-limiting step and resting state of the catalyst.[33] For type-I catalysts, the rate-limiting step is alkene addition and the resting state is the five-coordinate $HRh(CO)(PR_3)_2$; for type-II catalysts, hydrogenolysis is rate-limiting and the acyl complex is the resting state.[36]

Zero-order dependence on substrate concentration can occur due to a variety of factors including steric bulk and electronic character of the ligand as well as interactions between reagents and a support.[37,38] However, in our system, preliminary evidence suggests that the loading of active catalytic sites is significantly lower than the amount of $Rh(CO)_2(acac)$ added. As a result, the olefin would be in vast excess compared to the number of active catalytic sites even at $S/Rh(CO)_2(acac)$

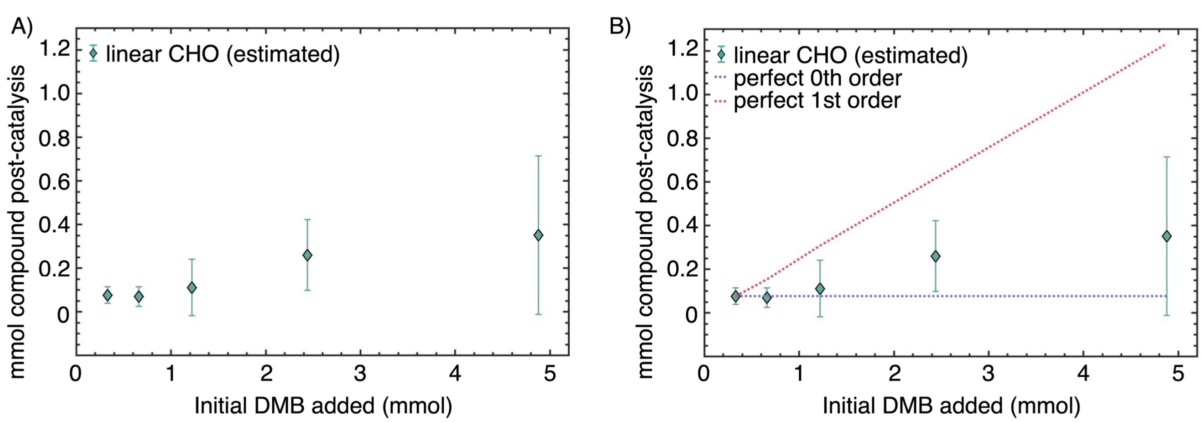

Figure 4.5. Dependence of hydroformylation on DMB added. (A) mmol of DMB recovered and 4,4-methylpentanal produced versus increasing amounts of added DMB. (B) Zoom-in on 4,4-methylpentanal data with expected trends for perfect 0th and 1st order dependence overlaid. mmol of 4,4-methylpentanal estimated by mmol DMB added – mmol DMB remaining.

= 11. When high S/Cat occurs for molecular catalysts, there is a shift from type-I to type-II behavior as the alkene addition step becomes faster.[35] The low loading of catalytic active sites in our system is further supported by preliminary $Rh(CO)_2(acac)$ concentration studies.

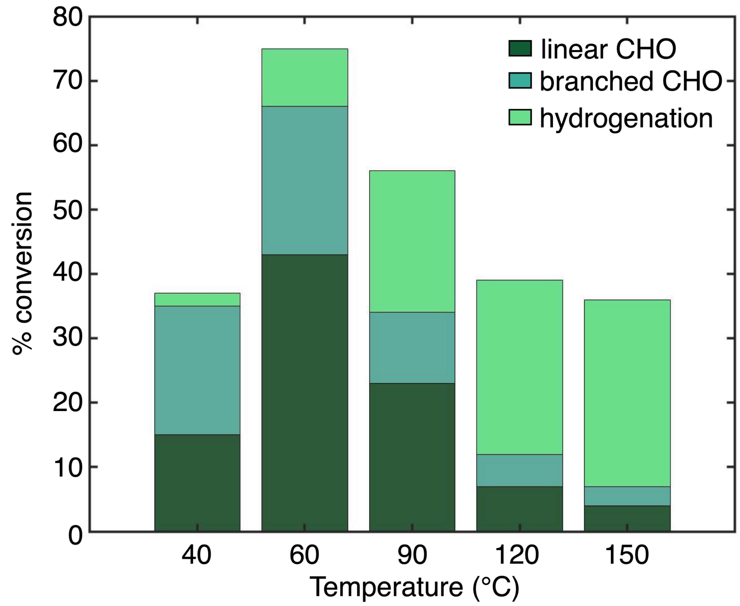

Figure 4.6. Temperature dependence for the hydroformylation of styrene by Rh@bP.

4.2.5 *Optimization of Temperature and Rh Concentration*

Further optimization studies of temperature and Rh/bP ratio were performed with styrene. Temperature studies revealed similar trends to those observed for molecular phosphine-modified Rh catalysts.[39] As temperature is increased from 40–120°C, n/iso also increased from 1.1 to 1.6 (Figure 4.2, Figure 4.6). Over the same temperature range, catalytic activity for hydroformylation peaked at *ca.* 60°C with activity significantly decreasing at 120°C due to increased hydrogenation. Hydrogenation activity steadily increased with temperature, likely due to the increased favorability of CO dissociation at higher temperatures (Figure 4.6).[33]

Adjusting the Rh/bP ratio produced mixed results. Typically, increasing the amount of phosphine relative to Rh increases the rate of hydroformylation by stabilizing the active catalyst.[10] However, increasing the amount of bP (decreasing Rh/bP from 0.09–0.02) ultimately shut down hydroformylation activity for styrene at Rh/bP = 0.02. This unusual result could be due to

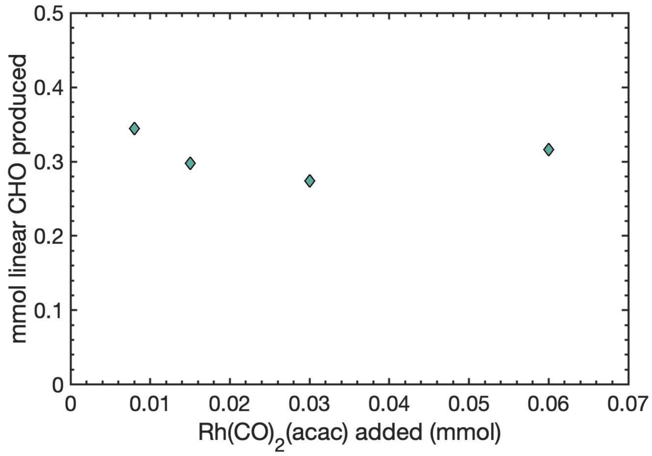

Figure 4.7. Dependence of % DMB conversion on Rh/bP. Amounts of linear aldehyde were estimated from mmol DMB added – mmol DMB remaining.

nanosheet aggregation induced by the hydroformylation reaction conditions, resulting in inaccessible Rh active sites. However, switching to a solvent where bP shows higher dispersibility, benzonitrile, or increasing the overall solvent volume did not change this result.

Interestingly, neither increasing nor decreasing the amount of $Rh(CO)_2(acac)$ gives changes in activity. While this result is preliminary, these data suggest that within this regime (Rh/bP = 0.02–0.2), changing the amount of $Rh(CO)_2(acac)$ does not result in more active sites (Figure 4.7). This result in is distinct contrast to molecular catalysts which show 1st order dependence on Rh precursor concentration for both type-I and type-II catalysts and strongly suggests that the active catalyst is immobilized on the bP surface.[33] This would imply that all available surface sites on bP are saturated at Rh/bP = 0.02; however, the exact Rh/bP value where saturation occurs will also depend on the degree of nanosheet exfoliation, which has not yet been investigated with respect to activity. Preliminary ICP-MS supports this hypothesis: analysis of the post-catalysis organic phase shows some soluble Rh remaining after bP removal. The presence of this soluble Rh could indicate leaching, however, based on these preliminary $Rh(CO)_2(acac)$ concentration studies, excess $Rh(CO)_2(acac)$ that does not interact with bP appears more likely.

4.3 CONCLUSION

While these results are preliminary, it is clear that bP plays a key role in the observed hydroformylation activity. The behavior of the Rh@bP catalyst differs in distinct ways from traditional molecular phosphine catalysts including an unusual selectivity for the linear aldehyde of styrene and zero-order dependence on [DMB] and Rh(acac)$(CO)_2$. These saturation-type kinetics strongly suggest that the active catalyst is immobilized on the bP surface. In general, much of the data suggests that Rh@bP behaves similarly to bulky phosphite-modified Rh. This may indicate that steric constraints imposed by bP play a large role in activity and selectivity; it could also suggest that Rh is interacting with adventitious PO sites on the bP surface. Further reactions with intentionally oxidized bP could shed light on this question. Preliminary characterization of this species post-catalysis suggests a high surface loading of Rh with some carbonyl groups intact. In order to probe the nature of Rh@bP further and begin to correlate structure-activity relationships, additional characterization via vibrational and X-ray spectroscopies and imaging techniques is required both pre- and post-catalysis.

4.4 EXPERIMENTAL

4.4.1 *Materials*

Unless stated otherwise, all work was performed under an inert atmosphere of N_2 using a Schlenk line or inside of an LC Technology Solutions, Inc. glove box containing <5 ppm H_2O and O_2. All glassware was dried at 160˚C for a minimum of 12 h and cooled under vacuum prior to use. All solvents excluding benzonitrile were purchased from Fischer Scientific. Anhydrous solvents were dispensed from a JC Meyer solvent system and stored over 3 Å molecular sieves (Thermo-Fisher) for at least 12 h before use. Molecular sieves were previously activated under vacuum at 300˚C for 48 h. Benzonitrile (99%, Alfa Aesar) was degassed for at least 6 hours under vacuum and stored over activated 3Å molecular sieves in the glovebox for a minimum of 72 h prior to use.

All reagents were stored in a glovebox. $Rh(CO)_2(acac)$ (98%, Sigma-Aldrich), undecane (>99%, Sigma-Aldrich), and $CDCl_3$ (99.8 atom% D (1% v/v TMS, Sigma-Aldrich) were used as received. Styrene (ReagentPlus®, contains 4-tert-butylcatechol as stabilizer, ≥99%, Sigma-Aldrich), 1-hexene (98%, ThermoFisher), 3,3-dimethyl-1-butene (>97%, Sigma-Aldrich), *trans*-2-hexene (97%, Sigma-Aldrich), 5-hexene-1-ol (98%, Sigma-Aldrich), 1-octene (98%, Sigma-Aldrich), *trans*-2-octene (97%, Sigma-Aldrich), 1,5-cyclooctadiene (contains 4-tert-butylcatechol as stabilizer, 99%, Sigma-Aldrich), heptanal (95%, Sigma-Aldrich), 3-phenylpropanal (≥95%, Sigma-Aldrich), 2-phenylpropanal (98%, Sigma-Aldrich), and ethylbenzene (anhydrous, 99.8%, Sigma Aldrich) were degassed via freeze-pump-thaw and stored over 3 Å molecular sieves.

Black phosphorus (bP) crystals were synthesized using the methods in Reference [40]. Crystals of black phosphorus (bulk bP; 120 mg) were finely crushed with an agate mortar and pestle. The resulting fine, silver-black powder was subsequently sonicated in the dark for 20 h in anhydrous benzonitrile (120 mL). Air-free 250-mL Schlenk flasks sealed with Teflon stoppers were used to prevent air exposure. The resulting suspensions were brown and opaque. The solids were isolated via filtration and washed extensively with toluene to remove residual benzonitrile. The solids were then resuspended in toluene via ultrasonication.

4.4.2 *Instrumentation*

Ultrasonication was performed in a 110W bath sonicator at 40 kHz. Circulation cooling was used to maintain a bath temperature of 22–28˚C. Filtrations were performed with EMD Millipore Omnipore hydrophobic membrane filters with a pore size of 0.2 μm. Hydroformylation reactions were performed in 50 mL Parr Instrument Micro Benchtop Model 4590 Reactors equipped with PTFE flat gaskets, Teflon-coated overhead stir rods, and an internal thermocouple. The system was controlled by a 4848 controller and SpecView version 3 software.

GC-MS spectra were collected on an Agilent Technologies 5973 GC-MS instrument. Quantitative analysis was performed using calibration curves made at standard concentrations and 0.025 M undecane as the internal standard. ^{1}H NMR was collected on a 300 MHz Burker AVance instrument. Attenuated total reflectance infrared (ATR-IR) spectra were recorded on a Bruker Alpha IR instrument equipped with a Platinum ATR accessory. Diffuse reflectance infrared Fourier transform spectroscopy (DRIFTS) was used in some analyses with the corresponding Bruker DRIFTS accessory and FTIR-grade potassium bromide (KBr, >99%; Alfa Aesar).

4.4.3 *General hydroformylation reaction conditions*

Catalytic reactions were assembled in air-free conditions inside a glovebox. Standard reaction mixtures were composed of $Rh(CO)_2(acac)$ (8.3 mg, 0.03 mmol), black phosphorus (10 mg, 0.32 mmol), olefin (0.66 mmol), and 10 mL of dry toluene. All liquid-phase reagents were measured by micropipette; a stock solution of $Rh(CO)_2(acac)$ in toluene was prepared and transferred to the reactor via micropipette. Standard reaction conditions were 110 psi 1:1 $CO:H_2$, 90°C, and 200 rpm stirring for 2h. Any modifications to both reaction mixture composition and/or reaction conditions are noted where applicable. After cooling down, the reactors were purged with N_2 and disassembled in air-free conditions. Reactions were worked up air-free, and the organic products were separated from the nanosheets via filtration through a Celite plug. The organic phase was characterized by ^{1}H NMR and GC-MS with 0.025 M undecane added as an internal standard. In between reaction work-up and measurements, the organic phase and the nanosheets were stored at −25°C.

4.4.4 *Kinetic studies with 3,3-dimethylbutene*

Kinetic studies were performed in triplicate and characterized using quantitative GC-MS. Calibration curves for each substrate, product, and by-product were obtained independently using 0.025 M undecane as an internal standard. The calibration curves consisted of at least 20 data points from $6.25\text{x}10^{-4}$ – 0.12M. Standard calibration curve samples were prepared in toluene via serial dilution. Samples of reaction mixtures were prepared via micropipette with 500 µL of the post-reaction organic phase, 500 µL of toluene, and 1 mL of a 0.05 M undecane solution in toluene. Multiple GC-MS measurements of the same sample were within ±2%.

4.5 ADDITIONAL CHARACTERIZATION

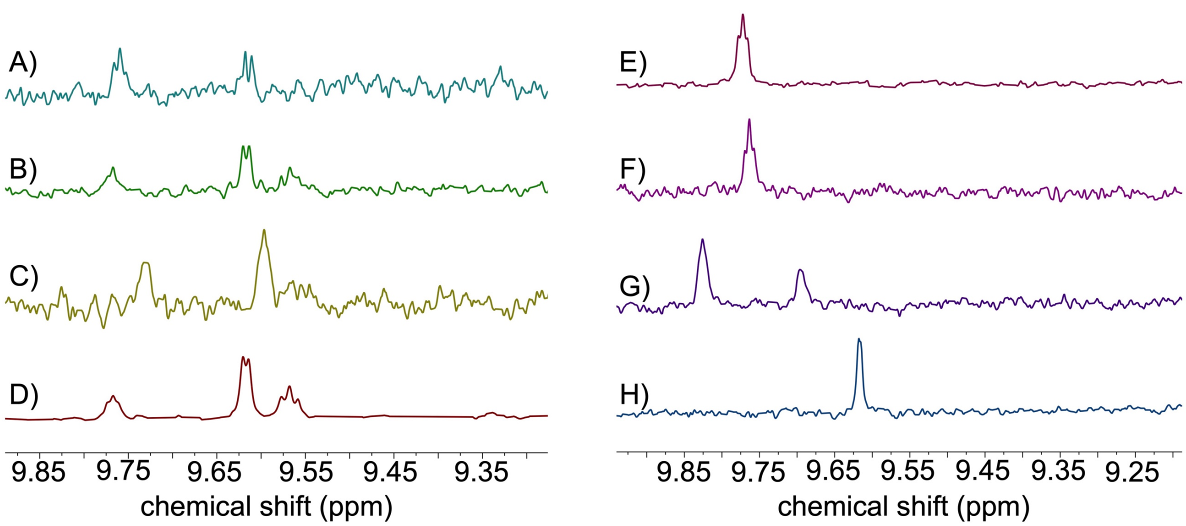

Figure 4.8. ^{1}H NMR ($CDCl_3$) spectra of the hydroformylation of A) 1-hexene, B) 1-octene, C) 2-hexene, D) 2-octene, E) 3,3-dimethylbutene, F) 5-hexenol, G) styrene, and H) cyclooctadiene. All features correspond to aldehyde isomers.

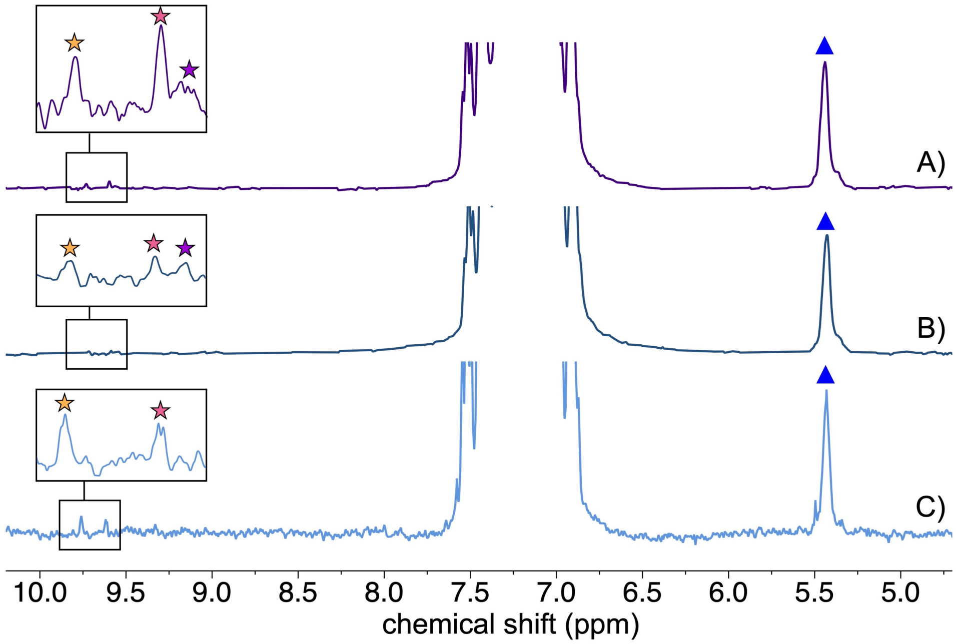

Figure 4.9. Effect of terminal versus internal olefins. ^{1}H NMR ($CDCl_3$) spectra of the hydroformylation of A) 2-hexene after 20 h, B) 2-hexene after 2 h, and C) 1-hexene after 2 h. Insets show zoom-in on aldehyde features where yellow, pink, and purple stars denote the linear, branched, and internal aldehyde isomers. Only trace aldehydes were observed in B.

4.6 References

[1] J. M. Thomas, R. Raja, D. W. Lewis, *Angew. Chem. Int. Ed.* **2005**, *44*, 6456–6482.

[2] J. D. A. Pelletier, J.-M. Basset, *Acc. Chem. Res.* **2016**, *49*, 664–677.

[3] A. Ienco, G. Manca, M. Peruzzini, C. Mealli, C. Organometallici, C. Nazionale, *Dalton Transactions* **2018**, *47*, 17243–17256.

[4] Z. Sofer, D. Sedmidubský, Š. Huber, J. Luxa, D. Bouša, C. Boothroyd, M. Pumera, *Angew. Chem. Int. Ed.* **2016**, *55*, 3382–3386.

[5] X. Liu, K. Chen, X. Li, Q. Xu, J. Weng, J. Xu, *Adv. Mater.* **2021**, 2005924.

[6] H. Qiao, H. Liu, Z. Huang, Q. Ma, S. Luo, J. Li, Y. Liu, J. Zhong, X. Qi, *Advanced Energy Materials* **2020**, *10*, 2002424.

[7] M. Vanni, M. Caporali, M. Serrano-Ruiz, M. Peruzzini, *Surfaces* **2020**, *3*, 132–167.

[8] J. Li, H. Ma, J. Wang, X. Luo, L. Yu, J. Gao, *ChemistrySelect* **2021**, *6*, 5899–5905.

[9] Z.-Z. Luo, Y. Zhang, C. Zhang, H. T. Tan, Z. Li, A. Abutaha, X.-L. Wu, Q. Xiong, K. A. Khor, K. Hippalgaonkar, J. Xu, H. H. Hng, Q. Yan, *Adv. Energy Mater.* **2017**, *7*, 1601285.

[10] R. Franke, D. Selent, A. Börner, *Chem. Rev.* **2012**, *112*, 5675–5732.

[11] D. M. Hood, R. A. Johnson, A. E. Carpenter, J. M. Younker, D. J. Vinyard, G. G. Stanley, *Science* **2020**, *367*, 542–548.

[12] A. Börner, R. Franke, *Hydroformylation: Fundamentals, Processes, and Applications in Organic Synthesis*, Wiley-VCH Verlag GmbH & Co. KGaA, Weinheim, **2016**.

[13] K. L. Walz Mitra, C. H. Chang, M. P. Hanrahan, J. Yang, D. Tofan, W. M. Holden, N. Govind, G. T. Seidler, A. J. Rossini, A. Velian, *Angew. Chem. Int. Ed.* **2021**, *60*, 9127–9134.

[14] J. Feng, M. Garland, *Organometallics* **1999**, *18*, 417–427.

[15] A. J. Bruss, M. A. Gelesky, G. Machado, J. Dupont, *Journal of Molecular Catalysis A: Chemical* **2006**, *252*, 212–218.

[16] C. Powell, **1989**, DOI 10.18434/T4T88K.

[17] J. Zakzeski, H. R. Lee, Y. L. Leung, A. T. Bell, *Applied Catalysis A: General* **2010**, *374*, 201–212.

[18] L. Chen, P. Ren, B. P. Carrow, *J. Am. Chem. Soc.* **2016**, *138*, 6392–6395.

[19] A. M. Gull, J. M. Blatnak, C. P. Kubiak, *Journal of Organometallic Chemistry* **1999**, *577*, 31–37.

[20] J. A. Osborn, R. R. Schrock, *J. Am. Chem. Soc.* **1971**, *93*, 2397–2407.

[21] C. Vogl, E. Paetzold, C. Fischer, U. Kragl, *Journal of Molecular Catalysis A: Chemical* **2005**, *232*, 41–44.

[22] A. Van Rooy, *Journal of Organometallic Chemistry* **1996**, *507*, 69–73.

[23] S. Deerenberg, P. C. J. Kamer, P. W. N. M. van Leeuwen, *Organometallics* **2000**, *19*, 2065–2072.

[24] S. Yu, Y. Chie, Z. Guan, Y. Zou, W. Li, X. Zhang, *Org. Lett.* **2009**, *11*, 241–244.

[25] C. Cai, S. Yu, B. Cao, X. Zhang, *Chem. Eur. J.* **2012**, *18*, 9992–9998.

[26] P. E. Goudriaan, M. Kuil, X.-B. Jiang, P. W. N. M. van Leeuwen, J. N. H. Reek, *Dalton Trans.* **2009**, 1801.

[27] D. Sémeril, D. Matt, L. Toupet, *Chem. Eur. J.* **2008**, *14*, 7144–7155.

[28] O. Tissot, M. Gouygou, F. Dallemer, J.-C. Daran, G. G. A. Balavoine, *Eur. J. Inorg. Chem.* **2001**, *2001*, 2385–2389.

[29] C. B. Dieleman, P. C. J. Kamer, J. N. H. Reek, P. W. N. M. van Leeuwen, *HCA* **2001**, *84*, 3269–3280.

[30] C. U. Grünanger, B. Breit, *Angew. Chem. Int. Ed.* **2008**, *47*, 7346–7349.

[31] Y. Ueki, H. Ito, I. Usui, B. Breit, *Chem. Eur. J.* **2011**, *17*, 8555–8558.

[32] Y. Wang, A. Slassi, J. Cornil, D. Beljonne, P. Samorì, *Small* **2019**, *15*, 1903432.

[33] P. W. N. M. van Leeuwen, C. Claver, Eds. , *Rhodium Catalyzed Hydroformylation*, Kluwer Academic Publishers, Dordrecht [Netherlands] ; Boston, **2000**.

[34] C. Kubis, D. Selent, M. Sawall, R. Ludwig, K. Neymeyr, W. Baumann, R. Franke, A. Börner, *Chem. Eur. J.* **2012**, *18*, 8780–8794.

[35] A. C. Brezny, C. R. Landis, *J. Am. Chem. Soc.* **2017**, *139*, 2778–2785.

[36] S. S. Nurttila, P. R. Linnebank, T. Krachko, J. N. H. Reek, *ACS Catal.* **2018**, *8*, 3469–3488.

[37] A. van Rooy, E. N. Orij, P. C. J. Kamer, P. W. N. M. van Leeuwen, *Organometallics* **1995**, *14*, 34–43.

[38] L. Wang, W. Zhang, S. Wang, Z. Gao, Z. Luo, X. Wang, R. Zeng, A. Li, H. Li, M. Wang, X. Zheng, J. Zhu, W. Zhang, C. Ma, R. Si, J. Zeng, *Nat Commun* **2016**, *7*, 14036.

[39] C. G. Arena, D. Drago, F. Faraone, *Journal of Molecular Catalysis A: Chemical* **1999**, *144*, 379–388.

[40] A. H. Woomer, T. W. Farnsworth, J. Hu, R. A. Wells, C. L. Donley, S. C. Warren, *ACS Nano* **2015**, *9*, 8869–8884.

APPENDIX A. SUPPLEMENTAL INFORMATION FOR CHAPTER 2

A.1 ADDITIONAL CHARACTERIZATION OF FUNCTIONALIZED BLACK PHOSPHORUS NANOSHEETS (RN–BP)

A.1.1. *Solid state NMR*

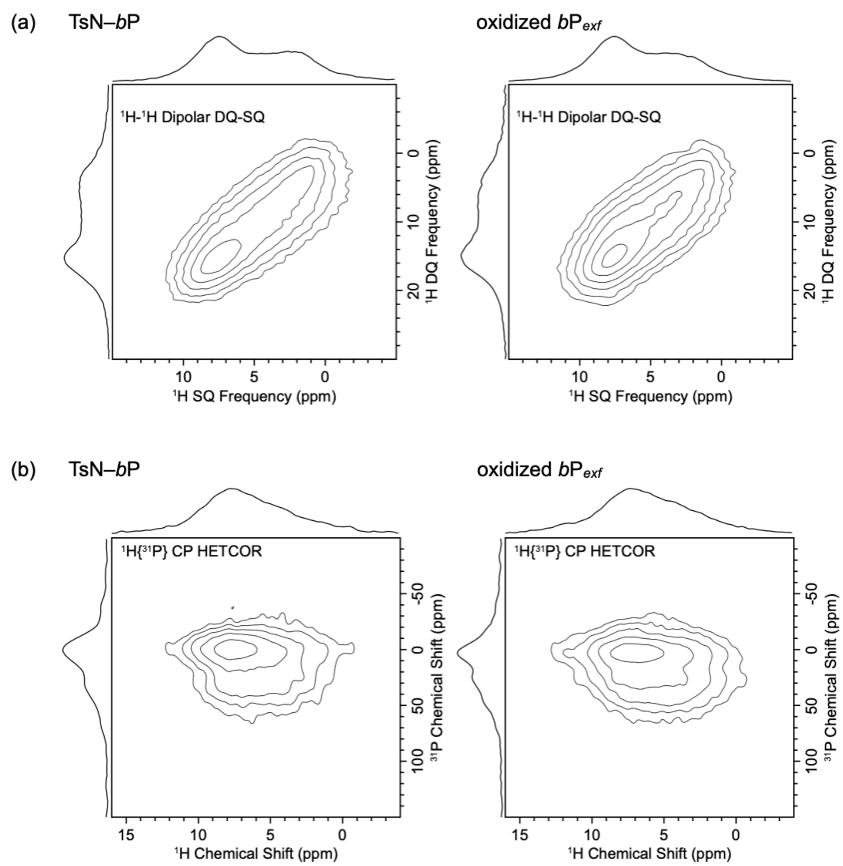

Figure A.1. 2D NMR of TsN–bP and oxidized bP$_{exf}$. (a) ^{1}H–^{1}H dipolar DQ-SQ and (b) ^{1}H{^{31}P} CP HETCOR of TsN–bP and oxidized bP$_{exf}$. The oxidized bP$_{exf}$ was prepared by sonicating mechanically crushed bP in PhCN for five days. IR characterization of this material shows significant oxidation.

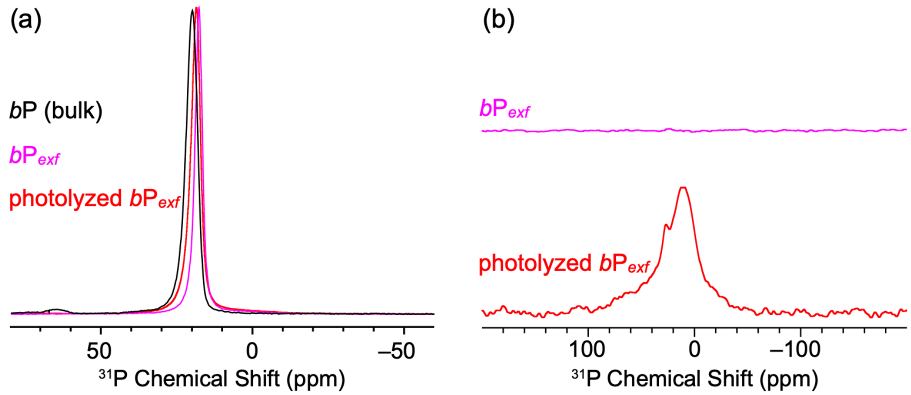

Figure A.2. 1D NMR of bP_{exf} and photolyzed bP_{exf}. (a) Direct excitation ^{31}P solid state NMR spectra of bulk bP, bP_{exf}, and photolyzed bP_{exf}. (b) $^{1}H \rightarrow ^{31}P$ CPMAS spectra of bP_{exf} and photolyzed bP_{exf}. The spectrum of photolyzed bP_{exf} was obtained with 8192 scans while that of bP_{exf} was obtained with 256 scans. CP contact times of 5 ms were used in both cases.

A.1.2. *X-ray photoelectron spectroscopy*

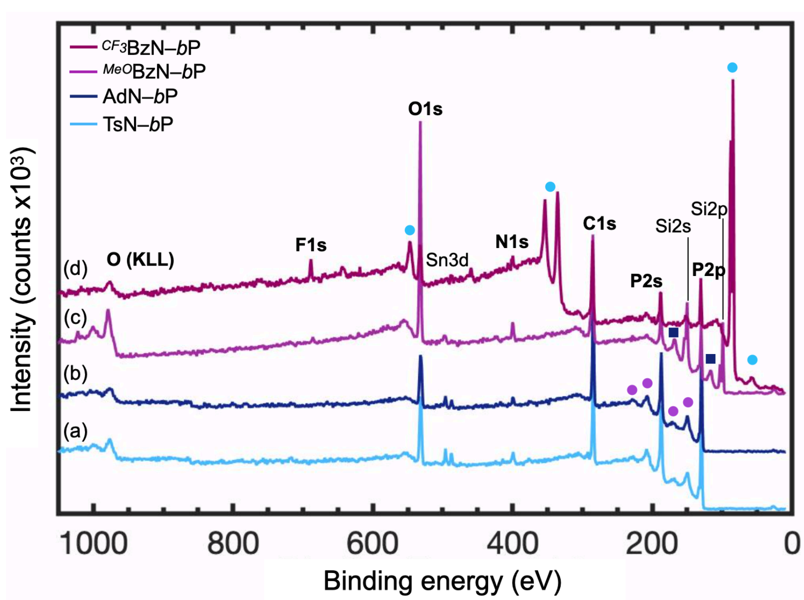

Figure A.3. XPS survey spectra for (a) TsN–bP, (b) AdN–bP, (c) ^{MeO}BzN–bP, and (d) ^{CF_3}BzN–bP. bP plasmon satellites (purple circles), Si satellites (navy squares), and signals from the Au support (blue circles) are labeled. bP plasmon satellites were identified using Taniguchi, *Solid State Commun.* **1983**, *45*, 59 and Brunner, *J. Phys. Chem. Solids* **1979**, *40*, 967.

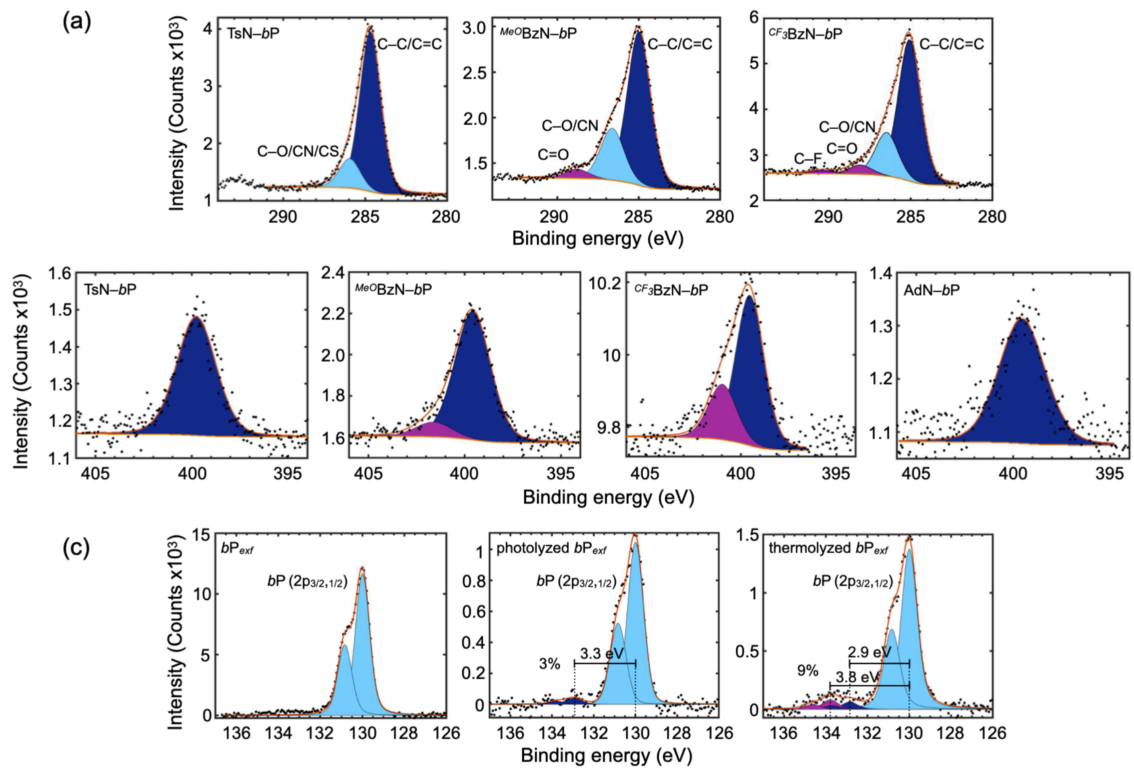

Figure A.4. High-resolution XPS of select materials. (a) High-resolution C1s XPS of TsN–bP, ^{MeO}BzN–bP, and ^{CF_3}BzN–bP. The feature at 293 eV in TsN–bP is a shakeup satellite. Assignments were determined using Reference 9. (b) High-resolution N1s XPS of TsN–bP, ^{MeO}BzN–bP, ^{CF_3}BzN–bP, and AdN–bP. (c) High-resolution P2p XPS of controls.

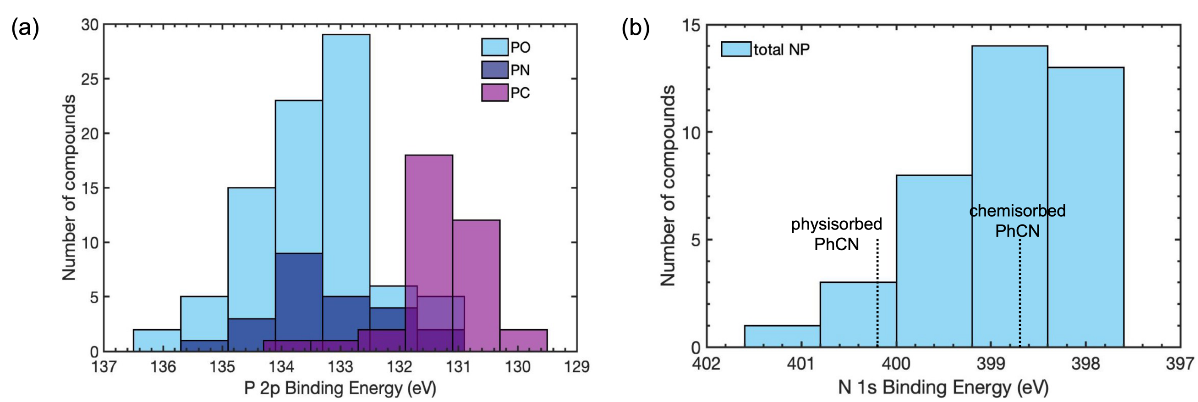

Figure A.5. Literature survey of reported XPS binding energies. The majority of these values were obtained from the NIST X-ray Photoelectron Spectroscopy Database. (a) Histogram of reported P2p binding energies for PN, PO, and PC bonds. (c) Histogram of reported N1s binding energies for both P–N and P=N bonds. The majority of these binding energies fall near the values expected for PhCN (398.7 eV for chemisorbed and 400.2 for physisorbed).

A.1.3. *Additional characterization techniques*

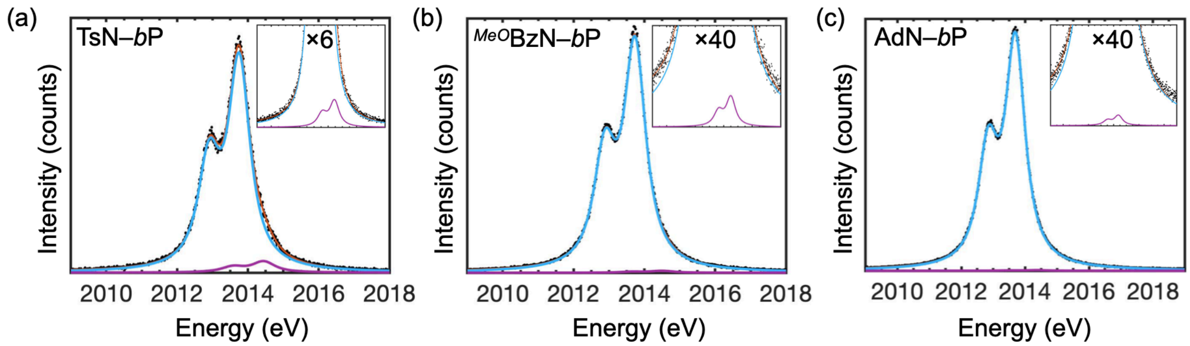

Figure A.6. XES spectra for (a) TsN–*b*P, (b) ^{MeO}BzN–*b*P, and (c) AdN–*b*P. The primary Kα_1,α_2 environment (blue) corresponds to P(0) from unfunctionalized P atoms; the lower intensity Kα_1,α_2 environment (purple) corresponds to oxidized P sites, which includes both PN and PO. The percent oxidation was found to be (a) 5.2 ±10%, (b) 0.9% ±40%, and (c) 0.3% ± >40%, consistent with the higher degree of exfoliation for TsN–bP compared to ^{MeO}BzN–bP and AdN–bP.

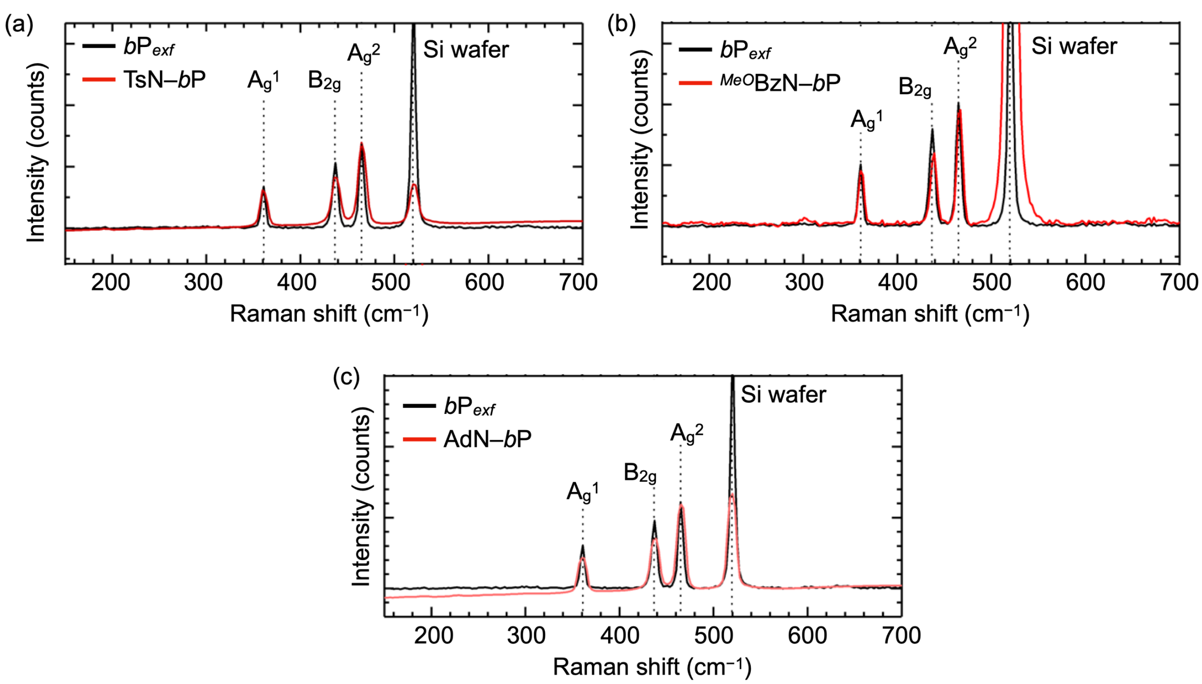

Figure A.7. Raman spectra of (a) TsN–bP, (b) ^{MeO}BzN–bP, and (c) AdN–bP with the spectrum for bP$_{exf}$ overlaid. Post-functionalization, slight broadening of the Raman signals as well as changes in the relative peak ratios of A_g^1, B_{2g}, and A_g^2 are observed; no changes in the Raman shifts of A_g^1, B_{2g}, or A_g^2 are observed. Excluding the features shown here, no detectable signals are observed in the full measurement range of 150–3000 cm^{-1}.

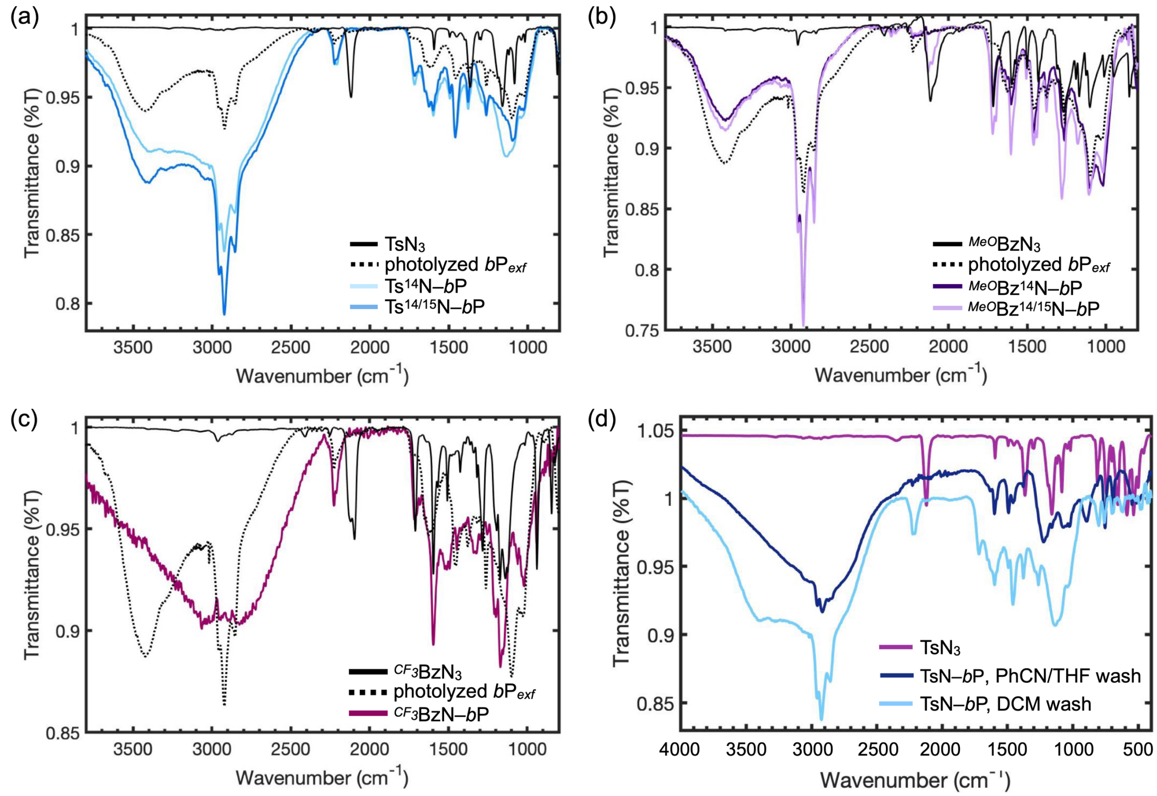

Figure A.8. Full IR spectra of (a) TsN–bP and Ts$^{14/15}$N–bP, (b) ^{MeO}BzN–bP and ^{MeO}Bz$^{14/15}$N–bP, and (c) ^{CF_3}BzN–bP overlaid with the respective azides and photolyzed bP$_{exf}$ control. (d) Full IR spectrum of TsN–bP comparing our standard PhCN and THF wash with a DCM wash after the functionalization reaction. Additional stretches between 900–500 cm^{-1} in TsN–bP washed with DCM suggest residual organic polymeric and oligomeric species on the bP surface.

Table A.1. Assigned IR vibrational modes of the TsN–bP features. Peaks were assigned using Parimala, *Spectrochim. Acta. A.* **2011**, *81*, 711; van Druenen, *Langmuir* **2019**, *35*, 2172, and the calculated IR spectrum in Figure A.10.

ν – stretching; γ – out-of-plane bending; β – in-plane bending; δ – scissoring

Signal	TsN–bP (cm^{-1}) (DRIFTS)	TsN_3 (cm^{-1}) (ATR)	photolyzed bP_{exf} (cm^{-1}) (ATR)
(PO_x)	1653, 1626	--	1653, 1631
(a) ν(C=C) + ν(SO_2)	1599	1595	1601w
(b) ν(C=C) + ν(SO_2)	1492	1495	--
(c) (PO_x)	1458	1451w	~1456
(d) (PO_x)	1378	--	1377
(e) ν(C=C)	~1370	1366	--
(f) (PO_x)	1262	--	1263
(g) ν(SO_2)$_{sym}$	~1155	1160	--
(h) $P{=}^{14}N$ ($P{=}^{15}N$)	~1120 (1094)	--	--
(PO_x)	~1104	--	1099
(i) β(CH) + ν(C=C) + γ(CH_3)	~1083	1084	--
(PO_x)	~1040, 1026	1040, 1018	1046, 1029

Table A.2. Assigned IR vibrational modes of the ^{MeO}BzN–*b*P features. Peaks were assigned using van Druenen, *Langmuir* **2019**, *35*, 2172; Maiti, *Phys. Chem. Chem. Phys.* **2015**, *17*, 19735, and the calculated IR spectrum in Figure A.10.

ν – stretching; γ – out-of-plane bending; β – in-plane bending; δ – scissoring

Signal	^{MeO}BzN–bP (cm^{-1}) (DRIFTS)	$^{MeO}BzN_3$ (cm^{-1}) (ATR)	photolyzed bP_{exf} (cm^{-1}) (ATR)
(a) ν(C=O)	1724	1717	--
$(PO)_x$	1654, 1630	--	1653, 1631
(b) aromatic ν(C=C)	1603	1599	--
(c) aromatic ν(C=C)	1507	1501	--
(d) $P{=}^{14}N$ ($P{=}^{15}N$)	1458 (1440)	--	~1456
(e) ν(C=C), Ph	1436	1430	--
(f) (PO_x)	1379	--	1377
(g) ν(COC)	1279	1273	--
(h) (PO_x)	1265	--	1263
(i) δ(CH), Ph	1173	1173	--
(j) ν(COC) / δ(CH), Ph / (PO_x)	1102	1107	1099
(k) δ(CH), Ph	1018	1013	--

Table A.3. Assigned IR vibrational modes of the ^{CF_3}BzN–*b*P features. Peaks were assigned using van Druenen, *Langmuir* **2019**, *35*, 2172; Maiti, *Phys. Chem. Chem. Phys.* **2015**, *17*, 19735; Miller, *Spectrochim. Acta Part A* **1969**, *25*, 1577; Berney, *Spectrochim. Acta* **1965**, *21*, 1809, and the calculated IR spectrum in Figure A.10.

ν – stretching; γ – out-of-plane bending; β – in-plane bending; δ – scissoring

Signal	^{CF_3}BzN–*b*P (cm^{-1}) (DRIFTS)	$^{CF_3}BzN_3$ (cm^{-1}) (ATR)	photolyzed *b*P_{exf} (cm^{-1}) (ATR)
(a) ν(C=O)	1715	1711	--
(b) aromatic ν(C=C)	1597	1597	--
(c) aromatic ν(C=C)	1509	1507	--
(d) (PO_x)	1446	--	~1456
(e) aromatic ν(C=C)	--	1426	--
hypothesized P=N	1332	--	--
(f) β(CH), Ph	1285	1283	--
(PO_x)	1254	--	1263
(g) β(CH), Ph	1199	1195	--
(h) δ(CH), Ph	1171	1173	--
(i) ν(C–F), CF_3	1146	1140	--
(PO_x)	1018	--	1026
(j) γ(CH)	940	938	--

A.2 ADDITIONAL DISCUSSION OF AMBIENT STABILITY

To assess degradation over time by UV-vis spectroscopy, two ambient stability tests were performed. For comparison with previously reported *p*-benzoic acid azide-functionalized bP,[58] the functionalized RN–bP materials reported here, bP_{exf}, and the photolyzed bP_{exf} control were dispersed in 5 mL milli-Q water under ambient conditions using ultrasonication. All suspensions were stored in air and measured once every 3–4 days for a total of 6 timepoints spanning 17 days (Figure 6a, b). As P=N bonds are known to hydrolyze in water, we separately tracked the ambient degradation of the materials in our exfoliation solvent, PhCN. TsN–bP and bP_{exf} were dispersed in 20 mL of dry PhCN under air-free conditions using ultrasonication. Half of each dispersion was

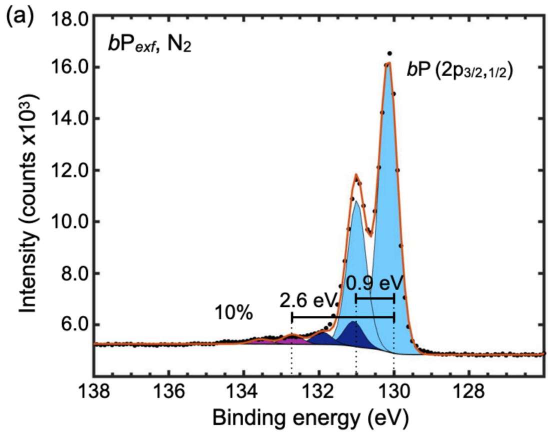

Figure A.9. High-resolution P2p XPS of (a) bP_{exf} and (b) TsN–bP after 7 days under air-free conditions. The environment at 130.0 eV (light blue) corresponds to unfunctionalized P(0) atoms. The higher-energy environments (navy blue, purple) correspond to P atoms in a higher oxidation state. For bP_{exf}, these higher energy environments are exclusively PO whereas our previous characterization of TsN–bP shows these environments correspond to both PN and PO. Importantly, these spectra cannot be directly compared to our other XPS measurements as they were obtained with a different spectrometer (Kratos Axis-Ultra DLD versus the SSI S-probe used for all other XPS measurements).

stored under air-free conditions to assess aggregation and precipitation of the nanosheets over time; the remainder was exposed to ambient conditions and monitored over 7 days (Figure 6c, d). All four samples were stirred for 10 minutes every day after measurement to introduce oxygen into the dispersions under ambient exposure. The supernatant was collected for the UV-vis measurements. All spectra were solvent-corrected and baseline-corrected to the absorbance at 1300 nm. Concentrations were calculated using the absorbance of each dispersion at 450 nm and the extinction coefficient calculated by Woomer and coworkers.[40] After 7 days, the materials dispersed in PhCN were isolated by vacuum filtration and washed with PhCN (1 x 30 mL) and THF (1 x 15 mL) under air-free conditions. For the bP_{exf} and TsN–bP dispersions exposed to ambient conditions, oxygen was first removed from the solvent using the freeze-pump-thaw method. All materials were then placed under vacuum before characterization by XPS. In order to approximate variations in percent composition derived from peak fitting, two spots on each sample were measured and fit 3 times independently to give a total of 6 peak fits per sample. This process gave an average oxidized P composition of 12±1% and 81±6% for bP$_{exf}$ in N_2 and air, respectively, and 17±2% and 81±1% for TsN–bP in N_2 and air, respectively.

A.3 CALCULATIONS

A.1.4. *Calculated IR spectra for molecular model systems RN=PPh$_3$ and RN(PPh$_2$)$_2$*

Molecular models of iminophosphoranes (Ph_3P=NR) and bisphosphinoamines ($(Ph_2P)_2NR$) were built for R = Ph, Ts, ^{MeO}Bz, and ^{CF3}Bz. DFT geometry optimizations and vibrational spectra

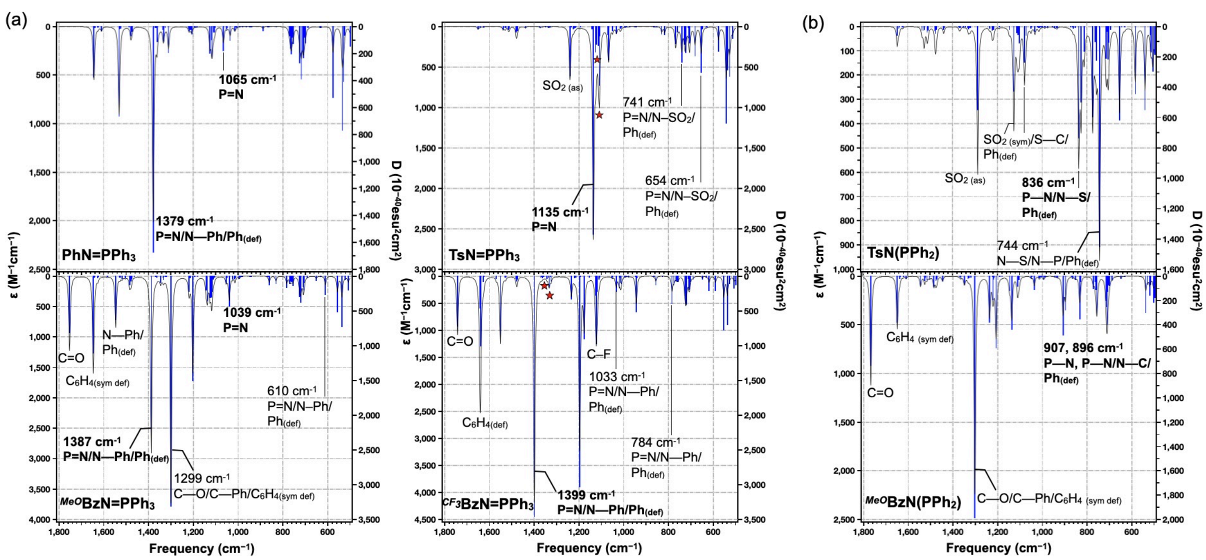

Figure A.10. Predicted vibrational spectra for (a) iminophosphoranes (RN=PPh$_3$, R=Ph, Ts, ^{MeO}Bz, ^{CF3}Bz) and (b) bisphosphinoamines ($(Ph_2P)_2$NR, R=Ts, ^{MeO}Bz). In addition to the primary P=N/P–N vibrations (bold text) observed in all spectra, many additional vibrational modes also contain a PN component. Red stars in the TsN=PPh$_3$ and ^{CF3}BzN=PPh$_3$ spectra denote clusters of peaks near the primary P=N mode that contain some PN component. In TsN=PPh$_3$, these stretches occur at 1126, 1121, 1114, and 1109 cm^{-1}; in ^{CF3}BzN=PPh$_3$, they occur at 1356, 1333, and 1327 cm^{-1}. The units on the y-axes of all graphs are defined as follows: ε is molar absorptivity; D is dipole strength.

calculations were obtained using the Gaussian package[59] with the input opt freq b3lyp/6-31+g(d) geom=connectivity.

A.1.5. *Energy and geometry optimization of tosyl nitrene binding modes on bP surface*

Geometry optimization and P–N vibrational energy prediction for tosyl-functionalized black phosphorus (Ts$^{14/15}$N–bP)

Calculations were performed with the NWChem computational chemistry program (version 6.8.1).[60] Geometry optimizations and vibrational mode calculations of all systems were performed using the 6-31G* basis set on all atoms[61,62] with B3LYP exchange-correlation functional[63,64] and the Grimme dispersion correction (D3).[65] The normal modes, vibrational frequencies, and IR intensities were also calculated, and IR spectra were generated using a line broadening of 10 cm^{-1}. Vibrational frequencies for the functionalized nanosheets were calculated for both ^{14}N and ^{15}N isotopologues.

Initial geometry optimizations were performed on a bare finite sheet consisting of 110 phosphorus atoms produced from experimental X-ray data corresponding to a single layer of *b*P.[66] Hydrogen atoms were used to cap the dangling bonds on the edges of the sheet. The H atoms were constrained to lie along the P–P bond vectors connecting the trimmed sheet to phosphorus atoms they replaced.

Table A.4. Table of calculated energies for each binding configuration, relative to the lowest-energy configuration, (1). Motifs (3a) and (3b) are nearly identical to (1) and were thus not considered in the generation of calculated vibrational spectra.

Bond Mode	ΔE (eV)
bP-Ts_01	0.100
bP-Ts_02	0.502
bP-Ts_03a	0.074
bP-Ts_03b	0

A geometry optimization routine was performed in which the central 48 phosphorus atoms were allowed to move while the outer edges of the sheet were held fixed to the experimental geometry of a pristine black phosphorus crystal. After the optimization, the free phosphorus atoms shifted very little (~0.08 Å average) from their initial positions. A single tosyl nitrene fragment was installed on the geometry optimized sheet with three distinct binding modes (Figure 2) where motif (1) is an iminophosphorane, $TsN{=}P_{bP}$, (2) is a bisphosphinoamine, $TsN(\lambda^3\text{-}P_{bP})_2$, and (3) is a cyclic μ-nitrene diphosphine, $TsN(\lambda^4\text{-}P_{bP})_2$.

Geometry optimization of the TsN–bP sheet showed convergence of motifs (1) and (3); thus, (3) does not represent a distinct binding motif computationally and was discarded from further analysis. Motif (1) was found to have a lower energy than the alternative binding configuration (2) by 0.40 eV. These findings are in good agreement with literature reports of a similar calculation performed with the analogous fragment of 4-azidobenzoic acid as the functional group (ΔE[binding configurations] = 0.45 eV).[58]

A.4 References

[1] F. Tao, Z. H. Wang, X. F. Chen, G. Q. Xu, *Phys. Rev. B* **2002**, *65*, 115311.

[2] Y. Liu, P. Gao, T. Zhang, X. Zhu, M. Zhang, M. Chen, P. Du, G. Wang, H. Ji, J. Yang, S. Yang, *Angew. Chem. Int. Ed.* **2019**, *58*, 1479–1483.

[3] A. H. Woomer, T. W. Farnsworth, J. Hu, R. A. Wells, C. L. Donley, S. C. Warren, *ACS Nano* **2015**, *9*, 8869–8884.

[4] M. J. Frisch, G. W. Trucks, H. B. Schlegel, G. E. Scuseria, M. A. Robb, J. R. Cheeseman, J. A. Montgomery, Jr, T. Vreven, K. N. Kudin, J. C. Brant, J. M. Millam, S. S. Iyengar, J. Tomasi, V. Barone, B. Mennucci, M. Cossi, G. Scalmani, N. Rega, G. A. Petersson, **2004**.

[5] M. Valiev, E. J. Bylaska, N. Govind, K. Kowalski, T. P. Straatsma, H. J. J. Van Dam, D. Wang, J. Nieplocha, E. Apra, T. L. Windus, W. A. de Jong, *Computer Physics Communications* **2010**, *181*, 1477–1489.

[6] G. A. Petersson, A. Bennett, T. G. Tensfeldt, M. A. Al-Laham, W. A. Shirley, J. Mantzaris, *The Journal of Chemical Physics* **1988**, *89*, 2193–2218.

[7] G. A. Petersson, M. A. Al-Laham, *The Journal of Chemical Physics* **1991**, *94*, 6081–6090.

[8] A. D. Becke, *The Journal of Chemical Physics* **1993**, *98*, 5648–5652.

[9] P. J. Stephens, F. J. Devlin, C. F. Chabalowski, M. J. Frisch, *J. Phys. Chem.* **1994**, *98*, 11623–11627.

[10] S. Grimme, J. Antony, S. Ehrlich, H. Krieg, *The Journal of Chemical Physics* **2010**, *132*, 154104.

[11] R. Hultgren, N. S. Gingrich, B. E. Warren, *The Journal of Chemical Physics* **1935**, *3*, 351–355.

APPENDIX B: SUPPLEMENTAL INFORMATION FOR CHAPTER 3

B.1 ADDITIONAL CHARACTERIZATION OF METALLATED NANOSHEETS

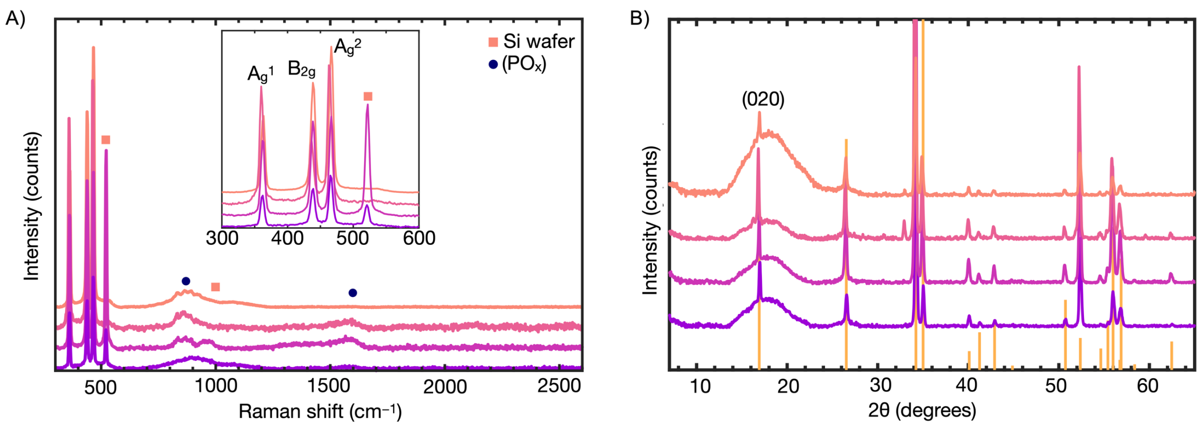

Figure B.1. (A) Raman spectra of (bottom to top) **1**(bP)(Cl), [**3**(bP)][Cl], **2**(bP), and **4**(bP). Inset shows zoom-in on key bP Raman modes. (B) XRD patterns for (bottom to top) bP reference, **1**(bP)(Cl), [**3**(bP)][Cl], **2**(bP), and **4**(bP).

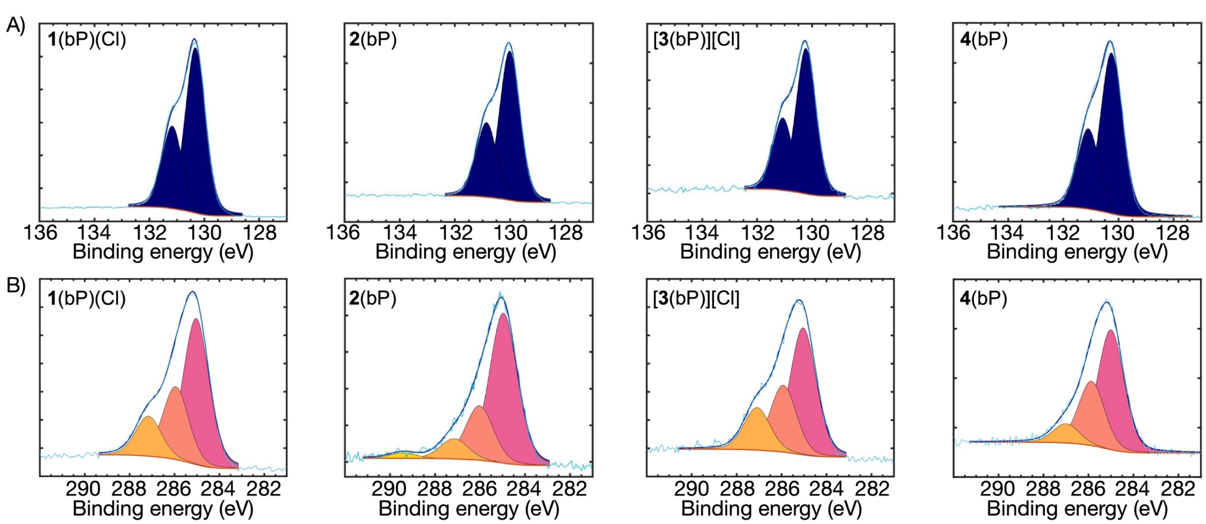

Figure B.2. High-resolution (A) P 2p and (B) C 1s XPS of **1**(bP)(Cl), **2**(bP), [**3**(bP)][Cl], and **4**(bP).

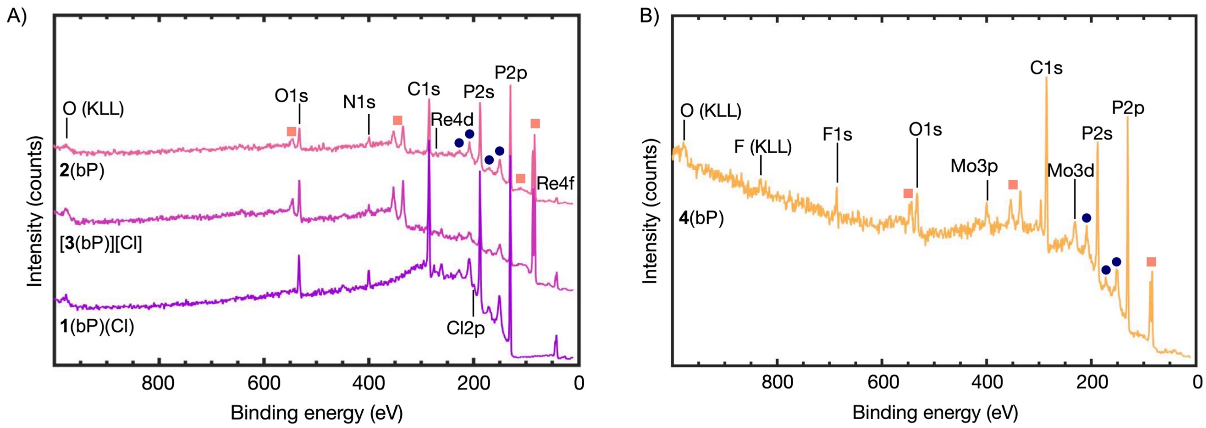

Figure B.3. XPS survey spectra of (A) **1**(bP)(Cl), [**3**(bP)][Cl], and **2**(bP), and (B) **4**(bP). Peach squares and navy circles indicate features from the Au wafer and bP plasmon modes, respectively.

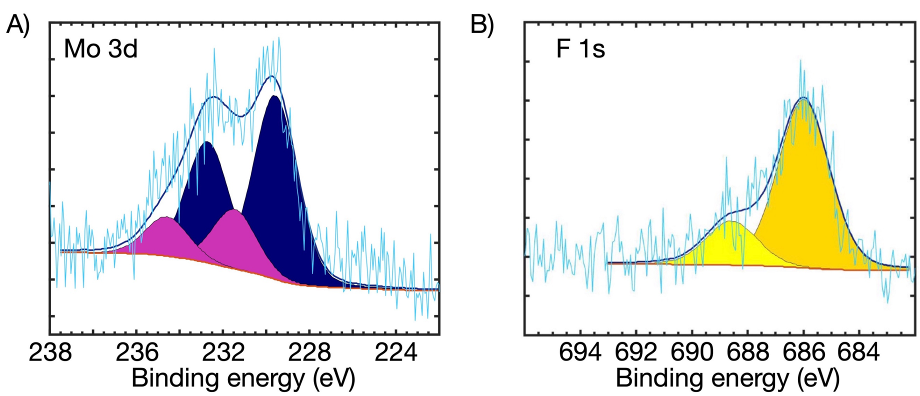

Figure B.4. High-resolution (A) Mo 3d and (B) F 1s XPS spectra of **4**(bP). The high and low energy environments are present in a 25:75 and 21:79 ratio for (A) and (B), respectively.

Table B.1. Literature Re $4f_{7/2}$ binding energies for select materials and complexes. Binding energies were adjusted to the same reference as used for experimental values (C1s at 285.0 eV).

Complex/Material	Reported Re $4f_{7/2}$ binding energy (eV)	Reference
Re(^{t}Bu-bipy)$(CO)_3$Cl on MWCNTs	42.4	Kubiak, *JACS* **2019**
Re(N–N)$(CO)_3$Cl tethered to carbon support	41.7	Piers, *ACS Appl. Energy Mater.* **2019**, *2*, 2414
Re(phen)$(CO)_3$Cl on graphitic carbon	42.0	Surendranath, Y. *JACS* **2016**, *138*, 1820.
Re oxides	43.0–46.8	NIST database
Re metal	40.3	NIST database
Re$(PPh_3)(CO)_3$Cl	41.6	NIST database

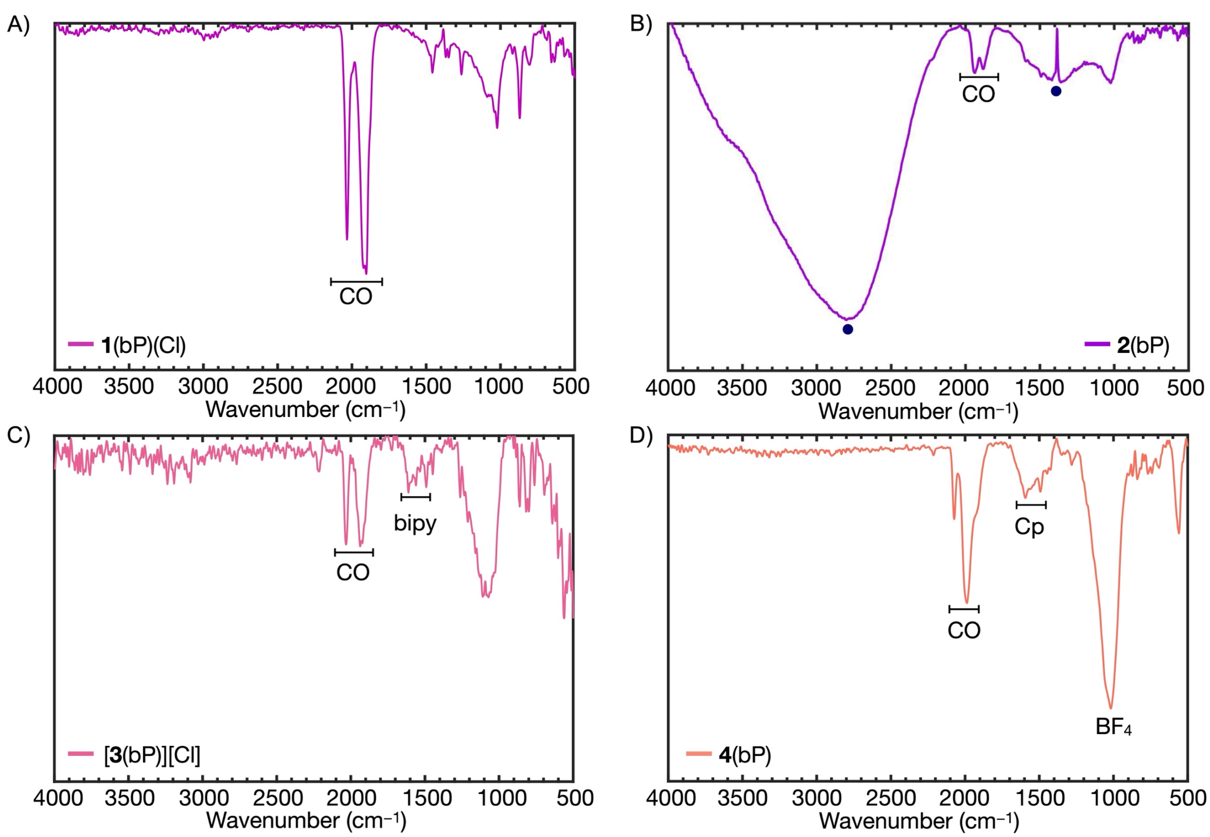

Figure B.5. Full DRIFTS spectra for (A) **1**(bP)(Cl), (B) **2**(bP), (C) [**3**(bP)][Cl], and (D) **4**(bP).

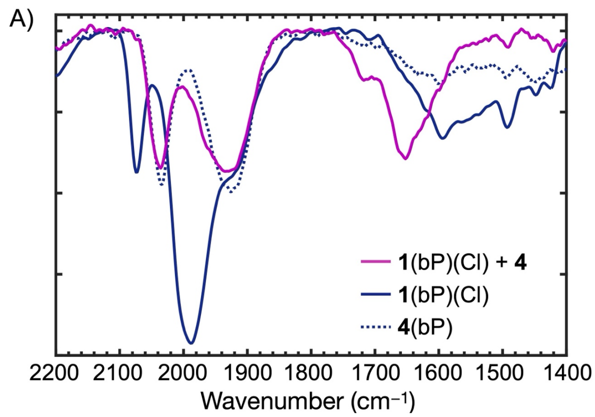

Figure B.6. Full DRIFTS spectra for (A) **1**(bP)(Cl) + **4** and (B) **2**(bP) + **4** overlaid with relevant comparisons.

Table B.2. Literature ν(CO) values for select **2**(PR_3) complexes. Intensities are denoted as follows: vs = very strong; s = strong; m = medium.

R =	Reported A' ν(CO) (cm^{-1})	Measurement method	Reference
OPh	1961s, 1891s	DCM	Lokshin, *J. Organomet. Chem.* **1976**, *108*, 353.
Ph	1943m, 1881m	Cyclohexane	Angelici, *Synth. React. Inorg. Met-Org.* **1990**, *20*, 275.
Me	1937vs, 1872vs	Hexane	Angelici, *Synth. React. Inorg. Met-Org.* **1990**, *20*, 275.

Table B.3. Literature ν(CO) values for select products of reactions of $CpMo(CO)_3X$ and PR_3. Intensities are denoted as follows: vs = very strong; s = strong; m = medium.

R =	Reported ν(CO) (cm^{-1})	Measurement method	Reference
$[CpMo(CO)_3(PPh_3)]BF_4$	2062, 2001, 1975*	DCM	Sünkel, Z. *Naturforsch. Pt. B* **1981**, *36*, 474.
$[CpMo(CO)_2(PPh_3)_2]BF_4$	1978s, 1901vs	DCM	Sünkel, Z. *Naturforsch. Pt. B* **1981**, *36*, 474.
$[CpMo(CO)_2(dmpe)]PF_6$	1983s, 1913s	DCM	Kegley, *Organomet.* **1993**, *12*, 2339.

Table B.4. Literature ν(CO) values for select products of $Re(bipy)(CO)_3X$ and PR_3. Intensities are denoted as follows: vs = very strong; s = strong; m = medium.

Complex	Reported ν(CO) (cm^{-1})	Measurement method	Reference
fac-$[Re(bipy)(CO)_3(PPh_3)]PF_6$	2041, 1954, 1924*	MeCN	Ishitani, *Dalton Trans.* **2005**, *2*, 385.
cis-$[Re(bipy)(CO)_2(dppm)]OTf$	1950, 1884*	DCM	Schutte, *Inorg. Chem.* **1998**, *37*, 2618.
cis-$[Re(bipy)(CO)_2(PPh_3)_2]OTf$	1938, 1868*	DCM	Smithback, *Inorg. Chem.* **2006**, *45*, 2163.
cis-$Re(bipy)(CO)_2(P(OEt)_3)Cl$	1936, 1857*	KBr	Ishitani, *Inorg. Chem.* **2000**, *39*, 2777.

B.2 METHODS TO ESTIMATE THE ELECTRONIC AND STERIC CHARACTER OF BP

The method for estimating the Tolman electronic parameter (TEP) of bP was based on the work of Anton and Crabtree with $Mo(CO)_4(L–L)$.[13] The authors show that $Mo(CO)_4(L–L)$ can be used as an experimental probe for phosphine electronic character akin to Tolman's work with $Ni(CO)_3L$.[14] By plotting experimentally determined symmetric νCO_{Mo} for a variety of monodentate PR_3 against A_1 νCO_{Ni} reported by Tolman, Anton and Crabtree demonstrated correlation between the two scales and developed an equation to relate their experimental values to Tolman's. Through this correlation, they were able to determine the TEP of chelating phosphines, which are excluded from Tolman's original scale. This method has been repeated for multiple metal carbonyl complexes,[15] ultimately demonstrating that any metal carbonyl complex can be used as a reliable probe if it shows correlation with Tolman's scale.[15]

Previously reported symmetric νCO_{Re} for $[Re(bipy)(CO)_3(PR_3)][X]$ (referred to as [**3**(PR_3)][X]) with a variety of PR_3 ligands showed good linear correlation with Tolman's scale through this

Table B.5. Calculated % buried volumes for select molecular complexes.

Complex	L =	Binding mode type	Calculated %V_{bur}
$Re(CO)_3(Cl)(L)$	dmpe	κ^2	37
	Modified dppp	κ^2	44
	dppp	κ^2	44
$Re(CO)_3(Cl)(L_2)$	benzyl	κ^2	44
	phenyl	κ^2	48
	Ph–OMe	κ^2	49
[Re(bipy)$(CO)_3$(L)][X]	MeOH	κ^1	21
	^{n}Bu	κ^1	22
	Et	κ^1	23
	p-toluene	κ^1	25
	phenyl	κ^1	25
	Ph–OMe	κ^1	25

method.[1] Comparison of the reported symmetric ν(CO) for [**3**(PPh_3)][X] with our experimental value gave a difference of only 8 cm^{-1}, an acceptable value for this qualitative comparison.

The percent buried volume (%V_{bur}) was calculated using the SambVca 2.1 online calculator tool[1] using [**3**(PR_3)][X] and **1**(bP)(Cl) for the κ^1 and κ^2 binding modes, respectively. bP structures were optimized and molecular structures were obtained from the CCDC database. In order to provide accurate comparison between ligands, the Re–P bond length was set to the average bond length reported for each geometry (2.478 Å for κ^1 binding mode and 2.469 Å for κ^2 binding mode).[1] For the κ^1 geometry, the xz axis was defined between the two equatorial CO groups; for κ^2, it was defined between the axial CO and the halide.

B.3 FURTHER DISCUSSION ON DEGREE OF FUNCTIONALIZATION

One hypothesis for the trend in degree of functionalization observed by XPS is the electrophilicity of the molecular species. Assuming a dissociative mechanism is at play during the substitution, as reported for the molecular phosphines, the leaving group, either CO, Cl^-, or BF_4^-, will dissociate leaving a coordinatively unsaturated 16 e^- metal fragment that can react with bP. The most electrophilic species, $CpMo(CO)_3^+$, shows the highest degree of functionalization followed by $Re(bipy)(CO)_3^+$, $Re(CO)_2(Cl)$, and $CpRe(CO)_2$. Other factors likely influence the degree of functionalization, including the steric profile of the fragment and the type of binding with the nanosheet surface (i.e. κ^1 or κ^2) as well as the differing reaction conditions for each functionalization method. While these values obtained by XPS only represent 2 measurements, they suggest an interesting avenue for further study.

B.4 ADDITIONAL CHARACTERIZATION OF ANION EXCHANGE PRODUCTS

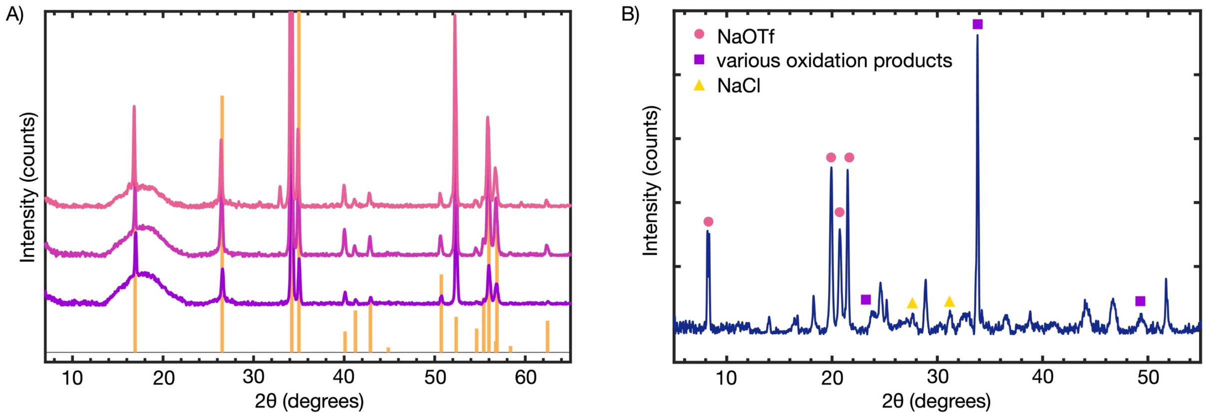

Figure B.7. XRD of (A) anion exchange products (bottom to top) bP reference, **1**(bP)(OTf), **1**(bP)(NCS), and **1**(bP)(NCO), and (B) filtrate from the synthesis of **1**(bP)(OTf).

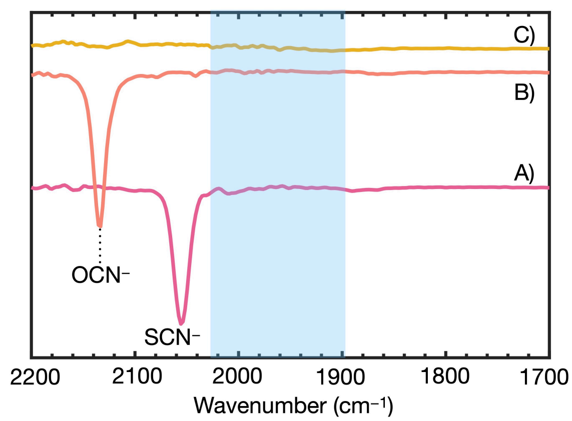

Figure B.8. ATR-IR of filtrates (THF) from synthesis of (A) **1**(bP)(NCS), (B) **1**(bP)(NCO), and (C) **1**(bP)(OTf). The blue box highlights the CO region.

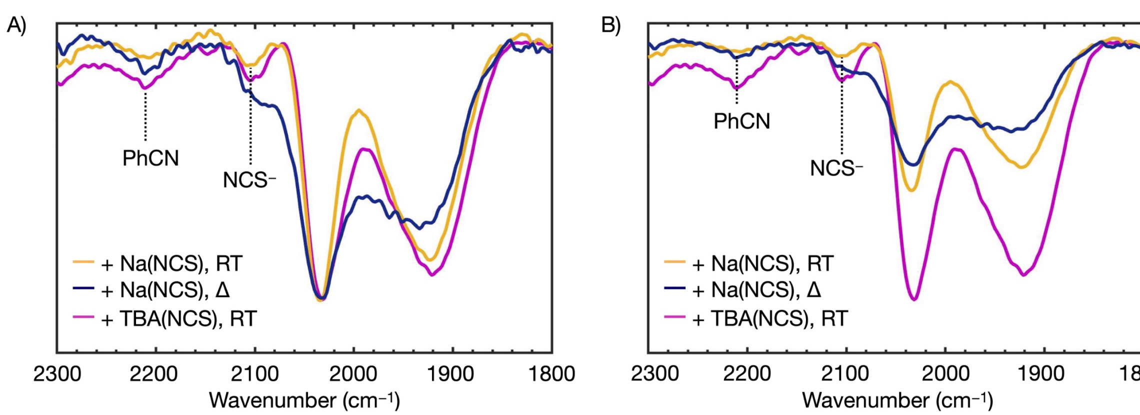

Figure B.9. DRIFTS of **1**(bP)(NCS) obtained by three different methods. The spectra are (A) normalized to the symmetric CO stretch and (B) unnormalized.

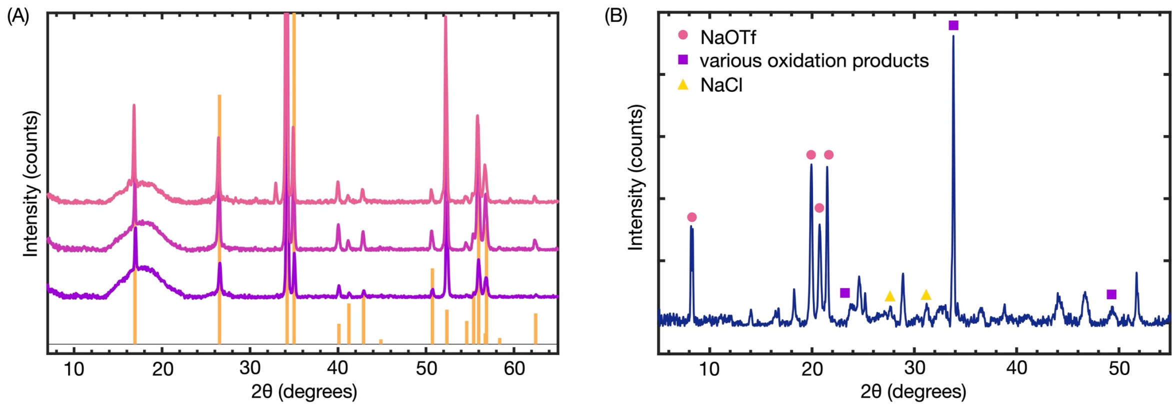

Figure B.10. DRIFTS of (A) OTf⁻ and (B) SCN⁻ control reactions overlaid with the respective parent salts and **1**(bP)(X) spectra.

Table B.6. Literature ν(X) and ν(CO) values for **1**(PR_3)(X).

X =	R =	Reported ν(X) (cm^{-1})	Reported ν(CO) (cm^{-1})	Measurement method	Reference
OTf	dppe	1317	2035, 1958, 1917	KBr	Dahlenburg, *J. Organomet. Chem.* **1996**, *525*, 115.
OTf	PPh_3	1341	2039, 1954, 1910	KBr	Dahlenburg, *J. Organomet. Chem.* **1996**, *525*, 115.
NCS	PPh_3	2093	2054, 1958, 1919	DCE	Hoffman, *Inorg. Chem.* **1991**, *30*, 4177.
NCO	PPh_3	2230	2028, 1925, 1843	KBr	Moelwyn-Hughes, *J. Chem. Soc. A.* **1971**, 2361.

B.5 ADDITIONAL CHARACTERIZATION OF SEQUENTIAL ANION EXCHANGE AND INSERTION PRODUCTS

Table B.7. Literature ν(X) and ν(CO) values for **1**(PR_3)(X).

X =	R =	Reported ν(X) (cm^{-1})	Reported ν(CO) (cm^{-1})	Measurement method	Reference
OTf	dppe	1317	2035, 1958, 1917	KBr	Dahlenburg, *J. Organomet. Chem.* **1996**, *525*, 115.
OMe	Me	Not reported	2012, 1921, 1875	KBr	Simpson, *Organomet.* **1993**, *12*, 781.
CO_3Me	Me	1670	2027, 1978, 1905	KBr	Simpson, *Organomet.* **1992**, *11*, 4306.

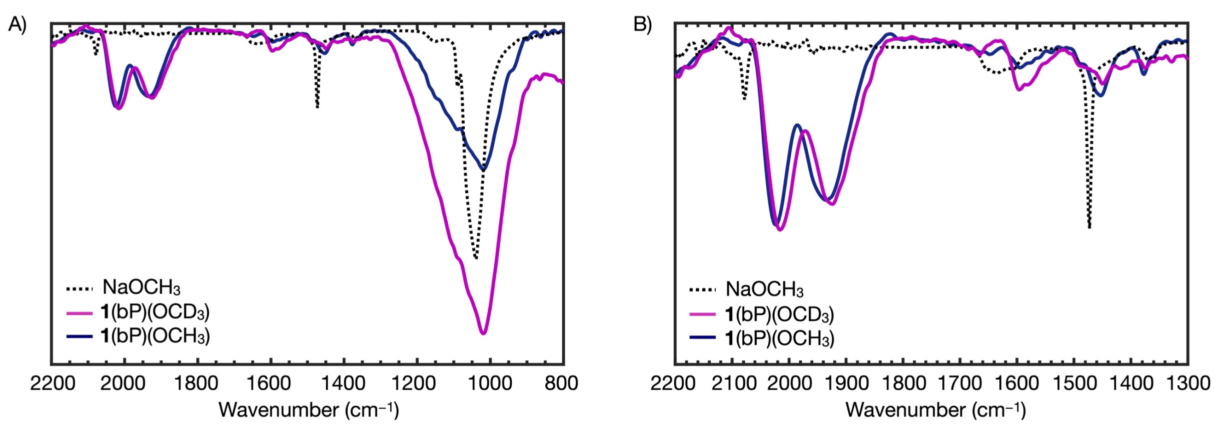

Figure B.11. (A) Full IR spectrum and (B) zoom-in of **1**(bP)(OCH_3) and **1**(bP)(OCD_3) overlaid with $NaOCH_3$.

B.6 REFERENCES

[1] D. R. Anton, R. H. Crabtree, *Organometallics* **1983**, *2*, 621–627.

[2] C. A. Tolman, *Chem. Rev.* **1977**, *77*, 313–348.

[3] O. Kuhl, *Coordination Chemistry Reviews* **2005**, *249*, 693–704.

[4] L. Falivene, Z. Cao, A. Petta, L. Serra, A. Poater, R. Oliva, V. Scarano, L. Cavallo, *Nat. Chem.* **2019**, *11*, 872–879.

[5] A. Poater, B. Cosenza, A. Correa, S. Giudice, F. Ragone, V. Scarano, L. Cavallo, *Eur. J. Inorg. Chem.* **2009**, *2009*, 1759–1766

VITA

Kendahl grew up in Clyde, Ohio and completed her undergraduate degree at Rice University where she graduated in 2017 with a degree in Chemistry. Her undergraduate research was conducted with Prof. Angel Martí on the covalent functionalization of boron nitride nanomaterials. During graduate school, Kendahl participated as a diligence analyst with the E8 Angel Investors through the Torrance Technology Due Diligence Fellowship. Outside of the lab, Kendahl enjoys hand embroidery, hiking, and kayaking.